UNIVERSITAT DE BARCELONA

Computational modelling of magnetic and conductive properties of multifunctional molecular materials

Cristina Roncero Barrero

ADVERTIMENT. La consulta d'aquesta tesi queda condicionada a l'acceptació de les següents condicions d'ús: La difusió d'aquesta tesi per mitjà del servei TDX (**www.tdx.cat**) i a través del Dipòsit Digital de la UB (**diposit.ub.edu**) ha estat autoritzada pels titulars dels drets de propietat intel·lectual únicament per a usos privats emmarcats en activitats d'investigació i docència. No s'autoritza la seva reproducció amb finalitats de lucre ni la seva difusió i posada a disposició des d'un lloc aliè al servei TDX ni al Dipòsit Digital de la UB. No s'autoritza la presentació del seu contingut en una finestra o marc aliè a TDX o al Dipòsit Digital de la UB (framing). Aquesta reserva de drets afecta tant al resum de presentació de la tesi com als seus continguts. En la utilització o cita de parts de la tesi és obligat indicar el nom de la persona autora.

ADVERTENCIA. La consulta de esta tesis queda condicionada a la aceptación de las siguientes condiciones de uso: La difusión de esta tesis por medio del servicio TDR (**www.tdx.cat**) y a través del Repositorio Digital de la UB (**diposit.ub.edu**) ha sido autorizada por los titulares de los derechos de propiedad intelectual únicamente para usos privados enmarcados en actividades de investigación y docencia. No se autoriza su reproducción con finalidades de lucro ni su difusión y puesta a disposición desde un sitio ajeno al servicio TDR o al Repositorio Digital de la UB. No se autoriza la presentación de su contenido en una ventana o marco ajeno a TDR o al Repositorio Digital de la UB (framing). Esta reserva de derechos afecta tanto al resumen de presentación de la tesis como a sus contenidos. En la utilización o cita de partes de la tesis es obligado indicar el nombre de la persona autora.

WARNING. On having consulted this thesis you're accepting the following use conditions: Spreading this thesis by the TDX (**www.tdx.cat**) service and by the UB Digital Repository (**diposit.ub.edu**) has been authorized by the titular of the intellectual property rights only for private uses placed in investigation and teaching activities. Reproduction with lucrative aims is not authorized nor its spreading and availability from a site foreign to the TDX service or to the UB Digital Repository. Introducing its content in a window or frame foreign to the TDX service or to the UB Digital Repository is not authorized (framing). Those rights affect to the presentation summary of the thesis as well as to its contents. In the using or citation of parts of the thesis it's obliged to indicate the name of the author.

Computational modelling of magnetic and conducting properties of multifunctional molecular materials

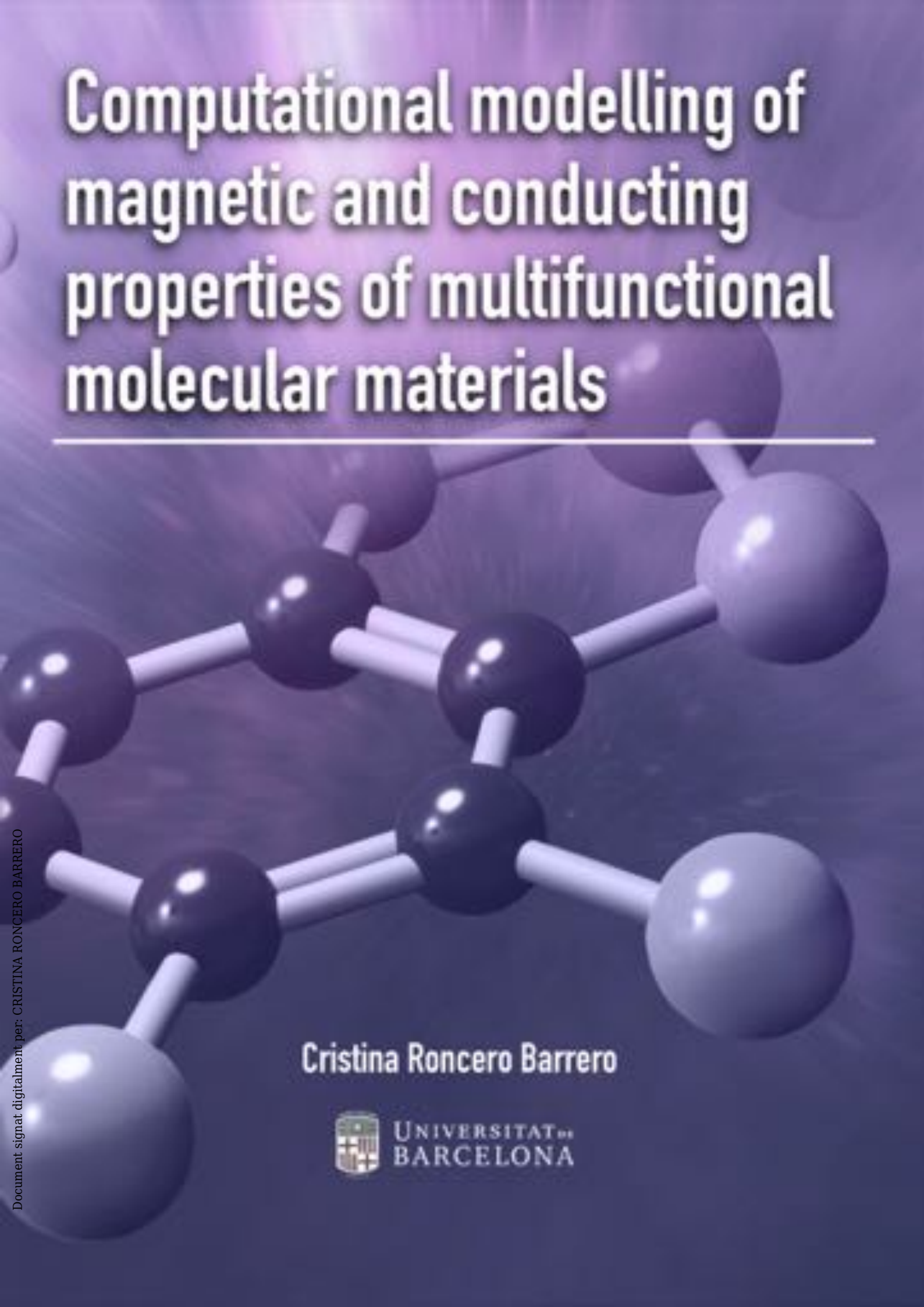

Cristina Roncero Barrero

UNIVERSITAT DE BARCELONA

Document signat digitalment per: CRISTINA RONCERO BARRERO

Document signat digitalment per: CRISTINA RONCERO BARRERO

=

This dissertation is submitted for the degree of
Doctor of Philosophy in

Theoretical Chemistry and Computational Modelling

Computational modelling of magnetic and conductive properties of multifunctional molecular materials

Author: Cristina Roncero Barrero
Theoretical and Computational Chemistry Institute
Department of Materials Science & Physical Chemistry
Facultat de Química,
Universitat de Barcelona

Supervisors:

Dr. Mercè Deumal i Solé
Theoretical and Computational Chemistry Institute
Department of Materials Science & Physical Chemistry
Facultat de Química,
Universitat de Barcelona

Dr. Ibério de P. Ribeiro Moreira
Theoretical and Computational Chemistry Institute
Department of Materials Science & Physical Chemistry
Facultat de Química,
Universitat de Barcelona

Tutor: Prof. Francesc Illas Riera
Theoretical and Computational Chemistry Institute
Department of Materials Science & Physical Chemistry
Facultat de Química,
Universitat de Barcelona

Document signat digitalment per: CRISTINA RONCERO BARRERO

Document signat digitalment per: CRISTINA RONCERO BARRERO

"*The most important step a man can take. It's not the first one, is it?*
It's the next one. Always the next step, Dalinar."

Brandon Sanderson, Oathbringer

Document signat digitalment per: CRISTINA RONCERO BARRERO

Document signat digitalment per: CRISTINA RONCERO BARRERO

Document signat digitalment per: CRISTINA RONCERO BARRERO

Document signat digitalment per: CRISTINA RONCERO BARRERO

Abstract

Purely organic radical-based materials constitute a promising approach for the miniaturization of devices due to their interesting optical, electronic and magnetic properties, and are good candidates to substitute scarce and/or environmentally harmful transition metal and lanthanide compounds. However, the inclusion of any type of paramagnetic molecular entity faces critical issues related to the stability of the materials and temperature range applicability. Nevertheless, advances in the last 30 years in producing stable persistent paramagnetic organic molecules provided stable enough organic radicals and polyradicals that can be used to produce molecular materials with a wide range of properties. The use of organic radicals in the development of organic (semi)conductors gives rise naturally to multifunctional materials because the spin moment associated with the unpaired electron of the radicals endows the (semi)conductor with magnetic properties. The multifunctional character of this type of material can become even more relevant when charge transport and magnetism are not considered separately. Indeed, the magnetoresistance featured by some organic conducting magnets holds great promise for the development of spintronic devices.

In organic-radical based semiconductor materials, both charge and spin of the unpaired electron of the spin-carrying units play a key role. Indeed, the unpaired electrons of radicals are not only charge carriers but also the source of magnetic moments. The correct modelling of the electronic structure and the properties of these systems is thus a challenge due to the competition between charge localization or charge transport. Typically, organic molecular materials present low charge mobility, and hence, hopping model usually dominates the charge transport process. Computational studies based on hopping charge transfer models have been successfully applied in the analysis of closed-shell organic materials. However, in the literature, there are few studies that deal with the

Document signat digitalment per: CRISTINA RONCERO BARRERO

applicability of these hopping models to open-shell systems, and as far as we know, none of them tackles the calculation of electric conductivity.

Bisdithiazolyl (bisDTA) radicals have furnished in recent years multiple examples of molecular materials with promising conductive and magnetic properties. This large and well-characterized family of compounds have been constructed in the quest to find a radical-based single component conductor, following different synthetic strategies that aim to enhance their electric properties whereas preventing dimerization. As a result, the bisDTA family of compounds display a wide range of conductive properties (going from insulator to metallic materials), as well as a wide range of magnetic properties (going from materials with no long-range magnetic order to materials that order antiferromagnetically or ferromagnetically). Our computational work focuses on the study of four isostructural pyridine-bridged bisDTA-multifunctional materials triggered by their magnetic and conducting properties being strongly dependent on the different S/Se ratio in the neutral radical skeleton.

The electronic structure of the four bisDTA-derived materials has been characterized by means of periodic unrestricted hybrid DFT calculations. The analyses of their band structure and density of states have served as a crucial starting point for the rationalization of their electric properties and the relevant intermolecular contacts involved in the description of the charge transport process. Furthermore, the study of their open-shell ground state and the spin delocalization has proved that the molecular building blocks act as localized spin-carrying units, allowing the rationalisation of their magnetic interactions using a HDVV Hamiltonian.

A systematic bottom-up strategy has been used in order to thoroughly compute all the relevant microscopic parameters that govern both magnetism (magnetic exchange couplings) and charge transport (electronic coupling and reorganization energy). Microscopic interactions have been put to test by computing the macroscopic properties (magnetic susceptibility, critical

Document signat digitalment per: CRISTINA RONCERO BARRERO

temperature and electric conductivity) and comparing them with the available experimental data.

Furthermore, structural-property correlations analysis (ie. magneto structural correlation maps and distance analysis) has proved that properties in these materials are sensitive to small geometry distortions.

Document signat digitalment per: CRISTINA RONCERO BARRERO

Document signat digitalment per: CRISTINA RONCERO BARRERO

Resum

Els materials basats en radicals orgànics constitueixen una prometedora proposta per a la miniaturització de dispositius tecnològics gràcies a les seves propietats òptiques, elèctriques i magnètiques, i són bons candidats per a substituir els escassos i/o mediambientalment nocius metalls de transició i compostos derivats dels lantànids. L'ús de radicals orgànics en el desenvolupament de (semi)conductors dona lloc de forma natural a materials multifuncionals, degut a que el moment d'espín associat a l'electró desaparellat dota addicionalment al (semi)conductor amb propietats magnètiques.

En aquesta tesi, ens centrarem en l'estudi de materials moleculars constituïts per radicals orgànics, en els quals, l'electró desaparellat del radical servirà a la vegada com a portador de càrrega i com a font de moment magnètic. La correcta modelització de l'estructura electrònica i les propietats en aquests sistemes és un repte pels mètodes actuals, degut a la competició entre localització de càrrega i el seu transport. Típicament, els estudis computacionals dedicats a la conductivitat elèctrica en materials moleculars orgànics fan servir el que s'anomena model de *hopping*, degut als baixos valors de conductivitat que presenten generalment aquests materials. Malgrat els avenços reportats amb aquests models en l'estudi de sistemes de capa tancada, hi ha pocs estudis dedicats a l'anàlisi de materials de capa oberta i cap en què es calculi la conductivitat elèctrica a partir de models de *hopping*.

S'han seleccionat quatre materials isoestructurals d'una gran família de derivats del bisditiazolil, degut a l'ampli espectre de propietats magnètiques i elèctriques que presenten, per tal de testejar una estratègia *bottom-up* sistemàtica per a l'estudi dels paràmetres microscòpics rellevants en la descripció del magnetisme i la conductivitat elèctrica en materials moleculars de capa oberta.

Document signat digitalment per: CRISTINA RONCERO BARRERO

Els resultats obtinguts corroboren que l'anàlisi, mitjançant càlculs periòdics de l'estructura electrònica, la densitat d'estats i l'estructura de bandes, estableix un punt de partida clau per a la descripció de les propietats en aquests sistemes.

Mitjançant un estudi sistemàtic *bottom-up* s'han pogut caracteritzar tots els paràmetres microscòpics rellevants que governen tant el magnetisme com la conductivitat en aquests sistemes. Els resultats s'han pogut corroborar comparant-los amb les dades experimentals reportades.

Finalment, mitjançant una anàlisi completa de les distàncies i mapes de correlació estructura-propietat s'ha evidenciat que les propietats en aquests sistemes són sensibles als subtils canvis que pot patir l'estructura cristal·lina.

Document signat digitalment per: CRISTINA RONCERO BARRERO

Abbreviations

- **bisDTA** Bisdithiazolyl
- **FPBU** First-Principles Bottom-Up
- J_{AB} Exchange coupling
- **T** Temperature
- **SOMO** Singly Occupied Molecular Orbital
- **HDVV** Heisenberg-Dirac-VanVleck
- **FM** Ferromagnetic
- **AFM** Antiferromagnetic
- **CASSCF** Complete Active Space Self-Consistent field
- **CASPT2** Complete Active Space 2nd order Perturbation Theory
- **DFT** Density Functional Theory
- **BS** Broken Symmetry
- χ Magnetic susceptibility
- T_c Critical temperature
- C_p Heat capacity
- C_s Magnetic capacity
- **VB** Valence Bond
- P_{ij} Spin-exchange density matrix elements
- σ Electric conductivity
- ρ_c Density of charge carriers
- μ Mobility
- q Charge
- E Electric field
- v Drift velocity
- **D** Donor
- **A** Acceptor
- **CT** Charge Transfer

Document signat digitalment per: CRISTINA RONCERO BARRERO

- **PES** Potential Energy Surface
- $\boldsymbol{k_{DA}}$ Rate constants
- $\boldsymbol{H_{DA}}$ Electronic coupling
- $\boldsymbol{\lambda}$ Reorganization energy
- $\boldsymbol{\Delta G^{\ddagger}}$ Diabatic activation energy
- $\boldsymbol{\Delta G^{0}}$ Driving force
- **TS** Transition State
- **CS** Closed-shell
- **DOS** Density of states
- $\boldsymbol{\varepsilon_F}$ Fermi energy
- E_g Band gap
- **RHF** Restricted Hartree-Fock
- **MO** Molecular orbital
- **HOMO** Highest occupied molecular orbital

Document signat digitalment per: CRISTINA RONCERO BARRERO

Table of contents

Document signat digitalment per: CRISTINA RONCERO BARRERO

PART 2. RESULTS

PART 3. ANNEXES

Document signat digitalment per: CRISTINA RONCERO BARRERO

PART I. INTRODUCTION

Document signat digitalment per: CRISTINA RONCERO BARRERO

Document signat digitalment per: CRISTINA RONCERO BARRERO

Chapter 1. Thesis Overview

Organic radical-based materials are open-shell systems with one (or more) unpaired electron per constitutive unit, which potentially grants them magnetic and/or electric properties.[1-6] The open-shell nature of their building blocks makes them highly reactive and thus, kinetically and thermodynamically unstable, which limits their applications. Radical-based materials are easily oxidized or reduced, depending on the relative stability of the closed-shell cation or anion species. If the open-shell configuration prevails, *ie.* σ and π-dimerization is prevented, these redox reactions might lead to different applications: i) they can be involved in reversible redox processes, which will yield energy storage applications[7,8,9] and ii) as components in organic electronics[10,11,12], when there is a network of interconnected electron exchange sites. Additionally, taking advantage of the spin state of the unpaired electron, they can present magnetic interactions[13,14,15,16] between the paramagnetic centres. In some cases, also photon emission has been reported, which yields to the development of organic light-emitting diodes (OLEDs).[17-20] Overall, the paramagnetic units of these open-shell materials can act as magnetic centres and charge transport sites, sometimes at the same time, resulting in multifunctional materials, some of which displaying cross-effects, *e.g.* magnetoresistance,[21] being the latter of great interest for the development of organic spintronics.[22-26]

The incorporation of paramagnetic centres in organic systems has thus resulted in materials with a wide range of magnetic and electric properties, that stand as cheaper, lightweight and less environmentally harmful potential candidates to substitute conventional inorganic materials.[27-32] Furthermore, it

Document signat digitalment per: CRISTINA RONCERO BARRERO

has been shown that magnetic and electric properties can be finely tuned by modifications of the chemical backbone or applying an external stimulus[33] (*ie.* pressure or temperature), which will allow to aim at a given desired application once the ideal functionalization of the material has been figured. This is certainly an advantage when it comes to applications. Nevertheless, the prediction of such functionalization is far from trivial because chemical changes in molecular structure can affect both the molecular electronic structure and the crystal packing of the building blocks. For this reason, the rational design of new organic-radical based materials with specific technological applications is a challenging task. To this end, several complex aspects need to be taken into account simultaneously: (i) the electronic structure of the molecular building blocks (e.g. the degree of (de)localization of the unpaired electrons) and its changes upon chemical functionalization of a basic skeleton; (ii) the role of intermolecular interactions in shaping the electronic structure of the building blocks; (iii) which intermolecular interactions drive the crystal packing; (iv) the mechanisms of spin coupling and electron transport. Given the difficulty in characterizing and understanding all these factors on the exclusive basis of experimental data, it is clear that computational modeling can play a leading role in the rational design of new materials. Such computational modeling should focus on the use and development of multiscale models that encompass the microscopic effects of the molecular design and their resulting macroscopic property and, ultimately, analyse the possible structure-property correlations.

The paramagnetic nature of the building blocks makes these systems a challenge for quantum chemistry methods and models. The fact that the unpaired electrons sit in molecular orbitals of the spin-carrying units with the spin density smeared out across the molecule results in a great variety of options for the topology of the exchange coupling mechanism and conducting paths. However, it also results in a complex competition in the material between charge localisation (which would enhance magnetism) and charge transport (which would enhance conductivity). Furthermore, in radical molecular-based materials constituted by neutral organic radical building blocks (which reduce the cohesive

Document signat digitalment per: CRISTINA RONCERO BARRERO

forces in the crystal to dispersion or weak electrostatic interactions), interactions between partially delocalised unpaired electrons lead to a complex electronic structure that represents a tough challenge for most of the available computational methods.

The study of magnetism in molecular materials is computationally well established.[34] Specifically, the GEMM research group (Grup d'Estructura de Materials Moleculars) follows a working strategy whose initial step is the identifcation, and subsequent study, of the microscopic spin-spin interactions responsible for a given experimental magnetic property in organic open-shell molecular materials.[35] Therefore, despite specific problems that can arise from the chemical nature of the system under study, the macroscopic magnetic property of interest can be computed from first principles calculations using a bottom-up procedure.

Organic molecular materials are typically semiconductors with low electron mobility.[36] It is generally believed, due to the low values of mobility, that in these materials the hopping model dominates the charge transfer process. However, although these models have been successfully used in the description of closed-shell materials,[37] there are few studies available in the literature related to open-shell systems[38,39] and, as far as we know, none in which conductivity in open-shell organic molecular materials is computed from a hopping charge transfer model.

The aim of the doctoral project here submitted is, thus, the study of the different electric conductivities and magnetic behaviours that arise in four materials from a well-characterized family of bisdithiazolyl (bisDTA) derived compounds obtained after a series of S/Se substitutions.[40] Although there are a few studies that aim at evaluating J_{AB} magnetic interactions in these materials[41], the magnetic topology defined by all significant J_{AB} interactions has not yet been put forward, and no attempts to connect them with the macroscopic

Document signat digitalment per: CRISTINA RONCERO BARRERO

magnetic property have been neither reported. In this PhD dissertation, we have characterized the periodic electronic structure of these four bisDTA materials and studied, from a dimer cluster perspective, the microscopic interactions responsible for the magnetic and electric properties of the four selected bisDTA S/Se molecular materials.

The objectives of this thesis are:

- Understand the electronic structure and crystallographic packing of the four bisDTA-based materials of interest
- Rationalize the key microscopic contributions in the description of the experimental magnetic susceptibility.
- Evaluate the temperature effects on the crystal structure and, hence, on magnetism.
- Characterize the conduction paths after the evaluation of the λ reorganization energy and H_{AB} electronic coupling
- Reproduce the experimental conductivity data using Marcus hopping model.
- Assess the validity of the hopping mode in the description of electric conductivity in single-component radical semiconductors.
- Identification of structure-property correlations in bisDTA materials

The thesis here presented is structured as follows:

Firstly, Part I is an Introduction that consists in three Chapters. In particular, Chapter 1 (the current chapter) will provide a general overview of the relevance of the type of multifunctional systems, which are the target of this PhD thesis. The second chapter will present the *bisdithiazolyl-based* family of *materials*. In this chapter, the materials under study and their properties are described in detail. Finally, the working strategy, the theoretical framework and the models used in the study of the previous materials are introduced in chapter 3, which is entitled *models and methodology*.

Document signat digitalment per: CRISTINA RONCERO BARRERO

Part II is composed of the different results obtained for each of the objectives proposed. Chapter 4 is a benchmark study of the four selected bisDTA compounds in which the periodic electronic structure has been characterized. Thanks to DFT-UB3LYP spin-polarized calculations, a group of solutions with different spin arrangements has been studied, and the resultant ground states have been correlated with the experimental magnetic behaviour of the materials. From this analysis, a preliminary assessment of the relevant J_{AB} magnetic couplings has been also obtained, which has been compared with the full characterization of cluster models in Chapter 5. Then, in the same Chapter 5, the 3D magnetic topologies of the materials will be presented, together with the calculated macroscopic magnetic properties (magnetic susceptibility and critical temperature) computed at 100K, using the reported crystallographic data, and at 0 K, using DFT-optimized geometries. In the last chapter of results, in Chapter 6, the hopping model is employed to characterize the conduction paths and compute the macroscopic electric conductivity of all four bisDTA materials.

Finally, in Chapter 7, the conclusions of the thesis are reported based on the objectives presented in the first part.

1.1. References

1 Chen, Z. X., Li, Y., & Huang, F. (2021). Persistent and Stable Organic Radicals: Design, Synthesis, and Applications. Chem, 7(2), 288–332. https://doi.org/10.1016/j.chempr.2020.09.024

2 Wilcox, D. A., Agarkar, V., Mukherjee, S., & Boudouris, B. W. (2018). Stable Radical Materials for Energy Applications. https://doi.org/10.1146/annurev-chembioeng

3 Tan, Y., Hsu, S. N., Tahir, H., Dou, L., Savoie, B. M., & Boudouris, B. W. (2022). Electronic and Spintronic Open-Shell Macromolecules, Quo Vadis? In Journal of the American Chemical Society (Vol. 144, Issue 2, pp. 626–647). American Chemical Society. https://doi.org/10.1021/jacs.1c09815

Document signat digitalment per: CRISTINA RONCERO BARRERO

4 Ratera, I., & Veciana, J. (2012). Playing with organic radicals as building blocks for functional molecular materials. Chemical Society Reviews, 41(1), 303–349. https://doi.org/10.1039/c1cs15165g

5 Tang, B., Zhao, J., Xu, J. F., & Zhang, X. (2020). Tuning the stability of organic radicals: From covalent approaches to non-covalent approaches. In Chemical Science (Vol. 11, Issue 5, pp. 1192–1204). Royal Society of Chemistry. https://doi.org/10.1039/c9sc06143f

6 Ji, L., Shi, J., Wei, J., Yu, T., & Huang, W. (2020). Air-Stable Organic Radicals: New-Generation Materials for Flexible Electronics? In Advanced Materials (Vol. 32, Issue 32). Wiley-VCH Verlag. https://doi.org/10.1002/adma.201908015

7 Nakahara, K., Oyaizu, K., & Nishide, H. (2011). Organic Radical Battery Approaching Practical Use. Chemistry Letters, 40(3), 222–227. https://doi.org/10.1246/cl.2011.222

8 Nakahara, K., Iwasa, S., Satoh, M., Morioka, Y., Iriyama, J., Suguro, M., & Hasegawa, E. (2002). Rechargeable batteries with organic radical cathodes. Chemical Physics Letters, 359(5–6), 351–354. https://doi.org/10.1016/S0009-2614(02)00705-4

9 Wilcox, D. A., Agarkar, V., Mukherjee, S., & Boudouris, B. W. (2018). Stable Radical Materials for Energy Applications. https://doi.org/10.1146/annurev-chembioeng

10 Organic Radical Polymers. New Avenues in Organic Electronics, S. Mukherjee, B. W. Boudouris, Springer Briefs in Materials, Springer International Publishing, Cham, Switzerland 2017.

11 Hu, X., Wang, W., Wang, D., & Zheng, Y. (2018). The electronic applications of stable diradicaloids: Present and future. In Journal of Materials Chemistry C (Vol. 6, Issue 42, pp. 11232–11242). Royal Society of Chemistry. https://doi.org/10.1039/c8tc04484h

12 Sukegawa, T., Omata, H., Masuko, I., Oyaizu, K., & Nishide, H. (2014). Anionic polymerization of 4-methacryloyloxy-TEMPO using an MMA-capped initiator. ACS Macro Letters, 3(3), 240–243. https://doi.org/10.1021/mz400644y

13 Miller, J. S. (2014). Organic- and molecule-based magnets. Materials Today, 17(5), 224–235. https://doi.org/10.1016/j.mattod.2014.04.023

14 Winter, S. M., Hill, S., & Oakley, R. T. (2015). Magnetic Ordering and Anisotropy in Heavy Atom Radicals. Journal of the American Chemical Society, 137(11), 3720–3730. https://doi.org/10.1021/jacs.5b00672

15 Mahmood, J., Park, J., Shin, D., Choi, H.-J., Seo, J.-M., Yoo, J.-W., & Baek, J.-B. (2018). Organic Ferromagnetism: Trapping Spins in the Glassy State

Document signat digitalment per: CRISTINA RONCERO BARRERO

of an Organic Network Structure. Chem, 4(10), 2357–2369. https://doi.org/10.1016/j.chempr.2018.07.006

16 Phan, H., Herng, T. S., Wang, D., Li, X., Zeng, W., Ding, J., Loh, K. P., Shen Wee, A. T., & Wu, J. (2019). Room-Temperature Magnets Based on 1,3,5-Triazine-Linked Porous Organic Radical Frameworks. Chem, 5(5), 1223–1234. https://doi.org/10.1016/j.chempr.2019.02.024

17 Mayorga Burrezo, P., Jiménez, V. G., Blasi, D., Ratera, I., Campaña, A. G., & Veciana, J. (2019). Organic Free Radicals as Circularly Polarized Luminescence Emitters. Angewandte Chemie, 131(45), 16428–16434. https://doi.org/10.1002/ange.201909398

18 Peng, Q., Obolda, A., Zhang, M., & Li, F. (2015). Organic light-emitting diodes using a neutral π radical as emitter: The emission from a doublet. Angewandte Chemie - International Edition, 54(24), 7091–7095. https://doi.org/10.1002/anie.201500242

19 Obolda, A., Ai, X., Zhang, M., & Li, F. (2016). Up to 100% Formation Ratio of Doublet Exciton in Deep-Red Organic Light-Emitting Diodes Based on Neutral π-Radical. ACS Applied Materials and Interfaces, 8(51), 35472–35478. https://doi.org/10.1021/acsami.6b12338 [mateix material que la ref 12?-mirar numero paper cond.]

20 Ai, X., Evans, E. W., Dong, S., Gillett, A. J., Guo, H., Chen, Y., Hele, T. J. H., Friend, R. H., & Li, F. (2018). Efficient radical-based light-emitting diodes with doublet emission. Nature, 563(7732), 536–540. https://doi.org/10.1038/s41586-018-0695-9

21 Komatsu, H., Matsushita, M. M., Yamamura, S., Sugawara, Y., Suzuki, K., & Sugawara, T. (2010). Influence of Magnetic Field upon the Conductance of a Unicomponent Crystal of a Tetrathiafulvalene-Based Nitronyl Nitroxide. Journal of the American Chemical Society, 132(13), 4528–4529. https://doi.org/10.1021/ja9109538

22 Gopalakrishna, T. Y., Zeng, W., Lu, X., & Wu, J. (2018). From open-shell singlet diradicaloids to polyradicaloids. Chemical Communications, 54(18), 2186–2199. https://doi.org/10.1039/c7cc09949e

23 Sugawara, T., Komatsu, H., & Suzuki, K. (2011). Interplay between magnetism and conductivity derived from spin-polarized donor radicals. In Chemical Society Reviews (Vol. 40, Issue 6, pp. 3105–3118). https://doi.org/10.1039/c0cs00157k

24 Hayakawa, R., Karimi, M. A., Wolf, J., Huhn, T., Zöllner, M. S., Herrmann, C., & Scheer, E. (2016). Large Magnetoresistance in Single-Radical Molecular Junctions. Nano Letters, 16(8), 4960–4967. https://doi.org/10.1021/acs.nanolett.6b01595

Document signat digitalment per: CRISTINA RONCERO BARRERO

25 Herrmann, C., Solomon, G. C., & Ratner, M. A. (2010). Organic radicals as spin filters. Journal of the American Chemical Society, 132(11), 3682–3684. https://doi.org/10.1021/ja910483b

26 Shil, S., Bhattacharya, D., Misra, A., & Klein, D. J. (2015). A high-spin organic diradical as a spin filter. Physical Chemistry Chemical Physics, 17(36), 23378–23383. https://doi.org/10.1039/c5cp03193a

27 DOE, Critical Supply Strategy, 2011, https://www.energy.gov/sites/prod/files/DOE_CMS2011_FINAL_Full.pdf

28 DOE, Critical Supply Strategy, 2021, https://www.energy.gov/sites/prod/files/2021/01/f82/DOE%20Critical%20Minerals%20and%20Materials%20Strategy_0.pdf

29 European Raw Materials Alliance, Rare Earth Magnets and Motors: A European Call for Action, 2021, https://eitrawmaterials.eu/wpcontent/uploads/2021/09/ERMA-Action-Plan-2021-AEuropean-Call-for-Action.pdf

30 Balaram, V. (2019). Rare earth elements: A review of applications, occurrence, exploration, analysis, recycling, and environmental impact. Geoscience Frontiers, 10(4), 1285–1303. https://doi.org/10.1016/j.gsf.2018.12.005

31 Boudouris BW. 2013. Engineering optoelectronically active macromolecules for polymer-based photo-voltaic and thermoelectric devices.Curr. Opin. Chem. Eng.2(3):294–301

32 Root SE, Savagatrup S, Printz AD, Rodriquez D, Lipomi DJ. 2017. Mechanical properties of organic semiconductors for stretchable, highly flexible, and mechanically robust electronics.Chem. Rev.117:6467–99

33 Yuan, D., Liu, W., & Zhu, X. (2021). Design and Applications of Single-Component Radical Conductors. Chem, 7(2), 333–357. https://doi.org/10.1016/j.chempr.2020.10.001

34 Novoa, J. J., Deumal, M., & Jornet-Somoza, J. (2011). Calculation of microscopic exchange interactions and modelling of macroscopic magnetic properties in molecule-based magnets. Chemical Society Reviews, 40(6), 3182–3212. https://doi.org/10.1039/c0cs00112k

35 Deumal, M., Vela, S., Fumanal, M., Ribas-Arino, J., & Novoa, J. J. (2021). Insights into the magnetism and phase transitions of organic radical-based materials. In Journal of Materials Chemistry C (Vol. 9, Issue 33, pp. 10624–10646). Royal Society of Chemistry. https://doi.org/10.1039/d1tc01376a

36 Oberhofer, H., Reuter, K., & Blumberger, J. (2017). Charge Transport in Molecular Materials: An Assessment of Computational Methods. Chemical Reviews, 117(15), 10319–10357.

37 Yavuz, I., Martin, B. N., Park, J., & Houk, K. N. (2015). Theoretical study of the molecular ordering, paracrystallinity, and charge mobilities of

Document signat digitalment per: CRISTINA RONCERO BARRERO

oligomers in different crystalline phases. Journal of the American Chemical Society, 137(8), 2856–2866.

38 Tan, Y., Casetti, N. C., Boudouris, B. W., & Savoie, B. M. (2021). Molecular Design Features for Charge Transport in Nonconjugated Radical Polymers. *Journal of the American Chemical Society*, *143*(31), 11994–12002. https://doi.org/10.1021/jacs.1c02571

39 Kushida, T., Shirai, S., Ando, N., Okamoto, T., Ishii, H., Matsui, H., Yamagishi, M., Uemura, T., Tsurumi, J., Watanabe, S., Takeya, J., & Yamaguchi, S. (2017). Boron-Stabilized Planar Neutral π-Radicals with Well-Balanced Ambipolar Charge-Transport Properties. Journal of the American Chemical Society, 139(41), 14336–14339. https://doi.org/10.1021/jacs.7b05471

40 Robertson, C. M., Leitch, A. A., Cvrkalj, K., Reed, R. W., Myles, D. J. T., Dube, P. A., Oakley, R. T., & Ls, O. (2008). Enhanced conductivity and magnetic ordering in isostructural heavy atom radicals. *Journal of the American Chemical Society*, *130*(26), 8414–8425.

41 Deumal, M., Rawson, J. M., Goeta, A. E., Howard, J. A. K., Copley, R. C. B., Robb, M. A., & Novoa, J. J. "Studying the Origin of the Antiferromagnetic to Spin-Canting Transition in the ß-p-NCC6F4CNSSN. Molecular Magnet.", Chem. Eur. J., 2010, 16(9), 2741–2750.

Document signat digitalment per: CRISTINA RONCERO BARRERO

Document signat digitalment per: CRISTINA RONCERO BARRERO

Chapter 2. Bisdithiazolyl-Based Materials

Single-component radical conductors[1] made of planar organic radicals base its conductivity on taking profit of the unpaired electrons, which provides with spin for the magnetic interaction and charge for electric conduction, and on the efficiency of the π-stacking as conduction pathway. However, due to the high reactivity of radicals, they usually suffer from dimerization under ambient conditions, which quenches their conductivity and magnetism, and need bulky substituents in order to protect the paramagnetic centre. In this field, bisdithiazolyl (bisDTA) derivatives have been found to be a promising building block to construct single-component radical conductors. First attempts showed no evidence of dimerization, mainly thanks to the spin delocalization displayed by these radicals, which is enhanced by a resonance interaction between their two DTA rings. Besides the stabilization by means of spin delocalization, a judicious selections of substituents attached to the radicals can provide extra protection through steric hindrance. However, the protection provided by bulky substituents has the side effect of distorting the π-stacking alignment that would interfere with the radical-radical contacts and, hence, despite the close lateral S···S contacts, hinders the long-range transport and thus conductivity would remain low ($\sigma \sim 10^{-7}$ - 10^{-5} S·cm^{-1} at 300 K).

In a quest to improve their conductivity, experimentalists have synthetized a long list of bisDTA-derivatives following three different synthetic strategies. (see Appendix 1 for a compendium of the bisDTA synthetized compounds found in the literature). The first route consists of varying the central ring, leading to pyridine[2-8], pyrazine [9,10], semiquinone [11,-18] and

Document signat digitalment per: CRISTINA RONCERO BARRERO

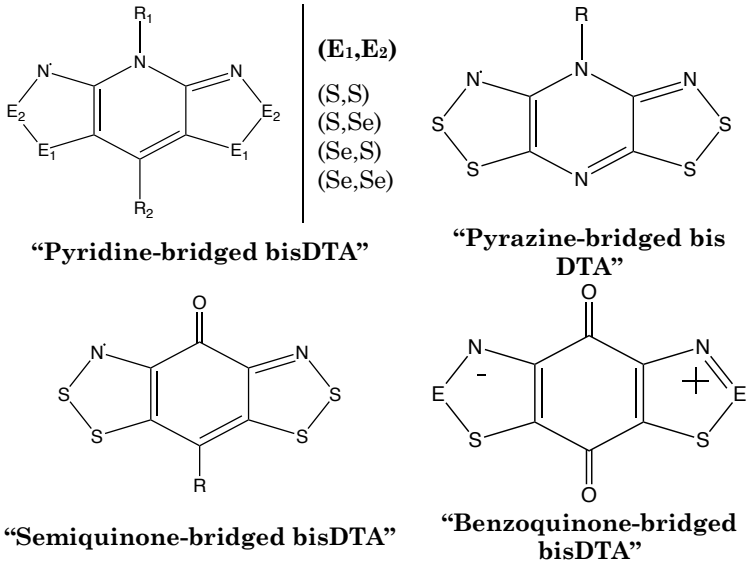

Figure 2.1. Chemical structures of bisDTA-derivatives.

benzoquinone[19,20] derivatives (see chemical skeletons in Figure 2.1). Secondly, the effects of the interplanar distance (∂) and slippage were also explored to obtain efficient conduction channels by modifying the bulky substituent of the above-mentioned central ring (see R or R_1,R_2 in Figure 2.1)[2,5,12,21-24]. Finally, the third strategy is based on the substitution of the S atoms of the central ring by a heavier alternative, such as Se. [5,21,23-25-30] Note that substitution by a larger heteroatom is believed to enhance conductivity thanks to a better orbital overlap, that will facilitate the charge migration between sites and, thus, increase conductivity. Following either one of these strategies or a combination of them, the family of compounds has more than 50 members, whose conductive properties range from insulator [2,25] to metallic conductor [12,13,19,20,24,].

Additionally, when dimerization is prevented, the spin of the unpaired electron gifts the material with magnetic properties, including weak/moderate ferromagnetism and antiferromagnetism[2-5,8,16,26,]. In fact, both the spin and the charge provided by the unpaired electrons, which translate into magnetic interactions and electric conductivity, may results in an entanglement between charge and spin carriers of potential application in the development of spintronic

Document signat digitalment per: CRISTINA RONCERO BARRERO

a)

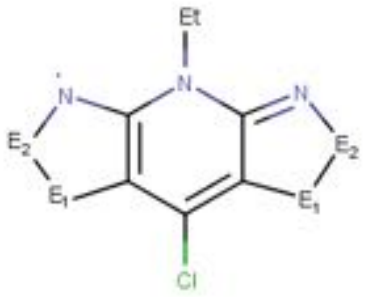

b)

	E_a (eV)	σ (S cm^{-1}) [T=300K]	Magnetic properties at low T	T_c (K)
(S,S)	0.43	$3.2 \cdot 10^{-6}$	No long-range order	--
(S,Se)	0.27	$1.0 \cdot 10^{-4}$	Bulk FM	12.8
(Se,S)	0.31	$2.2 \cdot 10^{-5}$	Spin-canted AFM	14.0
(Se,Se)	0.19	$3.0 \cdot 10^{-4}$	Bulk FM	17.0

Figure 2.2. Radicals are classified according to whether E_1 and E_2 positions are S or Se atoms. In the following, radicals will be referred to as (E_1,E_2), namely, as pure (S,S) (i.e. bisdithiazolyl) radical, mixed thiaselenazolyl (S,Se) and (Se,S) radicals, and pure (Se,Se) (i.e. bisdiselenazolyl) radical. Experimental magnetic behaviour at low temperature and critical temperatures (T_c) are extracted from ref. [29]

materials. On the other hand, it has been observed, both experimentally and computationally, that both macroscopic properties are strongly affected by the molecular packing, which can be easily modified by means of crystal engineering as a result of weak electrostatic and dispersion interactions between bisDTA radicals. Computationally, all these features, namely the highly sensitive dependence between structure and properties and the interconnection between charge localization and delocalization in the radicals, make the study of the magnetic and conducting properties of these systems a challenge for the actual models and computational methods.

In order to establish a working strategy for the study of both conductivity and magnetism in this kind of materials, we have selected four isostructural materials out of the huge bisDTA family (see Figure 2.2). Specifically, we have chosen four crystals that derive from pyridine-bridged bisDTA with Ethyl and Chlorine as substituents of the central-fused ring (see R_1 and R_2 for substituents in Figure 2.1, and E_1 and E_2 positions for S/Se heavy atoms in Figure 2.2a). To simplify the discussion and comparison along this work, the 4 materials have been named as (E_1,E_2) after the atoms that occupy the E_1 and E_2 positions. Accordingly, the bisdithiazolyl material will be referred to as (S,S) (E_1=S and E_2=S), the bisdiselenazolyl as (Se,Se), and the two mixed thiaselenazolyl compounds as (S,Se) and (Se,S). These four materials have been chosen mainly

Document signat digitalment per: CRISTINA RONCERO BARRERO

for two reasons: (1) they present very distinct physical properties while sharing the same crystallographic space group (and hence crystal packing), and (2) there is a full experimental characterization[29] of their crystallographic data (room temperature, 100K, 2K) and properties (χ magnetic susceptibility, C_p critical temperature and σ electric conductivity).

Regarding physical properties, they exhibit interesting magnetic properties (ranging from no long-range order to bulk ferromagnetism), and different conductivity (σ varies two orders of magnitude) (see Table in Figure 2.2b). It is experimentally observed that conductivity increases with the Se content. However, comparing both mixed (S,Se) and (Se,S) materials, an interesting dependence with the relative position of the heteroatoms arises. This dependence is also noticeable in their magnetism. Magnetic interactions seem to increase with the S/Se ratio: Se E_2-substituted materials present a bulk ferromagnet ordering at low temperatures, while Se in E_1 position results in an antiferromagnet material with experimental evidences of spin-canting.[28] As mentioned, in addition to these different intriguing physical properties, the four bisDTA-derivatives share the same crystallographic space group with $P\bar{4}2_1m$ symmetry. Therefore, it will be possible to apply an analogous computational strategy to all four materials and compare the results obtained trying to elucidate and disentangle the effects that could explain the magnetic and conductivity response observed experimentally.

Concerning the $P\bar{4}2_1m$ tetragonal crystal packing, it must be stressed that the unit cell consists of 4 columns of π-stacked radicals rotating around a central C_4 symmetry axis (see Figure 2.3a). Stacked molecules are tilted with respect to the c-axis, which is the stacking direction. As a result of this tilting, radicals are not eclipsed but there is a slippage along the central symmetry plane of the monomer (longitudinal slippage, *dy*)(see F, a feature that will be important in the description of the interactions along this direction.[22,30] As a result, radicals

Document signat digitalment per: CRISTINA RONCERO BARRERO

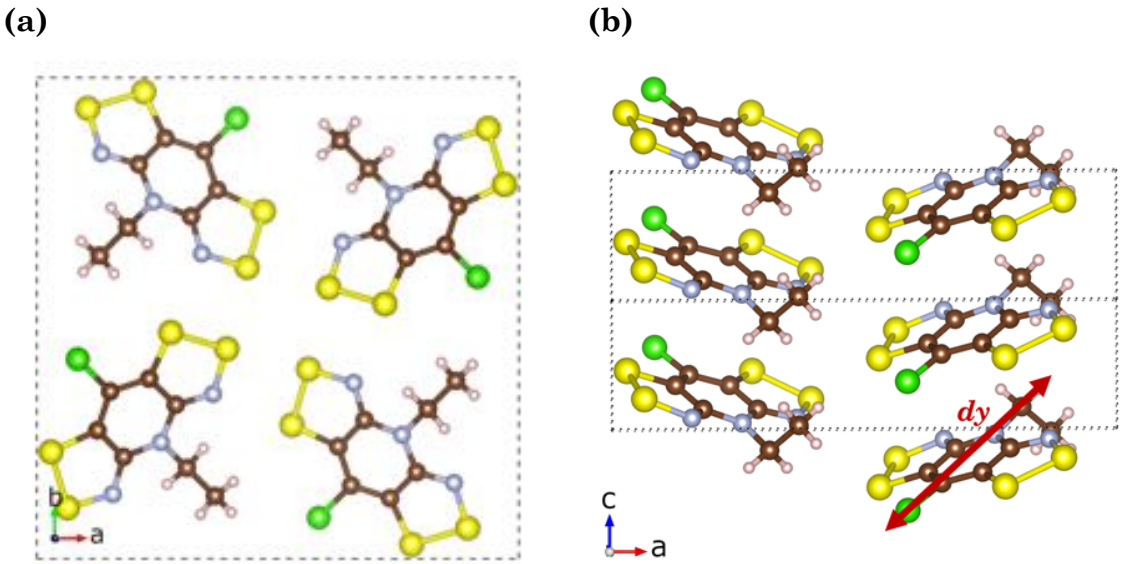

Figure 2.3. Crystal packing of (S,S) material. (a) top *ab*-planes view and (b) *c*-axis view, parallel to the π-stacking direction. All four bisDTA derivatives under study present equivalent crystallographic structures. Note that longitudinal slippage (*dy*) has been represented using a red arrow in (b).

are not perfectly aligned and form staggered columns (see Figure 2.3b), which may improve the lateral interactions enhancing their potential leading role in the description of their conductivity and magnetism. In fact, experimentalists have highlighted the relevance of the intermolecular $E_2 \cdots E_2$ contacts (see Figure 2.4) in the description of the conductivity for bisDTA compounds, showing that –upon distance contraction– the values of σ increase substantially.[29]

It is important to point out that crystal packing of neutral open-shell molecular species depends on the balance of several weak interactions, that can be easily affected by external stimulus, like pressure[15,25] or temperature[31]. In the literature, some already published works tackle the rationalization of the effect of such external stimuli on the magnetic response and crystal packing[30,32]. However, despite previously reported experimental evidences and computational studies for bisDTA multifunctional compounds, microscopic magnetic interactions and their macroscopic effect have not yet been connected. Additionally, the complexity of the crystal packing invalidates the assumption of a charge transport and/or magnetic topology simply governed by the π-stacking

Document signat digitalment per: CRISTINA RONCERO BARRERO

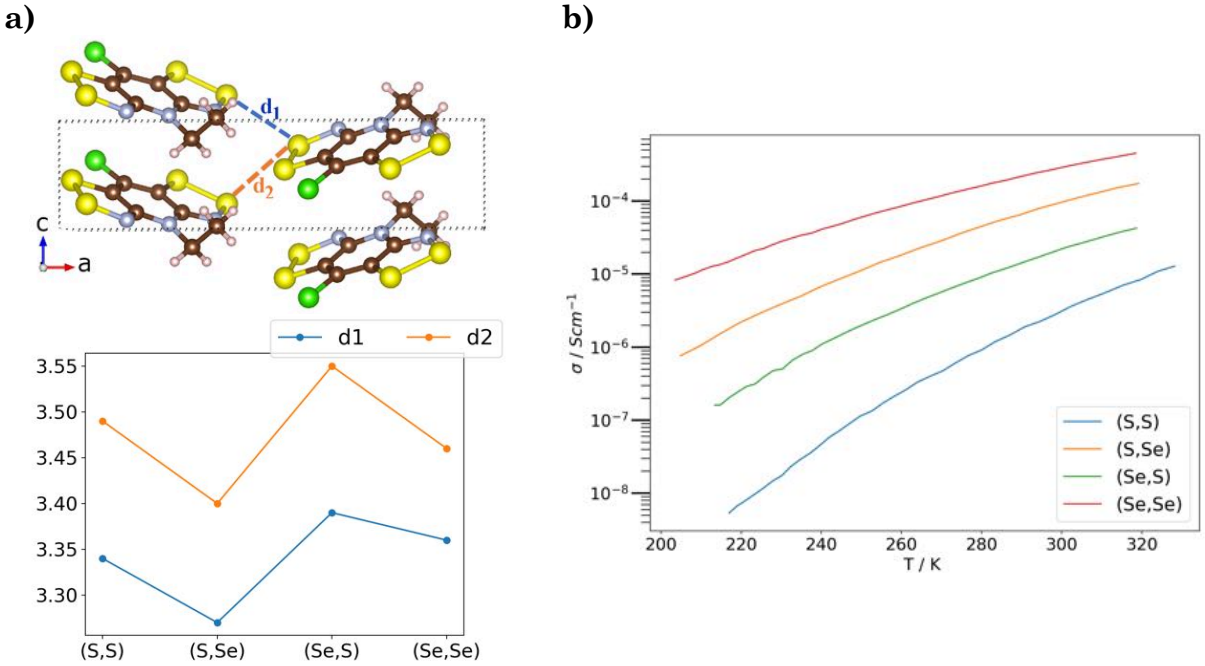

Figure 1.4. (a) Intermolecular $E_2\cdots E_2$ contacts, *i.e.* d_1 and d_2 (see top image for schematic representation) as a function of the four bisDTA materials. (b) log (σ) versus T plots.

radical···radical interactions and demands of a complete radical···radical mapping of all possible non-negligible contacts.

Our primary goal, as has been outlined in the previous chapter, will thus be to disentangle the different microscopic contributions to the macroscopic response (i.e. magnetism and conductivity). The evaluation of these microscopic interactions together with an analysis of the geometry variations due to S/Se substitutions and/or heating/cooling will serve as a starting point to establish structure-property correlations. Furthermore, the study of this well-characterized family of isostructural materials will help to settle a working strategy for the simulation of electric conductivity in organic open-shell molecular crystals.

Overall, electronic structure effects due to S/Se substitution, crystal packing and temperature influence merge together in the description of these four complex organic single-component multifunctional bisDTA materials.

Document signat digitalment per: CRISTINA RONCERO BARRERO

2.1. References

1 Yuan, D., Liu, W., & Zhu, X. (2021). Design and Applications of Single-Component Radical Conductors. Chem, 7(2), 333–357. https://doi.org/10.1016/j.chempr.2020.10.001

2 Beer, L., Brusso, J. L., Cordes, A. W., Haddon, R. C., Itkis, M. E., Kirschbaum, K., MacGregor, D. S., Oakley, R. T., Pinkerton, A. A., & Reed, R. W. (2002). Resonance-Stabilized 1,2,3-Dithiazolo-1,2,3-dithiazolyls as Neutral π-Radical Conductors. Journal of the American Chemical Society, 124(32), 9498–9509. https://doi.org/10.1021/ja026118s

3 Beer, L., Brusso, J. L., Cordes, A. W., Godde, E., Haddon, R. C., Itkis, M. E., Oakley, R. T., & Reed, R. W. (2002). Structure-property trends in π-stacked dithiazolo-dithiazolyl conductors. Chemical Communications, 21, 2562–2563. https://doi.org/10.1039/b207735n

4 Beer, L., Britten, J. F., Clements, O. P., Haddon, R. C., Itkis, M. E., Matkovich, K. M., Oakley, R. T., & Reed, R. W. (2004). Dithiazolodithiazolyl Radicals: Substituent Effects on Solid State Structures and Properties. Chemistry of Materials, 16(8), 1564–1572. https://doi.org/10.1021/cm035191u

5 Brusso, J. L., Derakhshan, S., Itkis, M. E., Kleinke, H., Haddon, R. C., Oakley, R. T., Reed, R. W., Richardson, J. F., Robertson, C. M., & Thompson, L. K. (2006). Isostructural bisdithiazolyl and bisthiaselenazolyl radicals: Trends in bandwidth and conductivity. Inorganic Chemistry. https://doi.org/10.1021/ic061687c

6 Lekin, K., Winter, S. M., Downie, L. E., Bao, X., Tse, J. S., Desgreniers, S., Secco, R. A., Dube, P. A., & Oakley, R. T. (2010). Hysteretic spin crossover between a bisdithiazolyl radical and its hypervalent σ-dimer. Journal of the American Chemical Society, 132(45), 16212–16224 . https://doi.org/10.1021/ja106768z

7 Lekin, K., Phan, H., Winter, S. M., Wong, J. W. L. L., Leitch, A. A., Laniel, D., Yong, W., Secco, R. A., Tse, J. S., Desgreniers, S., Dube, P. A., Shatruk, M., & Oakley, R. T. (2014). Heat, pressure and light-induced interconversion of bisdithiazolyl radicals and dimers. Journal of the American Chemical Society, 136(22), 8050–8062. https://doi.org/10.1021/ja502753t

8 Lekin, K., Wong, J. W. L., Winter, S. M., Mailman, A., Dube, P. A., & Oakley, R. T. (2013). Bisdithiazolyl Radical Spin Ladders. Inorganic Chemistry, 52(4), 2188–2198. https://doi.org/10.1021/ic302658c

9 Leitch, A. A., McKenzie, C. E., Oakley, R. T., Reed, R. W., Richardson, J. F., & Sawyer, L. D. (2006). Bimodal association of a bis-1,2,3-dithiazolyl

Document signat digitalment per: CRISTINA RONCERO BARRERO

radical. Chemical Communications, 10, 1088–1090. https://doi.org/10.1039/b517098b

10 Leitch, A. A., Reed, R. W., Robertson, C. M., Britten, J. F., Yu, X., Secco, R. A., & Oakley, R. T. (2007). An alternating π-stacked bisdithiazolyl radical conductor. Journal of the American Chemical Society, 129(25), 7903–7914. https://doi.org/10.1021/ja071218p

11 Yu, X., Mailman, A., Dube, P. A., Assoud, A., & Oakley, R. T. (2011). First semiquinone-bridged bisdithiazolyl radical conductor: A canted antiferromagnet displaying a spin-flop transition. Chemical Communications, 47(16), 4655–4657. https://doi.org/10.1039/c1cc10598a

12 Mailman, A., Winter, S. M., Yu, X., Robertson, C. M., Yong, W., Tse, J. S., Secco, R. A., Liu, Z., Dube, P. A., Howard, J. A. K., & Oakley, R. T. (2012). Crossing the insulator-to-metal barrier with a thiazyl radical conductor. Journal of the American Chemical Society, 134(24), 9886–9889. https://doi.org/10.1021/ja303169y

13 Yu, X., Mailman, A., Lekin, K., Assoud, A., Robertson, C. M., Noll, B. C., Campana, C. F., Howard, J. A. K. K., Dube, P. A., & Oakley, R. T. (2012). Semiquinone-bridged bisdithiazolyl radicals as neutral radical conductors. Journal of the American Chemical Society, 134(4), 2264–2275. https://doi.org/10.1021/ja209841z

14 Wong, J. W. L., Mailman, A., Lekin, K., Winter, S. M., Yong, W., Zhao, J., Garimella, S. v., Tse, J. S., Secco, R. A., Desgreniers, S., Ohishi, Y., Borondics, F., & Oakley, R. T. (2014). Pressure induced phase transitions and metallization of a neutral radical conductor. Journal of the American Chemical Society, 136(3), 1070–1081. https://doi.org/10.1021/ja411057x

15 Mailman, A., Wong, J. W. L., Winter, S. M., Claridge, R. C. M., Robertson, C. M., Assoud, A., Yong, W., Steven, E., Dube, P. A., Tse, J. S., Desgreniers, S., Secco, R. A., & Oakley, R. T. (2017). Fine Tuning the Performance of Multiorbital Radical Conductors by Substituent Effects. Journal of the American Chemical Society. https://doi.org/10.1021/jacs.6b11779

16 Mailman, A., Robertson, C. M., Winter, S. M., Dube, P. A., & Oakley, R. T. (2019). The Importance of Electronic Dimensionality in Multiorbital Radical Conductors. Inorganic Chemistry, 58(9), 6495–6506. https://doi.org/10.1021/acs.inorgchem.9b00691

17 Yu, X., Mailman, A., Lekin, K., Assoud, A., Dube, P. A., & Oakley, R. T. (2012). A bimodal oxobenzene-bridged bisdithiazolyl radical conductor. Crystal Growth and Design, 12(5), 2485–2494. https://doi.org/10.1021/cg300107t

18 Mailman, A., Winter, S. M., Wong, J. W. L., Robertson, C. M., Assoud, A., Dube, P. A., & Oakley, R. T. (2015). Multiple orbital effects and magnetic ordering in a neutral radical. Journal of the American Chemical Society, 137(3), 1044–1047. https://doi.org/10.1021/ja512235h

Document signat digitalment per: CRISTINA RONCERO BARRERO

19 Mailman, A., Leitch, A. A., Yong, W., Steven, E., Winter, S. M., Claridge, R. C. M., Assoud, A., Tse, J. S., Desgreniers, S., Secco, R. A., & Oakley, R. T. (2017). The Power of Packing: Metallization of an Organic Semiconductor. Journal of the American Chemical Society, 139(6), 2180–2183. https://doi.org/10.1021/jacs.6b12814

20 Lekin, K., Leitch, A. A., Assoud, A., Yong, W., Desmarais, J., Tse, J. S., Desgreniers, S., Secco, R. A., & Oakley, R. T. (2018). Benzoquinone-Bridged Heterocyclic Zwitterions as Building Blocks for Molecular Semiconductors and Metals. Inorganic Chemistry, 57(8), 4757–4770. https://doi.org/10.1021/acs.inorgchem.8b00485

21 Wong, J. W. L., Mailman, A., Winter, S. M., Robertson, C. M., Holmberg, R. J., Murugesu, M., Dube, P. A., & Oakley, R. T. (2014). Supramolecular architecture, crystal structure and transport properties of the prototypal oxobenzene- bridged bisdithiazolyl radical conductor. Chem. Commun. Chem. Commun, 50(50), 785–787. https://doi.org/10.1039/c3cc46686h

22 Robertson, C. M., Leitch, A. A., Cvrkalj, K., Myles, D. J. T. T., Reed, R. W., Dube, P. A., & Oakley, R. T. (2008). Ferromagnetic ordering in bisthiaselenazolyl radicals: Variations on a tetragonal theme. Journal of the American Chemical Society, 130(44), 14791–14801. https://doi.org/10.1021/ja8054436

23 Tse, J. S., Leitch, A. A., Yu, X., Bao, X., Zhang, S., Liu, Q., Jin, C., Secco, R. A., Desgreniers, S., Ohishi, Y., & Oakley, R. T. (2010). Metallization of a hypervalent radical dimer: Molecular and band perspectives. Journal of the American Chemical Society, 132(13), 4876–4886. https://doi.org/10.1021/ja100216c

24 Leitch, A. A., Lekin, K., Winter, S. M., Downie, L. E., Tsuruda, H., Tse, J. S., Mito, M., Desgreniers, S., Dube, P. A., Zhang, S., Liu, Q., Jin, C., Ohishi, Y., & Oakley, R. T. (2011). From magnets to metals: The response of tetragonal bisdiselenazolyl radicals to pressure. Journal of the American Chemical Society, 133(15), 6050–6060. https://doi.org/10.1021/ja200391j

25 Beer, L., Brusso, J. L., Haddon, R. C., Itkis, M. E., Kleinke, H., Leitch, A. A., Oakley, R. T., Reed, R. W., Richardson, J. F., Secco, R. A., & Yu, X. (2005). Pressure enhanced conductivity in bis-1,2,3-thiaselenazolyl dimers. Journal of the American Chemical Society. https://doi.org/10.1021/ja055122b

26 Brusso, J. L., Cvrkalj, K., Leitch, A. A., Oakley, R. T., Reed, R. W., & Robertson, C. M. (2006). Resonance stabilized bisdiselenazolyls as neutral radical conductors. Journal of the American Chemical Society, 128(47), 15080–15081. https://doi.org/10.1021/ja0666856

27 Leitch, A. A., Brusso, J. L., Cvrkalj, K., Reed, R. W., Robertson, C. M., Dube, P. A., & Oakley, R. T. (2007). Spin-canting in heavy atom heterocyclic radicals. https://doi.org/10.1039/b708756j

Document signat digitalment per: CRISTINA RONCERO BARRERO

28 Robertson, C. M., Myles, D. J. T., Leitch, A. A., Reed, R. W., Dooley, B. M., Frank, N. L., Dube, P. A., Thompson, L. K., & Oakley, R. T. (2007). Ferromagnetism in a heavy atom heterocyclic radical conductor. Journal of the American Chemical Society. https://doi.org/10.1021/ja076841o

29 Robertson, C. M., Leitch, A. A., Cvrkalj, K., Reed, R. W., Myles, D. J. T., Dube, P. A., Oakley, R. T., & Ls, O. (2008). Enhanced conductivity and magnetic ordering in isostructural heavy atom radicals. Journal of the American Chemical Society, 130(26), 8414–8425. https://doi.org/10.1021/ja801070d

30 Leitch, A. A., Yu, X., Winter, S. M., Secco, R. A., Dube, P. A., Oakley, R. T., & Ls, O. (2009). Structure and property correlations in heavy atom radical conductors. Journal of the American Chemical Society, 131(20), 7112–7125. https://doi.org/10.1021/ja900853t

31 Robertson, C. M., Winter, S. M., Howard, J. A. K., Probert, M. R., & Oakley, R. T. (2021). Low temperature insights into the crystal and magnetic structure of a neutral radical ferromagnet. Chemical Communications, 1(c). https://doi.org/10.1039/d1cc03842g

32 Winter, S. M., Hill, S., & Oakley, R. T. (2015). Magnetic Ordering and Anisotropy in Heavy Atom Radicals. Journal of the American Chemical Society, 137(11), 3720–3730. https://doi.org/10.1021/jacs.5b00672

Document signat digitalment per: CRISTINA RONCERO BARRERO

Chapter 3. Models And Methodology

In this chapter, the theory and models used in the calculations of the magnetic and electric macroscopic properties of interest of the systems presented in the previous section will be outlined. However depicted in two separate subsections for clarity, the *in silico* measure of magnetism and conductivity share a common fundamental idea: the evaluation of the microscopic interactions that give rise to the macroscopic property of interest. The study of microscopic interactions and their correlations with structural parameters gives valuable insight for the prediction of properties and guide the design of molecule-based solids.

3.1 Modelling macroscopic magnetic properties.

Macroscopic magnetic properties of molecular materials can be studied and rationalized starting from a microscopic analysis of the individual radical···radical interactions. In order to fully understand the macroscopic phenomena, a complete characterization of the microscopic interactions is key, as well as their interconnections and propagation through the crystal. Geometrical information and microscopic magnetic interactions have to be correctly correlated using the quantum and computational techniques available to study chemical systems. With this aim, in order to characterize the magnetic interactions and elucidate possible structural-property correlations, a study of the magnetic properties of the four bisDTA S/Se materials, presented in the previous chapter, has been carried out following a first-principles bottom-up (FPBU) working strategy.[1,2]

The FPBU procedure is a systematic unbiased (without any previous assumptions) 4 steps working strategy. First, a complete inspection of the crystal is carried out in order to select all the potential non-negligible magnetic

Document signat digitalment per: CRISTINA RONCERO BARRERO

exchange interactions (J_{AB}). The evaluation of all J_{AB} is then performed and the magnetic topology is defined based on the most significant J_{AB} couplings. Third, the minimal magnetic model is extracted from this magnetic topology, and used to obtain the energy spectra after full diagonalization of the secular equation of the system under study. Finally, the macroscopic property of interest is computed and compared to the experimental data (if available). Next each step will be briefly discussed.

3.1.1 Crystal analysis and screening of all potential non-negligible J_{AB}

The first step is the analysis of the crystal packing and the extraction of all the possible radical⋯radical interactions that might establish magnetic coupling. Usually, the preliminary study of the radical building block of the molecular material and its singly occupied molecular orbital (SOMO) gives information about the potentially relevant magnetic contacts. This is due to the fact that the overlap between the SOMO of the two radicals and their relative orientation is key for the resultant magnetic interaction. From this inspection, a criterion of selection, usually an intermolecular distance, is chosen and all the radical pairs under a certain representative threshold are extracted for their J_{AB} evaluation. It has been shown that J_{AB} decreases exponentially with the inter-radical distances, which means that in most cases only first neighbours are relevant.[3]

3.1.2 Evaluation of radical⋯radical J_{AB}

Once all the possible radical pair candidates to present a relevant magnetic interaction have been selected, the next step is the evaluation of J_{AB} for each pair. Thanks to the spin localization on each radical that makes them act as spin centres, the evaluation of the magnetic interactions can be carried out with a general Heisenberg Hamiltonian (also known as Heisenberg-Dirac-VanVleck Hamiltonian, HDVV)[4,5]. This phenomenological Hamiltonian describes the magnetic interactions between N paramagnetic centres as a sum over all the pairwise interactions:

Document signat digitalment per: CRISTINA RONCERO BARRERO

$$\widehat{H} = -2\sum_{A,B}^{N} J_{AB}\widehat{\boldsymbol{S}}_{\boldsymbol{A}} \cdot \widehat{\boldsymbol{S}}_{\boldsymbol{B}} \qquad \text{Eq. 3.1.}$$

where $\hat{S}$ is the spin operator of each "A" and "B" radicals and J_{AB} represents the magnetic exchange interaction (or coupling) between them. In the general case of a simple cluster model of two spin centres "A" and "B" with S_A=S_B, and knowing that the total spin operator $\hat{S}^2$ can be expressed as:

$$\widehat{\boldsymbol{S}}^{\boldsymbol{2}} = (\hat{S}_A + \hat{S}_B)^2 = \hat{S}_A^2 + \hat{S}_B^2 + 2\hat{S}_A\hat{S}_B \qquad \text{Eq. 3.2.}$$

the difference between two consecutive S and S-1 eigenvalues can be generalized as:

$$E(S) - E(S-1) = -2J_{AB}S \qquad \text{Eq. 3.3.}$$

The total S of all the possible states will take values ranging from S+S to $|S\text{-}S|$ in increments of -1 and each S state will have a multiplicity of 2S+1. In the present case, since any two interacting centres have S_A=S_B=1/2, their states can take two possible multiplicities, namely singlet (S=0) and triplet (S=1). In the case of two electrons in two orbitals (see Figure 3.1), accounting for all the possible permutations, a total of six electronic configurations (or Slater determinants) can be obtained: a singlet state (S=0, $^1\Psi_{S1}$), a singly- ($^1\Psi_{S3}$) and doubly- ($^1\Psi_{S2}$) excited singlet states and a triplet state of three components, namely the three possible configurations of m_S = +1 ($^3\Psi_T(1)$), 0 ($^3\Psi_T(3)$) and -1 ($^3\Psi_T(2)$). Accordingly, J_{AB} can be computed as a function of the two lowest energy states of different multiplicity, namely the triplet and lowest singlet states as Eq. 3.4.

$$J_{AB} = \frac{E_S - E_T}{2} \qquad \text{Eq. 3.4.}$$

Regarding the sign of J_{AB}, it is known that the energies of bonding states are negative, being the most stable the lowest one, and that the energy is strictly 0 in the case of two non-interacting centres at infinite distance. Therefore, using the HDVV Hamiltonian defined in Eq. 3.1, a singlet ground state will imply J_{AB}<0 defining the interaction as antiferromagnetic (AFM). Contrary, if the triplet state is more stable, the magnetic centres will be coupled ferromagnetically

Document signat digitalment per: CRISTINA RONCERO BARRERO

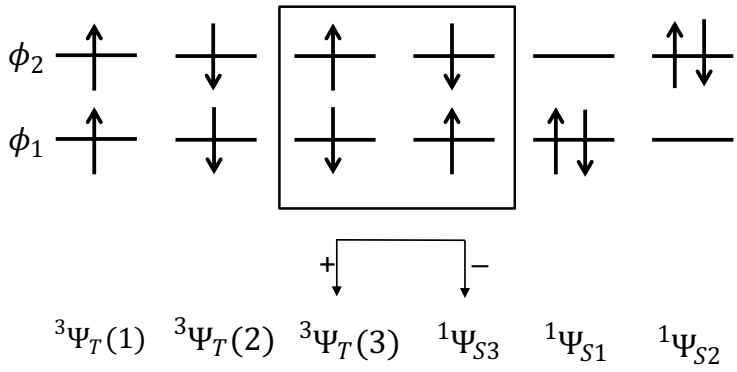

Figure 3.1. The six different Slater determinants represent the electronic configurations that are obtained when arranging two electrons in molecular orbitals $\phi_1$and ϕ_2. The bottom row indicates how the configuration translates to the three possible states: *i.e.* singlet state ($^1\psi_{S1}$), doubly-excited singlet state ($^1\psi_{S2}$), singly-excited singlet ($^1\psi_{S3}$) state and the three components of the triplet state ($m_S = +1\ ^3\psi_T(1)$, $-1\ ^3\psi_T(2)$ and $0\ ^3\psi_T(3)$).

(FM) and J_{AB}>0. The correct estimation of the energy of the two lowest states is thus crucial for the computation of J_{AB}, which for molecular systems is relatively small (1 to 10^3 cm^{-1} in absolute value), and very sensitive to errors in the evaluation of the energy. We need then to select the correct quantum chemical method to accurately describe both states. Usually, this implies the use of CASSCF[6,7] or CASPT2[8,9] calculations which are complex and, depending on the size of the system, computationally unattainable. However, it has been shown that calculations based on the Density Functional Theory (DFT) approach[10,11], with a wise choice of the functional, provide accurate results when compared with the experimental data, being a faster and cheaper useful alternative to CASSCF calculations.

The DFT method is monodeterminantal and, hence, it cannot describe correctly the open-shell singlet state, since it requires at least two determinants (see Figure 3.1 for schematic representation). Thanks to the Broken-Symmetry approach (BS)[12,13], the problem has been tackled, allowing the evaluation of J_{AB}. The energy of the open-shell BS singlet state ($E_{S,BS}$) is calculated to lay between the singlet and triplet states, and can be regarded as a linear combination of these two states, which leads, using the HDVV Hamiltonian given in Eq. 3.1, to:

$$J_{AB} = \frac{(E_{S,BS} - E_T)}{1 + S_{ab}^2} \qquad \text{Eq. 3.5.}$$

Document signat digitalment per: CRISTINA RONCERO BARRERO

where S_{ab} is the overlap between the a and b localized magnetic orbitals. Usually, there are two possible extreme situations: i) strongly localized or orthogonal orbitals lead to S_{ab}=0, and ii) the delocalized limit results in S_{ab}=1. In the DFT-BS calculations presented in this PhD thesis, the localized limit has been employed, since visual inspection of the SOMOs shows that S_{ab}~0. Accordingly, the magnetic coupling between any two spin-carrying centres has been evaluated as:

$$J_{AB} = E_{S,BS} - E_T \qquad \text{Eq. 3.6.}$$

Although the presented derivation that concludes in Eq. 4 and Eq.6 has been thought for pairs of radicals, HDVV Hamiltonian approach has also been shown to lead to correct estimations of J_{AB} when using both clusters with more than two radicals and periodic calculations.[14] In these cases, within the framework of the Ising Hamiltonian, a system of equations has to be settled for the evaluation of all the J_{AB} under consideration.

Referring to the bisDTA systems studied in this PhD dissertation, Chapter 4 will illustrate the procedure to evaluate J_{AB} conducted using a periodic approach to obtain different magnetic solutions needed to assess each J_{AB} individual magnetic coupling. Next, Chapter 5 will present a full screening of all possible J_{AB} using a dimer cluster evaluation. The resulting set of J_{AB} values obtained in both chapters will be then fully compared. In both cases, energies are computed with B3LYP[15,16] hybrid functional in the spin unrestricted formalism, since this functional has been extensibly used in the study of this kind of materials, providing reliable results in closely related systems.[2,17,18,1920] Technicalities regarding the computational details of J_{AB} evaluation will be briefly outlined in Section 3.3.

Once all the radical···radical J_{AB} couplings have been detected and calculated, the magnetic topology can be constructed, which will show how the interactions interconnect and propagate within the material. At this point, let us remark that magnetism is a cooperative property resulting from the

Document signat digitalment per: CRISTINA RONCERO BARRERO

interconnection of the spin centres in the crystal through the calculated magnetic interactions (J_{AB}). Therefore, in molecule-based crystals, magnetic topologies can have dimensionalities ranging from 0D (isolated spin carrying centres) to complex 3D networks of interconnected radicals along the three spatial directions.

3.1.3 Construction of the minimal magnetic model and Diagonalization of HDVV Hamiltonian

From the infinite magnetic topology, a finite cluster of radicals including all the relevant J_{AB}'s have to be extracted in order to compute the matrix representation of the Heisenberg Hamiltonian, obtain the energy spectra and, then, the macroscopic magnetic properties. This finite model, the so-called *minimal magnetic model*, is limited in size to a maximum of 18 radicals due to the scalability and computational cost of the diagonalization, since the dimensionality of the matrix representation increases as:

$$K(n) = \frac{n!}{\left(\frac{n}{2}\right)!\left(\frac{n}{2}\right)!} \qquad \text{Eq. 3.7.}$$

where n is the number of open-shell centres. The selected minimal magnetic model has to incorporate, as mentioned, all the non-negligible J_{AB} in a ratio as close as possible to that in the magnetic topology. The resultant properties are dependent on the model. Therefore, a non-representative model could lead to wrong results despite the correct calculation of the J_{AB} interactions. For the study of the four title bisDTA S/Se systems, different magnetic models have been explored and analysed in order to ensure that no problems arise from the model cluster selection. A detailed discussion will be provided in Chapter 5.

The Heisenberg Hamiltonian matrix is then constructed with the minimal magnetic model as:

$$\hat{H} = -2\sum_{A>B} J_{AB}(\hat{\boldsymbol{S}}_{\boldsymbol{A}}\hat{\boldsymbol{S}}_{\boldsymbol{B}} + \frac{1}{4}\hat{I}_{AB}) \qquad \text{Eq. 3.8.}$$

Document signat digitalment per: CRISTINA RONCERO BARRERO

where $\hat{I}_{AB}$ is the identity operator, $\hat{S}_A$ and $\hat{S}_B$ are the spin operators acting in the spin centres A and B, and J_{AB} the previously computed exchange coupling between A and B radicals. The diagonalization of the Hamiltonian in the minimal magnetic model space results in the energy spectra with which, using Statistical Mechanics, the macroscopic magnetic susceptibility, magnetization or heat capacity can be computed.

3.1.4 Derivation of the macroscopic magnetic properties

Finally, the last step is the computation of the macroscopic magnetic properties of interest. In the case of the bisDTA compounds, we will focus on the magnetic susceptibility (χ) and the critical temperature (T_c). The Statistical Mechanics equation for the macroscopic χ as a function of temperature (T) in absence of an external magnetic field (H = 0) is:

$$\chi(T) = \frac{N_A g^2 \mu_B^2}{3 k_B T} \mu_0 \left[\frac{\sum_n S_n(S_n+1)(2S_n+1) e^{-\left[\frac{E_n - E_0}{k_B T}\right]}}{\sum_n (2S_n+1) e^{-\left[\frac{E_n - E_0}{k_B T}\right]}} \right] \qquad \text{Eq. 3.9.}$$

where g is the gyromagnetic constant and μ_B the Bohr magneton, E_n and S_n are the energy and spin of the n microstate, N_A is the Avogadro constant and k_B the Boltzmann constant. Usually, T_c is obtained by analysing the maximum in the heat capacity as a function of temperature ($C_p(T)$) curve, which indicates a second order phase transition. The Statistical Mechanics expression for C_p is:

$$C_p(T) = \frac{N_A}{k_B T^2} \left[\frac{\sum_n (2S_n(S_n+1)\,(E_n - E_0)^2 \mathrm{e}^{\left[-\frac{(E_n - E_0)}{k_B T}\right]}}{\sum_n (2S_n+1) \mathrm{e}^{\left[-\frac{(E_n - E_0)}{k_B T}\right]}} - \frac{\left(\sum_n (2S_n+1)(E_n - E_0) \mathrm{e}^{\left[-\frac{(E_n - E_0)}{k_B T}\right]}\right)^2}{\left(\sum_n (2S_n+1) \mathrm{e}^{\left[-\frac{(E_n - E_0)}{k_B T}\right]}\right)^2} \right] \qquad \text{Eq. 3.10.}$$

However, it was observed that this transition, associated with energy changes rather than spin, was not always compatible with the T_c expected from a magnetic order/disorder physical transition.[21] Thus, a definition of a magnetic critical temperature was presented based in monitoring the spin moment instead

Document signat digitalment per: CRISTINA RONCERO BARRERO

of the energy, *i.e* monitoring the magnetic capacity (C_s). $C_s(T)$ accounts for the variation of the mean value of the spin multiplicity of the system as a function of temperature, and can also be related to the maximum in $\partial[\chi T(T)]/\partial T$ that can be obtained directly from experimental data. Differences between both $C_p(T)$ and $C_s(T)$ reveal the importance of long-range interactions operating in the system. Since $C_p(T)$ does not capture the long-range magnetic order, systems with negligible long-range interactions will exhibit $T_c(C_s) \sim T_c(C_p)$. The mathematical expressions employed for C_p and C_s have been derived using the Valence Bond theory, specifically the spin exchange density matrix elements (P_{ij})[22]. In parallel, the analysis of the different P_{ij} elements of the spin exchange density matrix will provide information about the alignment among all the spin units and its dependence upon temperature. Therefore, short- and long-range spin correlations will be obtained using the computed energy spectra by constructing and diagonalising the Heisenberg Hamiltonian in the Valence Bond (VB) framework.

3.1.4.1 C_p and C_S in the Valence Bond framework

The spin-exchange operator $\hat{P}_{ij}$ is a permutation operator which means that, when applied to two-electron spin functions $\Theta(1,2)$, it exchanges their spin coordinates. In fact, $\hat{P}_{ij}$ is an operator that has the same effect than the spin operator product ($\hat{S}_i \cdot \hat{S}_j$) of the Heisenberg Hamiltonian (Eq. 3.1). Therefore, it can be shown that ($\hat{S}_i \cdot \hat{S}_j$) and $\hat{P}_{ij}$ are related according to:

$$\left[\hat{S}_i\hat{S}_j\right]\Theta(1,2) = -\left(\frac{1}{2}\hat{P}_{ij} - \frac{1}{4}\hat{I}\right)\Theta(1,2) \qquad \text{Eq. 3.11.}$$

i.e.

$$\hat{P}_{ij} = \langle -\left(2\left[\hat{S}_i\hat{S}_j\right] + \tfrac{1}{2}\hat{I}\right)\rangle, \qquad \text{Eq. 3.12.}$$

where $\hat{I}$ is the identity operator. The reader is addressed to the reference paper [21] for a more detailed derivation of $\hat{P}_{ij}$. The expected values of $\hat{P}_{ij}$ operator, are the spin-exchange density matrix (P_{ij}) elements, which give a quantitative measure of the magnetic-bond order and are related to the total S spin by:

Document signat digitalment per: CRISTINA RONCERO BARRERO

$$S(S+1) = -\frac{N(N-4)}{4} - \sum_{i<j} P_{ij}, \qquad \text{Eq. 3.13.}$$

where N represents the number of unpaired electrons in the system. For instance, in a N=2 system the expected values for P_{ij} will be +1, -1 or -0.5 if the spins are either arranged FM (see Figure 3.2a), AFM (Figure 3.2b) or uncoupled (Figure 3.2c), respectively. Therefore, in this VB perspective, P_{ij} illustrates the magnetic bond-ordering between spin centres.

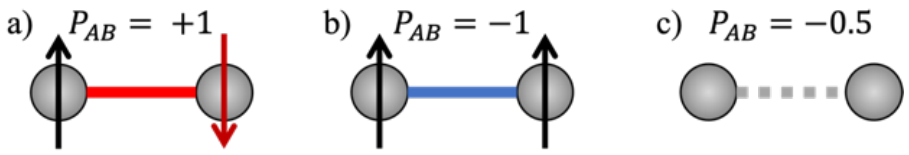

Figure 3.2. Possible spin alignments of the magnetic centres A and B in a two-electron system, and their expected P_{ij} value for (a) FM ordering, (b) AFM ordering and (c) magnetically uncoupled.

Within the P_{ij} VB framework, the general spin-exchange Hamiltonian (Eq. 3.8) for a S_A=S_B=1/2 system can be re-written as:

$$\hat{H} = -\sum_{AB} J_{AB}\left(2\hat{S}_A\hat{S}_B + \frac{1}{2}\hat{I}_{AB}\right) = \sum_{AB} J_{AB}\,\hat{P}_{AB}\,, \qquad \text{Eq. 3.14.}$$

and the Statistical Mechanics expression for the C_p(T) and C_s(T) derived from the Canonical partition function are expressed as:

$$C_p(T) = \frac{\partial\langle E\rangle_T}{\partial T} = \frac{N_A}{k_B T}\left\{\sum_n\left[\left(\sum_{A<B} J_{AB}\cdot P^n_{AB}(J)\right) f^n_B(T)\left[\sum_m (E_m - E_n) f^m_B(T)\right]\right]\right\} \qquad \text{Eq. 3.15.}$$

$$C_s(T) = \frac{\partial\langle S^2\rangle_T}{\partial T} = \frac{N_A}{k_B T}\left\{\sum_n\left[\left(\sum_{A<B} P^n_{AB}(J) + P^n_{AB}(0)\right) f^n_B(T)\left[\sum_m (E_m - E_n) f^m_B(T)\right]\right]\right\} \qquad \text{Eq. 3.16.}$$

where $f^n_B(T)$ is the Boltzmann distribution function ($f^n_B(T) = \frac{2S_n+1}{Z} e^{-E_n/k_B T}$) and defines the population of each microstate (n) in the canonical ensemble. $P^n_{AB}(0)$ and $P^n_{AB}(J)$ represent the value of P_{AB} at the two limiting cases in which, $J_{AB} \to 0$ and at a finite J_{AB} value, respectively. Thus, $P^n_{AB}(0)$ belongs to long-range spin couplings which have no energetic effects in the Heisenberg Hamiltonian.

Document signat digitalment per: CRISTINA RONCERO BARRERO

Analysing Eq. 3.15 and 3.16, it can be observed that the C_p(T) heat capacity involves changes in the energy of the system and depends on those radicals connected by significant J_{AB}, i.e. on the short-range spin coupling of the magnetic interactions. On the other hand, magnetic capacity C_S(T) depends on the changes in the spin moment and, hence, on the spin-alignment between all the spin centres, including those not connected by a significant J_{AB}.

3.2 Electric conductivity

Similar to magnetism, electric conductivity will be computed following a bottom-up working strategy that starts from the ab-initio calculation of the microscopic parameters and ends with the estimation of the macroscopic property. However, unlike the previous section, this working strategy is not unbiased, since it will be shown that models and assumptions are employed to tackle the simulation of electric conductivity. In this section, a top-down scheme will be followed in order to introduce the calculation of the electric conductivity σ and the model used. Yet the actual calculation of the conductivity will be implemented according to a bottom-up approach.

Conductivity (σ) is a rank 2 tensor defined in general, for any material, as the resultant charge flow of applying an external electric field. The general expression for σ depends on the density of charge carriers (ρ_c), the charge that they transport (q) and their mobility (μ) (see Eq. 17).[23]

$$\bar{\bar{\sigma}} = \rho_c q \bar{\bar{\mu}} \qquad \text{Eq. 3.17.}$$

Specific features of the materials, such as main transport mechanism or doping, are introduced in the definition of μ and ρ_c. The mobility tensor ($\bar{\bar{\mu}}$) defines the ability of a charged particle to move with an average velocity ($\langle \vec{v} \rangle$) in response to an applied external electric field ($\vec{E}$).

$$\mu_{ij} = \frac{\langle v \rangle_i}{E_j} \qquad \text{Eq. 3.18.}$$

Document signat digitalment per: CRISTINA RONCERO BARRERO

There are different experimental (*e.g.* Time-of-Flight, Field-Effect Transistor Configuration, TF-SCLC method …)[24] and computational techniques to measure μ.[23,25] Regarding computational modelling, methods are grouped in three categories depending on the predominant transport mechanism due to the degree of localization of the charge carriers in the material (see Figure 3.3). There are two opposite limiting regimes, namely, the itinerant band transport and the localized hopping, and also an intermediate regime between both limiting cases.

Band transport treats charge carriers as fully delocalized in the band edges of either valence or conduction bands. It is based on Bloch's theorem, which establishes that electron orbitals in a periodic potential are a superposition of plane waves modified by a set of periodic functions.[26,27] On the other hand, in the hopping limit, charge carriers are localized on a site in the system and describe the charge diffusion as the sum of consecutive jumps of charge between those sites (donor and acceptor). Broadly speaking, the band model is typically used in the description of metals and highly pure inorganic and organic crystals with large μ mobilities, while disordered materials or weakly coupled organic crystals are often studied from a localized hopping perspective or intermediate regime (see Figure 3.3). Experimentally, the measurement of μ when cooling/heating can hint at the predominant charge transport regime in the material. In fact, a decrease of μ when heating usually points out to a band transport mechanism and the opposite will be assigned to a hopping transport, which will be discussed in the following Section 3.2.1.

3.2.1 Charge Carrier Mobility: Hopping regime

In the hopping regime, charge transport is defined as discrete jumps of charge between the donor (D) and acceptor (A) sites in terms of charge transfer rates (k_{DA}). The definition of donor and acceptor sites depends on the degree of localization of the system and can range from just a molecule to a group of molecules.

Document signat digitalment per: CRISTINA RONCERO BARRERO

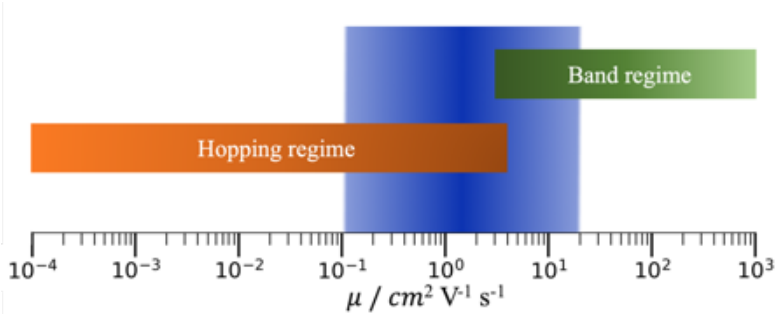

Figure 3.3. Representation of the ranges of validity of hopping (orange) and band (green) models according to the magnitude of the charge mobility (μ). The blue box illustrates the range of charge mobilities. Data has been obtained from ref. 28.

In this regime, the average drift velocity ($\langle\vec{v}\rangle$ in Eq. 3.18) can be computed as a sum of all the hopping rates between sites times the distance between them ($k_{DA}\vec{r}_{DA}$). The resultant expressions for the hopping mobility can be solved analytically in perfectly symmetric materials. Otherwise, in disordered systems or in those with intricate conduction paths, hopping mobilities have to be solved numerically with methods such as kinetic Monte Carlo[29], and the Master equation approach[30], among others.[23,] In the study of the four title bisDTA S/Se materials, μ mobilities will be computed in the hopping limiting regime using the master equation approach (see Eq. 3.19). Accordingly, μ can be calculated in terms of the p_A hopping probability for each single jump to occur, which will be computed as $p_A = \frac{k_{DA}}{\sum k_{DA}}$,[31] the $\vec{r}_{DA}$ distance between donor and acceptor sites and the E electric field.

$$\mu = \frac{1}{E}\sum_{A>D} p_A k_{DA}\vec{r}_{DA}\frac{\vec{E}}{E} \quad , \qquad \text{Eq.3. 19.}$$

Conductivity can be realized through electron transport (n-type conductor), hole transport (p-type conductor), or can be ambipolar if both mechanisms are equally possible. Therefore, the CT charge transfer reaction depends on the mechanism considered. It involves the oxidized form of the monomer when hole conduction is considered, or the reduced form for electrons conduction (see R.1 and R.2, respectively, in Figure 3.4). Accordingly, for hole conduction, the acceptor has a lack of electrons (A^+) while the donor is a neutral

Document signat digitalment per: CRISTINA RONCERO BARRERO

species (D), and after CT the acceptor becomes neutral (A) and the donor a cation (D^+). Contrarily, for electron conduction, the acceptor is neutral (A) and the donor has extra electrons (D^-) that will transfer to the acceptor, which will then become an anion (A^-). In this work, both possibilities have been contemplated and, although in some figures hole transfer will be used to illustrate the methodology, the treatment here presented will be equivalent for the study of electron transfer.

R.1	R.2
$A^+ + e^- \rightarrow A$	$A + e^- \rightarrow A^-$
$D \rightarrow D^+ + e^-$	$D^- \rightarrow D + e^-$
$A^+ + D \rightarrow A + D^+$	$A + D^- \rightarrow A^- + D$

Figure 3.4. Mechanism of charge transfer (CT) according to either hole conduction (R.1, $A^+ + D \rightarrow A + D^+$) or electron conduction (R.2, $A + D^- \rightarrow A^- + D$). Note that acceptor (donor) is always involved in the reduction (oxidation) reaction.

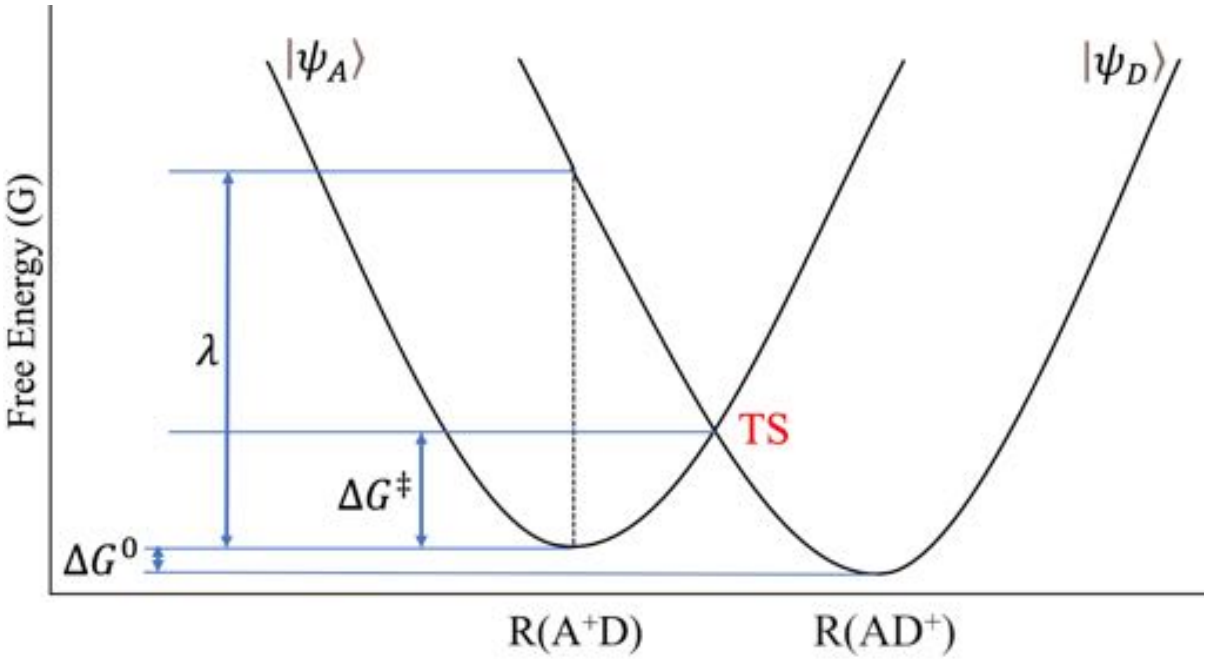

Figure 3.5. Charge transfer diabatic profile where R(A^+D) and R(AD^+) denote collective variables of all the nuclear coordinates before and after the charge transfer. Initial (A^+D) and final (AD^+) states are described with two curves that cross at the TS transition state. Note that hole charge transfer (R.1) has been here used to illustrate the concept, which will be equivalent in the case of electron transfer (R.2).

Document signat digitalment per: CRISTINA RONCERO BARRERO

Hopping rate theories define charge transport (CT) as a process that can only occur if the system overcomes an energy barrier at the transition state (TS), in which the geometry configurations of donor and acceptor are energetically degenerated. Assuming a harmonic response, for the hole transfer (see R.1 in Figure 3.4), the potential energy surface (PES) of the process along a reaction coordinate can be described in terms of two non-coupled diabatic PES, namely initial (A^+D) and final (AD^+) states (see Figure 3.5). The diabatic view of the CT process will be useful to define three important energetic quantities for the calculation of k_{DA} (see Eq 3.20): i) the reorganization energy (λ) which accounts for the effects of polarization due to the CT, ii) the driving force (ΔG^0) between the minima of the initial "A^+D" and final "AD^+" states, and iii) the diabatic activation energy ($\Delta G^{\ddagger}$) that the system needs to overcome.

In organic semiconductors, k_{DA} has been typically studied using the widely known Marcus equation[32,33]. Marcus theory describes the charge transfer in the adiabatic limit of the semiclassical Landau-Zener theory, which is also called nonadiabatic when $\lambda >> H_{DA}$.[23] According to :

$$k_{DA} = \frac{2\pi}{\hbar}\frac{1}{\sqrt{4\pi\lambda k_B T}}\langle|H_{DA}|^2\rangle_{TS} e^{-\frac{\Delta G^{\ddagger}}{k_B T}}, \qquad \text{Eq.3.20.}$$

where k_B is the Boltzmann's constant, $\hbar$ is the reduced Plank constant ($\hbar = h/2\pi$) and H_{DA}, the so-called electronic coupling, is a Hamiltonian transition matrix element between the diabatic electronic states of D donor and A acceptor at the TS. Note that $\Delta G^{\ddagger}$, known as the diabatic activation energy, is related to the ΔG^0 driving force and the λ reorganization energy (see Eq. 21) as:

$$\Delta G^{\ddagger} = \frac{(\lambda + \Delta G^0)^2}{4\lambda} \qquad \text{Eq. 3.21.}$$

Hence, in this hopping limit, k_{DA} can be fully determined by the λ reorganization energy, the ΔG^0 driving force and the H_{DA} electronic coupling.

Document signat digitalment per: CRISTINA RONCERO BARRERO

The CT process in the hopping approach is split into two steps: i) a fast CT process at the TS frozen geometry coordinates (H_{DA} electronic coupling) and ii) a slower relaxation of the geometry that has to adapt to the new charge distribution, evaluated by the λ reorganization energy. At this point, it is necessary to remind that bisDTA-derived compounds are one-component molecular crystals in which the charge is localized in the molecular building blocks. Thus, there is just one type of spin-carrying moieties. It follows that the same A and B paramagnetic sites that served as spin centres (J_{AB}) will be the ones involved in the charge transfer process. As will be discussed next, the fact that there is one radical acting as D donor and A acceptor sites will simplify significantly the evaluation of both H_{DA} electronic couplings and λ reorganization energy.

3.2.1.1 Electronic coupling (H_{DA})

The Electronic coupling (H_{DA}), as has been briefly mentioned before, is defined as an off-diagonal Hamiltonian matrix element between the initial ($|\psi_A\rangle$) and the final ($|\psi_D\rangle$) diabatic states of the CT at the nuclear transition state (see Figure 3.5 and Eq 3.22).

$$H_{DA} = \langle \psi_A | \hat{H} | \psi_D \rangle_{TS} \qquad \text{Eq. 3.22.}$$

The determination of the diabatic wave functions, and hence of H_{DA}, is one of the most critical steps in the evaluation of k_{DA}. H_{DA} values are strongly dependent on the orbitals of both wavefunctions and on the geometries of the D donor and A acceptor radicals. In the literature, several approaches that tackle the diabatization of the wave functions can be found, especially, for amorphous systems where electronic coupling has to be computed for many configurations.[23] However, for two-state systems, there is an exact relationship between the energies of adiabatic (E_1 and E_2) and diabatic (E_A and E_D) states.

$$E_{1,2} = \frac{1}{2}(E_A + E_D \pm \sqrt{(E_A - E_D)^2 + 4|H_{DA}|^2} \qquad \text{Eq. 3.23.}$$

The solution in Eq. 23 can be easily encountered by solving the two states diabatic Hamiltonian. However, with this solution, in order to compute H_{DA}, the

Document signat digitalment per: CRISTINA RONCERO BARRERO

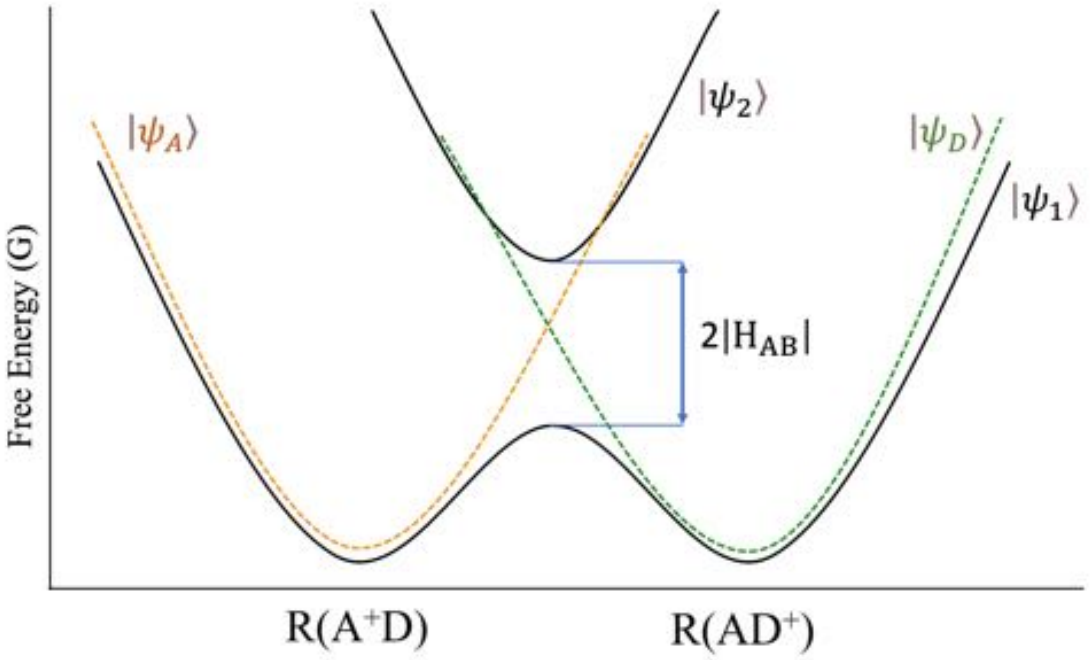

Figure 3.6. Representation of a two-states charge transfer adiabatic potential energy surface ($|\psi_1\rangle$ and $|\psi_2\rangle$, in solid black lines), compared to the diabatic picture ($|\psi_A\rangle$, orange and $|\psi_D\rangle$ in green dashed lines).

evaluation of the E_A, E_D diabatic state energies will still be needed. A further simplification is introduced when the system under study is highly symmetric. When both diabatic states are equivalent, and hence $E_A = E_D$, the excitation energy between both adiabatic solutions ($|\psi_1\rangle$ ground state and $|\psi_2\rangle$ first excited state, see Figure 3.6) is equal to twice H_{DA}.

$$\Delta E_{12} = E_2 - E_1 = 2|H_{AB}| \qquad \text{Eq. 3.24.}$$

In this case, the key for an accurate estimation of H_{DA} resides in the evaluation of the energy of the adiabatic states at the transition state geometry. The study of H_{DA} in the four bisDTA S/Se systems has been performed using a two monomer cluster since each monomer is believed to act as a site for the CT either as D donor or A acceptor. Note that a distinct dimer cluster for each non-equivalent possible k_{DA} rate constant has to be selected for the correct evaluation of the global conductivity of the crystal. Adiabatic state energies (E_1 and E_2) for each dimer cluster have been computed by means of state-average CASSCF

Document signat digitalment per: CRISTINA RONCERO BARRERO

calculations. Further details about H_{DA} computation will be outlined in Section 3.3.

3.2.1.2 Reorganization Energy (λ)

The reorganization energy (λ) is the term that accounts for all the polarization and geometry relaxation involved in the CT process. It evaluates the electrostatic response of the surroundings to the CT between two sites and the polarization of the sites themselves. Clearly, the total reorganization energy can be divided into two contributions (Eq. 3.25): the inner-sphere (λ_{in}) and the outer-sphere (λ_{ex}), which account for the short- and long-range polarizations, respectively.

$$\lambda = \lambda_{in} + \lambda_{ex} \qquad \text{Eq.3.25.}$$

Usually, in organic materials, changes in the equilibrium geometry of donor and acceptor monomers are denoted as inner contributions and the polarization / relaxation effects of the rest of the system as outer-sphere energy. It is important to remark that this separation has been shown to be valid in organic molecular materials, due to the weak van der Waals interactions that act as cohesive forces. The λ_{in} component is computed according to a four-point scheme, using two models constructed with the isolated acceptor and the isolated donor moieties to calculate the reorganization energies involved in the reduction λ_R and oxidation λ_O processes, respectively. For hole charge transfer (see R.1 in Figure 3.4), the reduction (λ_R) of an A^+ acceptor (oxidant agent) and the oxidation (λ_O) of a D donor (reducer agent) take place. Therefore, it will be necessary to evaluate the energy of the A^+ cation and A neutral geometries of the acceptor on the neutral PES to obtain λ_R , and the energy of the D neutral and D^+ cation geometries of the donor on the charged PES to evaluate λ_O (see Figure 3.7). The contributions to the free energy of both moieties are then computed evaluating the energy difference due to the geometry relaxation after the fastest charge transfer process.

Document signat digitalment per: CRISTINA RONCERO BARRERO

HOLE TRANSPORT

reduction process (R) oxidation process (O)

$A^+ + 1e^- \rightarrow A$ $D \rightarrow D^+ + 1e^-$

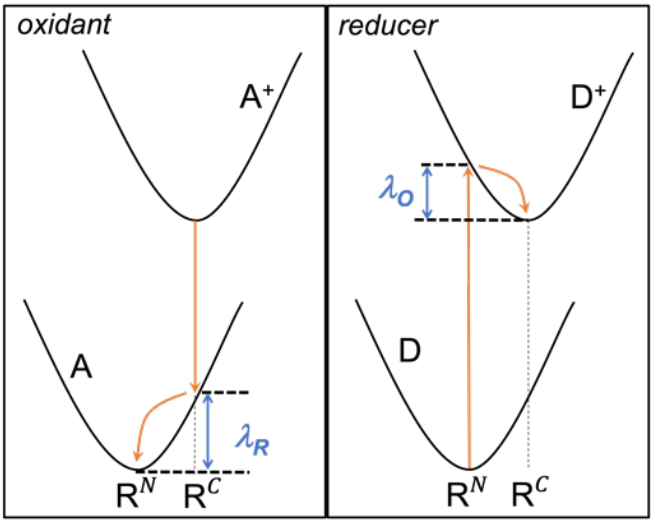

Figure 3.7. Four-point scheme to calculate the reorganization energy λ for hole transport mechanism as illustrated in the potential energy surfaces (PES) of the monomer cluster approach (λ, see Eq.3.26 and R.1 in Figure 3.4). Note that λ(hole) is the sum of the reorganization energies involved in the reduction (λ_R) of an A^+ acceptor (oxidant agent) and the oxidation (λ_O) of a D donor (reducer agent). Note that, although for electron transport the mechanism will involve the reduction of an A acceptor and the oxidation of a D^- donor (see R.2 in Figure 3.4), the above four-point scheme still applies.

$$\lambda_{in} = \lambda_R + \lambda_O$$
$$\lambda_R = E_N(R^C) - E_N(R^N)$$
$$\lambda_O = E_c(R^N) - E_c(R^C)$$
$$\lambda_{in} = [E_c(R^N) + E_N(R^C)] - [E_c(R^C) + E_N(R^N)] \quad \text{Eq.3.26.}$$

External reorganization energy was originally derived for liquid mixtures and computed with a mean-field approach. In organic crystals, it has been observed that the contribution of the environment is negligible in front of the inner reorganization. Yet, in TTF-derivatives, it has been observed that molecular and electronic polarization of the environment has a non-innocent impact in the reorganization energy, leading to a non-negligible λ_{ex} contribution. [34,35] At the light of these studies, we can expect λ_{ex} to also contribute in bisDTA derivatives. However significant, since the nature of the environment in all four crystals is identical, we can assume that λ_{ex} will be a constant similar

Document signat digitalment per: CRISTINA RONCERO BARRERO

contribution that will affect evenly the overall λ of these four isostructural bisDTA compounds whose conductivity is to be rationalised. Therefore, we will take advantage of the isostructural environment of all four compounds and, thus, solely aim at evaluating how the geometry of the charge carriers (λ_{in}) is affected during the charge migration. The specific computational details regarding the evaluation of λ_{in} will be briefly explained in the following Section 3.3.

3.2.1.3 Driving force

The driving force is the free energy difference between the two minima of the diabatic energy surfaces (see Figure 3.5). Under a homogeneous external electric field the ΔG^0 driving force between monomers at a $\vec{r}_{DA}$ distance is computed as:

$$\Delta G^0 = G_i(R_{A^+D}) - G_f(R_{AD^+}) + q\vec{E}\vec{r}_{DA} \qquad \text{Eq. 3.27.}$$

where G_i and G_f are the free energies of the A^+D initial and AD^+ final states, and R_{A^+D} and R_{AD^+} the equilibrium geometries for both states. In one-component crystals, both donor and acceptor molecules are equivalent. In addition, if both can be interchangeable through a symmetry operator, both minima of the PES are degenerate and the $G_i(R_{A^+D}) - G_f(R_{AD^+})$ energy difference becomes 0. In these cases, just the electric field dependent term remains ($q\vec{E}\vec{r}_{DA}$), which can be neglected in the low field limit. [36] Notice that then, Marcus equation (Eq. 3.20) will fully depend on the λ reorganization energy and H_{DA} electronic coupling parameters.

$$k_{DA} = \frac{2\pi}{\hbar}\frac{1}{\sqrt{4\pi\lambda k_B T}}\langle|H_{DA}|^2\rangle_{TS} e^{-\lambda/4k_B T} \qquad \text{Eq. 3.28.}$$

3.2.2 Charge Carrier Density

The density of mobile charge carriers in a solid, in absence of optical excitations, can be separated into two contributions: [23,26,27]

$$\rho_c = \rho_{in} + \rho_{ex} \qquad \text{Eq. 3.29.}$$

Document signat digitalment per: CRISTINA RONCERO BARRERO

The intrinsic density (ρ_{in}) accounts for the creation of holes and electrons due to thermal excitations in the electronic band structure of the ideal material, *i.e.,* without defects. The extrinsic density (ρ_{ex}) contribution adds the carrier density that arises from all the possible deviations from this ideal structure of the material. Therefore, the latter includes all the effects originated by point defects due to vacancies or to interstitial molecules (*e.g.,* solvent molecules) and doping with molecules or atoms.

Computationally, ρ_{in} for hole and electron conduction (ρ_{in}^{-} and ρ_{in}^{+}, respectively) can be obtained using the electronic density of states (DOS) around the Fermi energy (ε_F).

$$\rho_{in}^{-} = \int_{\varepsilon_F}^{\infty} d\varepsilon\, \rho(\varepsilon) f(\varepsilon;T)$$
$$\rho_{in}^{+} = \int_{-\infty}^{\varepsilon_F} d\varepsilon\, \rho(\varepsilon)\,[1 - f(\varepsilon;T)] \qquad \text{Eq. 3.30.}$$

where $f(\varepsilon;T)$ is the Fermi-Dirac function that defines the distribution of holes and electrons at a certain T.

$$f(\varepsilon;T) = \frac{1}{e^{(\varepsilon-\varepsilon_F)/k_BT} + 1} \qquad \text{Eq. 3.31.}$$

However well understood, the addition of extrinsic contributions in the model is not straightforward. The explicit incorporation of dopants or defects in the periodic electronic structure description can be avoided by simply adjusting the Fermi level position depending on the contribution. It thus follows that higher or lower hole (electron) charge carrier density results from shifting the Fermi energy (as schematically illustrated in Figure 3.8).

In an intrinsic pure semiconductor, the concentration of electrons (or holes) comes from the excitation of electrons from the valence to the conduction bands. This means that in the simplest case scenario, assuming a pure material without defects that could not modify the concentration of holes nor electrons, the quantity of each one is equal. Finally, using the quadratic integration of the

Document signat digitalment per: CRISTINA RONCERO BARRERO

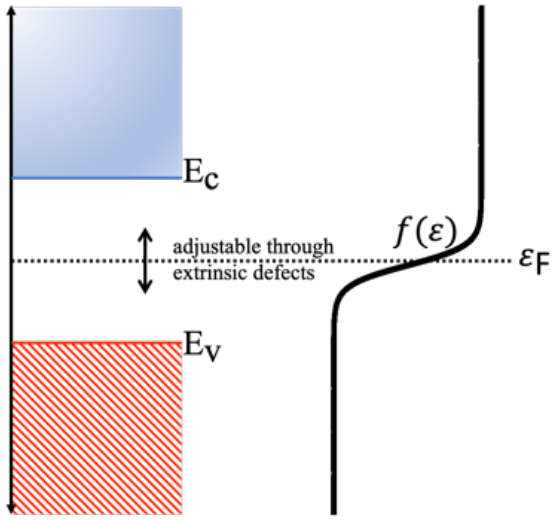

Figure 3.8. Representation of the energy distribution of the conduction (in blue) and valence (in red) bands. The Fermi energy (ε_F , black dashed line) has been taken to lie between both bands, as for an intrinsic semiconductor. On the right, the Fermi-Dirac function $f(\varepsilon;T)$ (see Eq. 31) for a specific T temperature has been illustrated.

DOS[26,27] (see Eq. 3.30) the total ρ_c could be computed with the E_g band gap of the material as:

$$\rho_c = 2\left(\frac{k_B T}{2\pi\hbar^2}\right)^{3/2}(m_e m_h)^{3/4}\, e^{-E_g/2k_B T} \qquad \text{Eq. 3.32.}$$

where m_e and m_h are the electron and hole mass, respectively.

3.3 Computational details.

As mentioned at the beginning of this chapter, the work here presented aims at testing two bottom-up strategies in the description of conductive and magnetic properties in a family of bisDTA S/Se materials. The common strategy can be foreseen as the combination of four steps (which are a generalized version of those illustrated in the FPBU working strategy for magnetism, see workflow in Figure 3.9):

i) *Crystal analysis* to select the clusters of radicals for the evaluation of the microscopic interactions. Note, that, since bisDTA paramagnetic centres act at the same time as spin centre (A, B radicals) and charge

Document signat digitalment per: CRISTINA RONCERO BARRERO

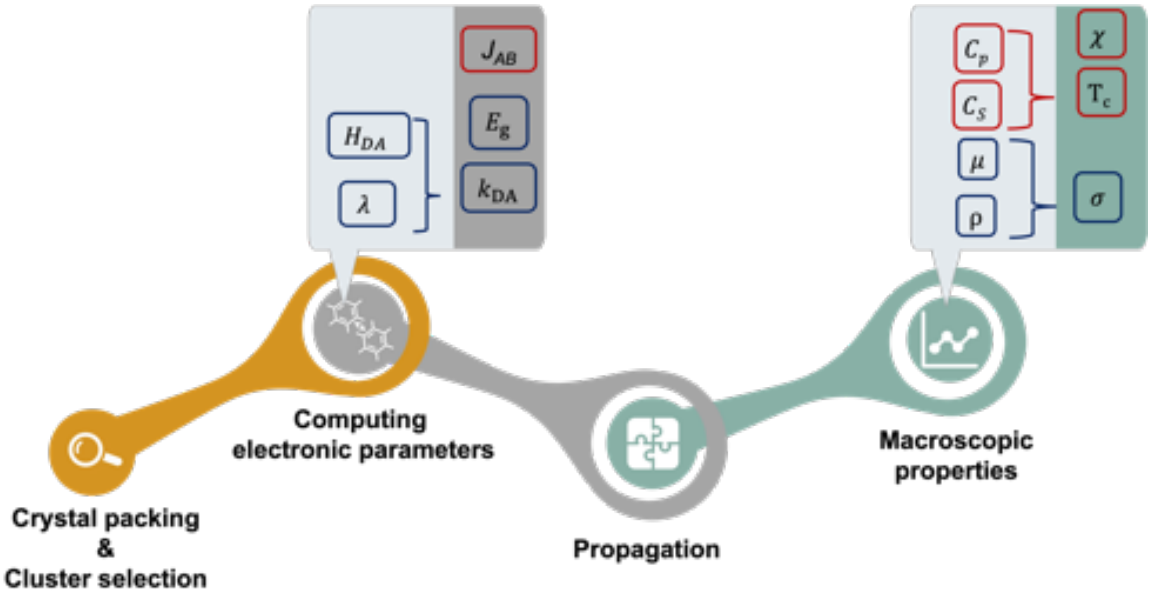

Figure 3.9 Workflow followed in the study of the magnetic and conductive properties. Intermediate parameters and final properties have been marked in red (for magnetism) and blue (for conductivity).

site (D donor and A acceptor), the cluster selection is required to evaluate both properties, magnetism (J_{AB}) and conductivity (H_{DA}).

i) *Computation of the microscopic* J_{AB} magnetic interaction and k_{DA} charge transport rate constant. For k_{DA}, a previous evaluation of the H_{DA} electronic coupling and λ reorganization energy is needed. Cluster evaluations of J_{AB} and H_{DA} are then performed using the previously selected pairs of radicals and λ with a single monomer cluster.

ii) Study of the *propagation* of the microscopic interactions within the crystal structure.

iii) Finally, computation of the *macroscopic properties* (χ, T_C and σ) of interest.

Among the afore-mentioned four steps, the cluster selection is common to the evaluation of H_{DA} and J_{AB}. Therefore, it will be outlined explicitly here, together with the computational details of the quantum chemistry calculations

Document signat digitalment per: CRISTINA RONCERO BARRERO

for the electronic parameters required in simulating magnetism (J_{AB}) and electric conductivity (H_{DA} and λ).

3.3.1 Crystal packing and Cluster selection

First, the crystal packing of all four materials is analysed in order to select all symmetry-unique pairs of A-B radicals that might present a non-negligible magnetic interaction (J_{AB}) or electronic coupling (H_{DA}, please keep in mind that D donor and A acceptor are the afore-mentioned A, B radicals). Within the family of bisDTA S/Se compounds (Fig 2.1), it has been found that contraction of $E_2 \cdots E_2$ distances correlates with an enhancement of conductivity and magnetism. Hence, in order to ensure the characterisation of all possible significant microscopic interactions, the criterion of selection of A-B pairs was the $E_2 \cdots E_2$ distance between closest contacts to be as large as a 7.0 Å threshold (note that Van der Waals $E_2 \cdots E_2$ distance is *ca.* 3.8 Å for (Se,Se) [37])

After an exhaustive assessment of which pairs of radicals have to be considered to evaluate the microscopic relevant interactions between bisDTA radicals, our analysis concluded that 13 pairs may contribute to the overall picture of both magnetic and electric properties for each one of our four target bisDTA compounds. Hereafter we describe the terminology used for all of them in order to name the selected radical···radical interactions. Taking a radical (identified as "central" in Figure 3.10) as reference, the *ab*-plane of the crystal shows five non-symmetry related π-stacks (namely, 1, 2, 3, 5 and 8 in Figure 3.10a, which are highlighted in blue). Notice that π-stacks 4, 6 and 7 are equivalent to 2, 3 and 5, respectively. Further analysis shows that the interactions between "central-2" and "central-5" radicals are also equivalent. From each π-stack, the 3 radicals closest to the central reference radical are referred as "#a", "#b" and "#c" where # stands for the number that identifies the stack (see Figure 3.10b). This geometrical analysis yields a total of 13 dimers for each system, i.e. the pairs of radicals evaluated are central vs. 1a-c, 2a-c, 3a-c and 8a-c, and central vs. top (or bottom) radical to assess the π-stack.

Document signat digitalment per: CRISTINA RONCERO BARRERO

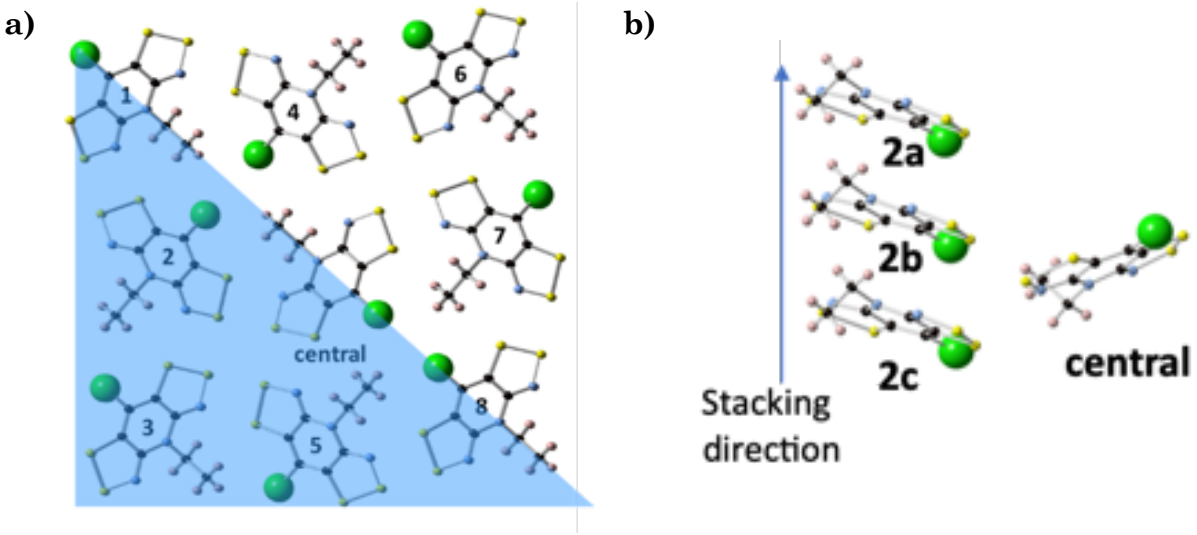

Figure 3.10 Selection of pairs of radicals that might be magnetically important. (a) View along the *ab*-plane (see region highlighted in blue for non-symmetry related π-stacks). (b) View along the π-stacking (*c*-axis) direction of the 3 dimers formed by the "central" reference radical and the radicals (*a*,*b*,*c*) in the π-stack numbered "2".

Reported studies on related materials[38,39] have shown that small variations in the arrangement of radicals within the crystal packing can make magnetic interactions along the π-stacking direction change from AFM to FM. In the present work, the dominant magnetic interactions of these four bisDTA materials (namely, (S,S), (S,Se), (Se,S) and (Se,Se) in Figure 2.1) and the effect of the S/Se substitution on their macroscopic magnetic response are analysed from a computational point of view. It will be shown that small structural changes might explain the differences among the four compounds at the electronic level, which in turn will clarify their magnetic properties at low and room temperatures. A complete analysis following the bottom up working strategy described in Section 3.1 has been carried out with the crystallographic data reported at 100 K[40]. Due to the lack of low temperature experimental data, optimised geometries are needed in order to describe the magnetic topology below the critical temperature and, thus, explain the temperature effects on the observed magnetism. Indeed, the fact that the systems are molecular multifunctional materials constituted by neutral radical molecules makes this family a challenging problem for quantum chemistry.

Document signat digitalment per: CRISTINA RONCERO BARRERO

Table 3.1. Cell parameters (in Å) for all 4 bisDTA compounds.

	(S,S)		(S,Se)		(Se,S)		(Se,Se)	
	a,b /Å	**c /Å**	**a,b /Å**	**c /Å**	**a,b /Å**	**c /Å**	**a,b /Å**	**c /Å**
295K[a]	15.886	4.1088	16.0334	4.109	16.0565	4.1599	16.2708	4.172
100K[a]	15.7927	4.031	15.9014	4.0161	16.0331	4.092	16.1801	4.1264
0K[b]	15.744	3.9907	15.835	3.9692	16.021	4.0572	16.134	4.1034

a. Data from ref.40
b. Values extrapolated from the 100 and 295K cell parameters

Geometry optimisations of all four bisDTA compounds were performed using the Quantum Espresso 5.4.0 code[41]. The cell parameters were extrapolated at 0 K from the data at 100 and 295 K reported in the literature[40] (cell parameters are listed in Table 3.1) and not allowed to relax along the optimisation. For the optimisation, the Broyden-Fletcher-Goldfarb-Shanno algorithm implemented in the Quantum Espresso code was used. Each optimisation was carried out with the PBE[42,43] exchange-correlation functional, supplemented with the Semiempirical Grimme's DFT-D2 correction[44]. A kinetic energy cut-off of 35 Ry and a Kinetic energy cut-off for charge density and potential of 280 Ry was set up for the plane wave basis set in all calculations. In all optimisations, the first Brillouin zone was sampled using a 2x2x2 Monkhorst–Pack grid of *k* points without offsets. Note that all optimisations were carried out in a supercell constructed doubling the unit cell along the stacking direction (*c*-axis) to allow for an antiferromagnetic coupling between the spins along the stack. Once optimised, the four bisDTA S/Se materials, where analysed according to the previously mentioned bottom-up working strategy and, results compared to those obtained from analysis of the CIF data at 100K.

3.3.2 Computing electronic parameters

3.3.2.1 J_{AB} magnetic coupling

Periodic calculations

In Chapter 4, the electronic structure of the family of bisDTA S/Se compounds is studied by periodic electronic band structure calculations using the

Document signat digitalment per: CRISTINA RONCERO BARRERO

spin unrestricted formalism of the B3LYP hybrid DFT functional[15,16] and the broken symmetry (BS) approach, as implemented in the CRYSTAL package.[45,46] Let us remark that the adequacy of BS-UB3LYP functional to describe the electronic structure and magnetic interactions has been confirmed by previous calculations on related systems.[38,55,17,18,2,19,20] The CRYSTAL computational code makes use of local basis sets of Gaussian-type orbitals (GTO) as used in standard quantum chemistry calculations. All electrons of N, C, and H lighter atoms are explicitly included in the calculations, whereas a nonrelativistic pseudopotential is used to describe the inner electrons of the S, Cl and Se atoms. Specifically, for the lighter atoms we used the basis sets reported by Gatti et al.[47], with contractions 3-1p1G for H and 6-31d1G for C and N. For the heavier atoms (S, Se and Cl) effective core pseudopotentials (ECP) have been used to describe the inner electrons. For Cl we used the "large core" ECP by Hay and Wadt,[48] for S a "large core" ECP by Durand and Barthelat[49] and for Se a "small core" ECP from the Stuttgard-Dresden[50] group. Gaussian type orbital (GTO) atomic basis sets have been used for each atom: for S we used the 31G* basis set reported by Ouazzani et. al.[51] , for Se we used the 6611-661d61G basis set reported by Heyd et al.[52] and for Cl a 31G basis set reported by Prencipe.[53] All these basis sets are available in the web page of the CRYSTAL program.[54]

The cut-off threshold parameters of CRYSTAL for Coulomb and exchange integral evaluations (ITOL1 to ITOL5) have been set to the 7, 7, 7, 7, and 14 strict values, respectively. The integration in reciprocal space has been carried out on a Monkhorst-Pack grid of 2x2x4 K points to cover the irreducible Brillouin zone. The numerical thresholds used to ensure the numerical convergence of the self-consistent-field procedure were set to 10^{-6} a.u. for the one-electron eigenvalues and 10^{-7} a.u. for the total energy. All four target compounds were experimentally characterised at 100K. Therefore, the X-Ray crystal data at 100K was used as the only input data.[40] Interestingly, (Se,Se) has been also characterised at 2K[55], and this X-Ray data has also been used as input to extract J_{AB} magnetic couplings. Several magnetic solutions have been calculated for each

Document signat digitalment per: CRISTINA RONCERO BARRERO

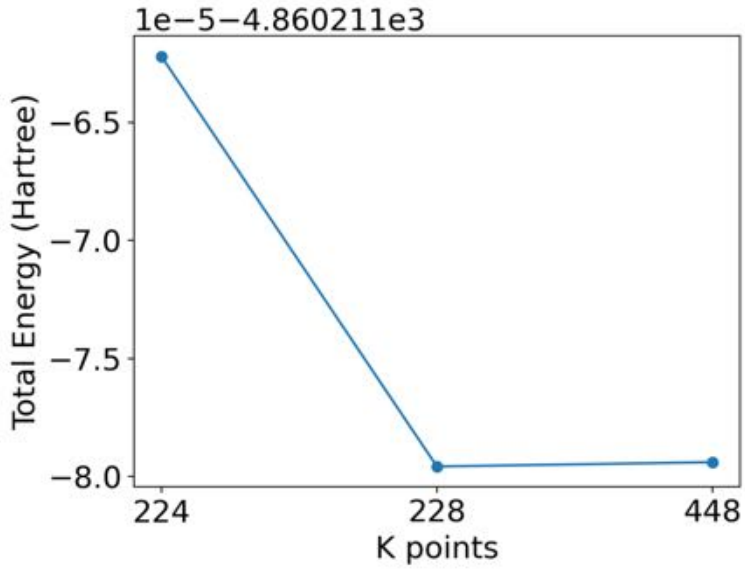

Figure 3.11 K points grid test performed in a (S,Se) simple unit cell (1x1x1). Note that 224, 228 and 448 stands for 2x2x4, 2x2x8 and 4x4x8 K points, respectively.

system using a 1x1x2 supercell of the crystallographic cell with reduced symmetry to explore the lowest energy spin unrestricted magnetic solutions and the restricted closed-shell solution with the simplest primitive cell to represent the lowest metallic solution. These solutions will be described in Chapter 4. Note that the supercell *c* value has been doubled in order to allow AFM and FM interactions along the π-stack direction. The sampled K points grid has been tested in a simple unit cell calculation (1x1x1) of (S,Se) material. Note that accuracy using a 1x1x1 unit cell converges towards 2x2x8 K points grid (see Figure 3.11). Therefore, since we have doubled the cell in the *c* direction, the 1x1x2 supercell ensures there will be enough accuracy for energy calculation due to the choice of K points.

Dimer cluster model calculations

Once all the pairs of radicals that might be candidate to couple magnetically have been selected (as illustrated in Section 3.3.1.**),** the J_{AB} magnetic interactions are computed by means of energy differences according to the general Heisenberg Hamiltonian ($\hat{H} = -2\sum_{A,B}^{N} J_{AB}\hat{S}_A \cdot \hat{S}_B$). Within the Density Functional Theory DFT framework, for pairs of radicals with S = ½, J_{AB} can be computed as $J_{AB} = E^{S,BS} - E^{T}$, where $E^{S,BS}$ and E^{T} are the energies of the broken-

Document signat digitalment per: CRISTINA RONCERO BARRERO

symmetry[56,57,58,59] open-shell singlet and triplet states, respectively (when there is no overlap between SOMOs, see explanation on Section 3.1.2). All the energy calculations were performed at DFT/UB3LYP[60,61] level as implemented in Gaussian09 package[62] using a 6-311+G(d,p) Pople basis set to provide diffuse and polarization functions to better describe the interactions between neutral radicals[63,64,65]. Note that the B3LYP functional has been widely used in the characterisation of these materials and has shown to give consistent and reliable results[66,67,68]. Let us remark here that in all calculations spin multiplicity, spin density and singly-occupied natural orbitals where examined as to be certain that the results were valid. In Chapter 5, cluster results will be reported and compared with those obtained in Chapter 4 using the periodic evaluation of J_{AB}.

3.3.2.2 Reorganization energy

The λ_{in} reorganization energy has been computed for all four bisDTA-derivative compounds using an isolated monomer. Geometry relaxations have been performed for neutral (R^N) and charged (R^C) isolated monomers acting as D donor and A acceptor (see Figure 3.4 as a reminder for hole transfer mechanism) at UB3LYP level[69] with a 6-311+G(d,p) basis set[70,71,72] in vacuum. Secondly, $E_N(R^N), E_N(R^C)$ and $E_c(R^N), E_c(R^C)$ have been evaluated by means of single-point energy calculations at UB3LYP/6-311+G(d,p) level using the previously neutral and charged optimized geometries for monomers acting as oxidant or reducer agents. Finally, λ_{in} is obtained by means of $\lambda_{in} = [E_c(R^N) + E_N(R^C)] - [E_c(R^C) + E_N(R^N)]$ (Equation 26). All DFT calculations have been performed using the Gaussian09 software[73]. In addition, all four energies (namely, $E_N(R^N), E_N(R^C)$, $E_c(R^N), E_c(R^C)$) have been re-evaluated at CASSCF and CASPT2 levels using a (7,7) for neutral monomers and, (7,6) and (7,8) active spaces for cation and anion, respectively. Note that (m,n) refers to (number of orbitals, number of electrons). The choice of the seven molecular orbitals and seven electrons active space was made to take into account both the symmetry and the occupation of the orbitals. The selected active space was the minimal that recovered the symmetry of the orbitals. Note that the occupation numbers of the active orbitals range from 0.05 and 1.94 (see active spaces of a (3,3), (5,5) and (7,7) calculations for the (S,S) bisDTA material).

Document signat digitalment per: CRISTINA RONCERO BARRERO

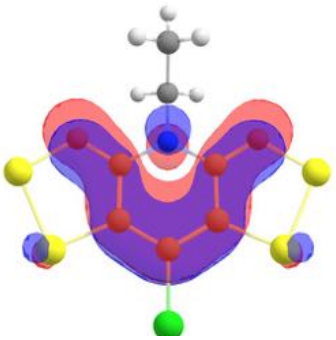

1.938

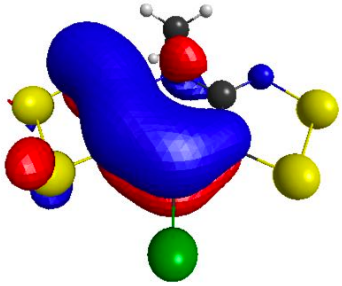

1.936

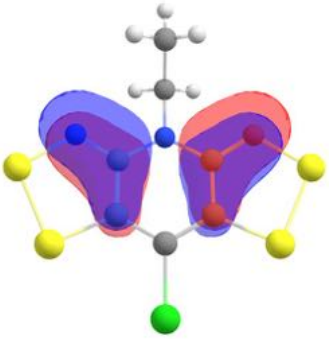

1.935

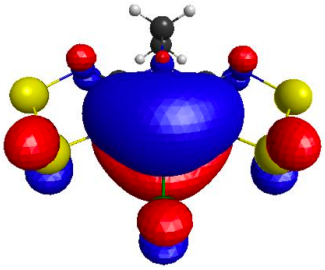

1.914

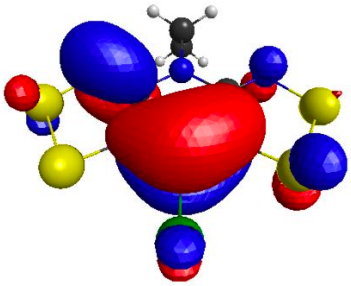

1.898

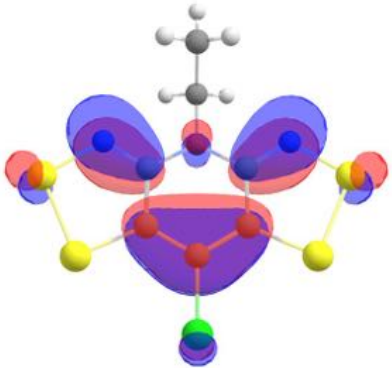

1.884

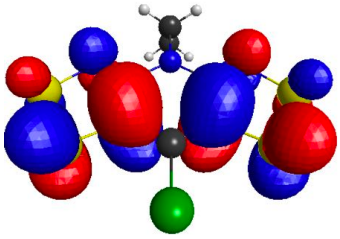

1.000

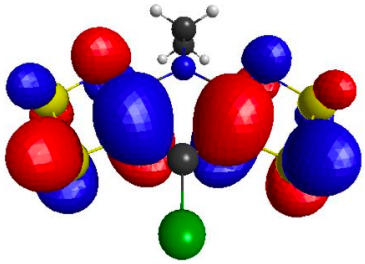

1.000

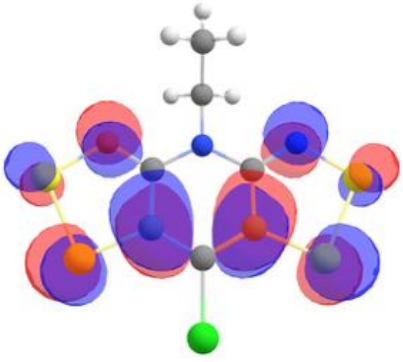

1.000

Document signat digitalment per: CRISTINA RONCERO BARRERO

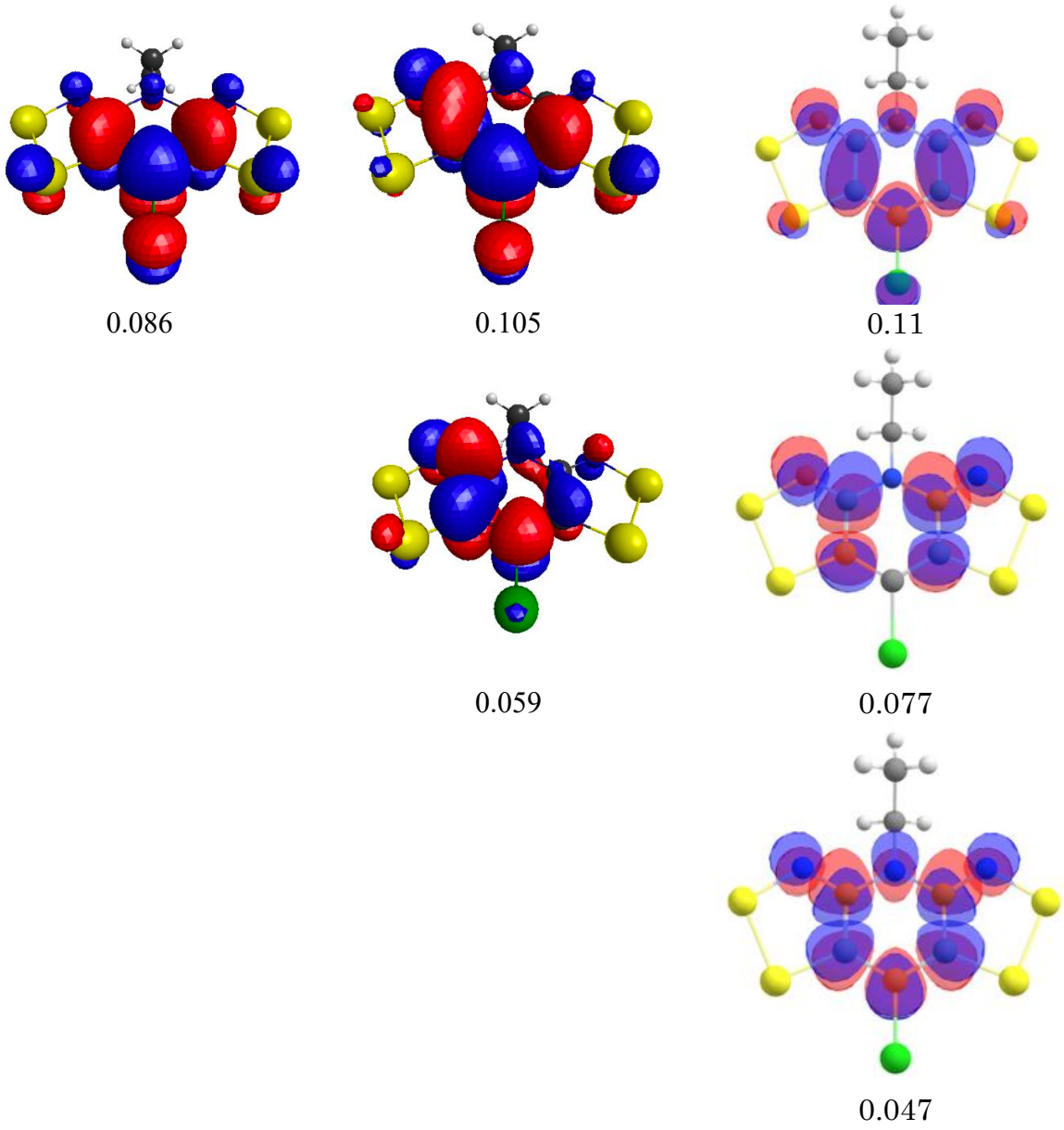

Figure 3.12 Representation of natural orbitals included in the active spaces of CASSCF(3,3), (5,5) and (7,7). Occupation numbers haven included below each orbital.

3.3.2.3 H_{DA} electronic coupling

Neutral reported geometries at 100K[38] have been assumed to be an approximation to the transition state (TS) geometries of the charged potential energy surface, since they fulfil the condition of energy degeneration of the geometry configurations of D donor and A acceptor sites. Therefore, H_{DA} have been evaluated using these TS transition states.

Document signat digitalment per: CRISTINA RONCERO BARRERO

The H_{DA} electronic coupling has been computed using the selected 13 dimers detailed in the previous Section 3.3.1 for all four bisDTA-based S/Se compounds. After the dimer selection, adiabatic state-average energies for the ground (E_1) and the first excited (E_2) states at the TS geometry have been computed at CASSCF level using (15,14) and (13,14) active spaces for anion and cation calculations, respectively.

Note that, since two monomers are included in the calculations, the orbitals included in the active space are twice those chosen in the λ reorganization energy evaluation, and that the total of 15 / 13 electrons comes from subtracting or adding one electron for anion and cation solutions, respectively (see Figure 3.13 for an example of the molecular orbitals included in the active space) Next, the H_{DA} for hole (H_{DA}^{+}) and electron (H_{DA}^{-}) transport are obtained using previously calculated E_1 and E_2 energies at CASSCF level for all D···A pairs extracted from each one of the bisDTA-systems according to $\Delta E_{12} = E_2 - E_1 = 2|H_{DA}|$ (Equation 3.24). Note that, in order to include the effect of the electronic correlation, E_1 and E_2 energies have been re-evaluated using a second order perturbation method (CASPT2). All CASSCF and CASPT2 calculations have been performed using MOLCAS 8.0 code[74] and ANO RCC-type basis functions.[75] The contractions of the basis set were the following: [9s8p3d] for de Se, [7s6p1d] for S and Cl, [5s4p1d] for C and N, and [3s1p] for H. The standard zeroth Hamiltonian for CASPT2 calculations has been modified with an IPEAshift of 0 eV (the default value for MOLCAS 8.0 is 0.25 eV) and shift equal to 0.2 eV (see Appendix 2 for further details about the selection of the CASPT2 parameters).

Document signat digitalment per: CRISTINA RONCERO BARRERO

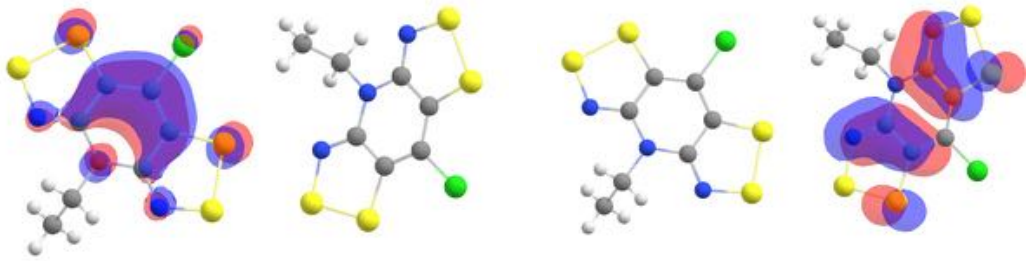

1.951149 1.943705

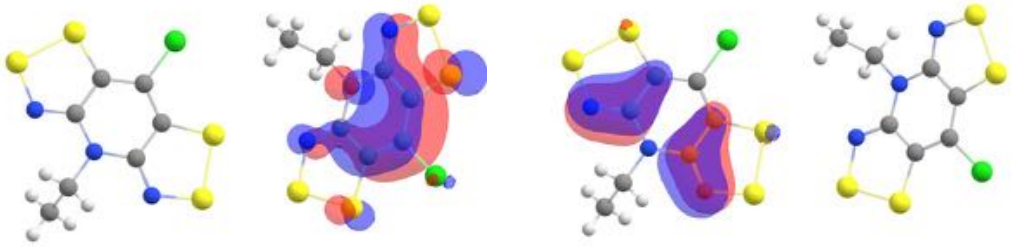

1.939704 1.931612

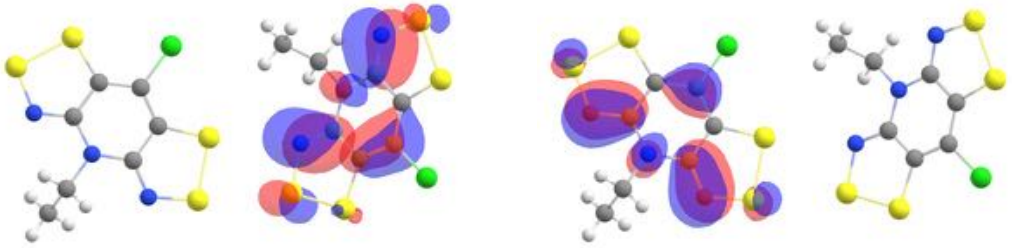

1.893340 1.873670

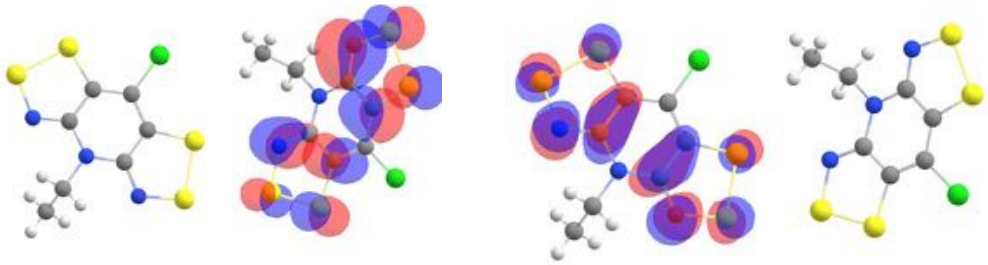

1.004116 0.123490

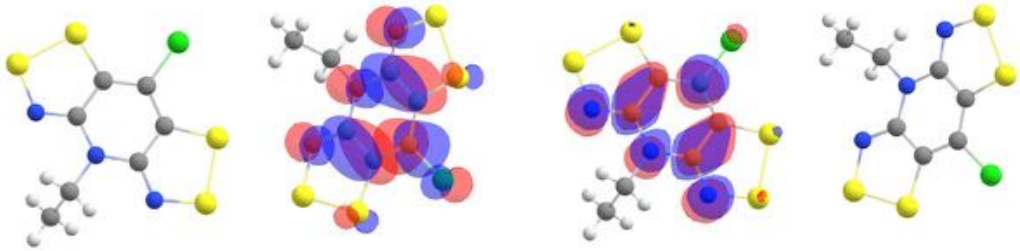

0.106579 0.074109

Document signat digitalment per: CRISTINA RONCERO BARRERO

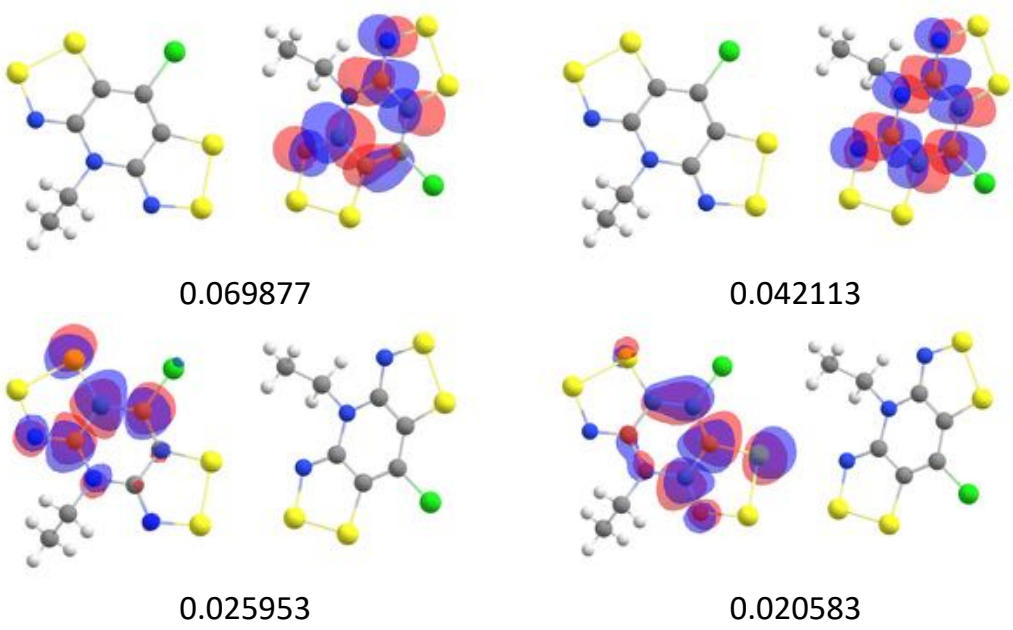

Figure 3.13. Example of molecular orbitals included in a (14,#) active space to evaluate the H_{DA} electronic coupling between two bisDTA monomers at CASSCF level. Represented orbitals and occupation numbers belong to the (S,S) 2b (14,13) calculation.

3.4 References

1 Deumal, M., Bearpark, M. J., Novoa, J. J., & Robb, M. A. (2002). Magnetic properties of organic molecular crystals via an algebraic Heisenberg Hamiltonian. Applications to WIL VIW, TOLKEK, and KAXHAS nitronyl nitroxide crystals. Journal of Physical Chemistry A, 106(7), 1299–1315. https://doi.org/10.1021/jp015512u

2 Novoa, J. J., Deumal, M., & Jornet-Somoza, J. (2011). Calculation of microscopic exchange interactions and modelling of macroscopic magnetic properties in molecule-based magnets. Chemical Society Reviews, 40(6), 3182–3212. https://doi.org/10.1039/c0cs00112k

3 C. Herring, inMagnetism, ed. G. T. Rado and H. Suhl, AcademicPress, New York, 1966, vol. IIB, p. 5.

4 W. Heisenberg,Z. Phys.,1926,38,411

5 P. A. M. Dirac,Proc. R. Soc. London,Ser. A,1926,112,661

6 Björn O. Roos, Peter R. Taylor, and Per E. M. Siegbahn. A complete active space SCF method (CASSCF) using a density matrix formulated super-CI approach. Chem. Phys., 48:157-173, 1980.

7 Björn O. Roos. The complete active space self-consistent field method and its applications in electronic structure calculations. In K. P. Lawley, editor, Ab Initio Methods in Quantum Chemistry Part II, volume 69 of Advances in

Document signat digitalment per: CRISTINA RONCERO BARRERO

Chemical Physics, pages 399-445. John Wiley & Sons, Hoboken, NJ, USA, 1987.

8 Finley, J., Malmqvist, A., Roos, B. O., Serrano-Andres¨´, L., & Andres¨´, A. (1998). The multi-state CASPT2 method a ˚ a a b. In Chemical Physics Letters (Vol. 288).

9 B. O. Roos, K. Andersson, M. P. Fu ¨lscher, P.-A ˚. Malmqvist,L. Serrano-Andre´s, K. Pierloot and M. Mercha´n,Adv. Chem.Phys., 1996,93, 219

10 P. Hohenberg and W. Kohn, "Inhomogeneous Electron Gas," Phys. Rev., 136 (1964) B864-B71. DOI: 10.1103/PhysRev.136.B864

11 R. G. Parr and W. Yang,Density Functional Theory of Atoms and Molecules, Oxford University Press, Oxford, 1994.

12 L. Noodleman,J. Chem. Phys., 1981,74, 5737

13 L. Noodleman and E. Davidson,Chem. Phys., 1986,109, 131

14 Ref ejemplos DFT-BS en syst. Periódicos y/o clusters

15 A. D. Becke, J. Chem. Phys. 1993, 98, 1372.

16 C. Lee, W. Yang and R. G. Parr, Phys. Rev. B 1988, 37, 785–789.

17 T. Francese, J. Ribas-Arino, J. J. Novoa, R. W. A. Havenith, R. Broer, C. de Graaf, M. Deumal, "The magnetic fingerprint of dithiazolyl-based molecule magnets", *Phys. Chem. Chem. Phys.*, 2018, **20**, 20406–20416.

18 M. Fumanal, S. Vela, J. Ribas-Ariño, J. J. Novoa, "On the Importance of Thermal Effects and Crystalline Disorder in the Magnetism of Benzotriazinyl-Derived Organic Radicals", Chem. Asian J. 2014, 9, 3612-3622.

19 R. Costa, R. Valero, D. Reta Mañeru, I. de P. R. Moreira, and F. Illas, "Spin Adapted versus Broken Symmetry Approaches in the Description of Magnetic Coupling in Heterodinuclear Complexes", J. . Chem. Theory Comput. 2015, 11, 1006–1019.

20 D. Reta Mañeru, Arun K. Pal, I. de P. R. Moreira, S. N. Datta, and F. Illas, "The Triplet–Singlet Gap in the m- Xylylene Radical: A Not So Simple One", J. Chem. Theory Comput., 2014, 10, 335-345.

21 Jornet-Somoza, J., Deumal, M., Borge, J., & Robb, M. A. (2018). A Definition of the Magnetic Transition Temperature Using Valence Bond Theory. Journal of Physical Chemistry A, 122(8), 2168–2177. https://doi.org/10.1021/acs.jpca.7b10657

22 Bearpark, M. J.; Robb, M. A.; Bernardi, F.; Olivucci, M. Molecular mechanics valencebond methods for large active spaces. Application to conjugated polycyclic hydrocar-bons.Chemical Physics Letters1994,217, 513–519.

Document signat digitalment per: CRISTINA RONCERO BARRERO

23 Oberhofer, H., Reuter, K., & Blumberger, J. (2017). Charge Transport in Molecular Materials: An Assessment of Computational Methods. Chemical Reviews, 117(15), 10319–10357. https://doi.org/10.1021/acs.chemrev.7b00086

24 Tiwari, S.; Greenham, N. Charge Mobility Measurement Techniques in Organic Semiconductors.Opt. Quantum Electron. 2009, 41, 69−89

25 Bredas Ref Chem. Rev. 2004

26 R Kittel, C. (n.d.). lntroduction to Solid State Physics.

27 Ashcroft, N. W., & Mermin, N. D. (1976). Solid State Physics.

28 Dong, H., Fu, X., Liu, J., Wang, Z., & Hu, W. (2013). 25th Anniversary Article: Key Points for High-Mobility Organic Field-Effect Transistors. In Advanced Materials (Vol. 25, Issue 43, pp. 6158–6183). https://doi.org/10.1002/adma.201302514

29 V. Rühle, A. Lukyanov, F. May, M. Schrader, T. Vehoff, J. Kirkpatrick, B. Baumeier, D. Andrienko, *J. Chem. Theory Comput.*, **7** (2011), 3335.

30 Stehr, V., Pfister, J., Fink, R. F., Engels, B., & Deibel, C. (2011). First-principles calculations of anisotropic charge-carrier mobilities in organic semiconductor crystals. Physical Review B - Condensed Matter and Materials Physics, 83(15), 1–14. https://doi.org/10.1103/PhysRevB.83.155208

31 Deng, W. Q., & Goddard, W. A. (2004). Predictions of hole mobilities in oligoacene organic semiconductors from quantum mechanical calculations. Journal of Physical Chemistry B, 108(25), 8614–8621. https://doi.org/10.1021/jp0495848

32 Marcus, R. A. (1956). On the theory of oxidation-reduction reactions involving electron transfer. I. The Journal of Chemical Physics, 24(5), 966–978. https://doi.org/10.1063/1.1742723

33 Marcus, R. A. (1993). Electron Transfer Reactions in Chemistry: Theory and Experiment (Nobel Lecture). Angewandte Chemie International Edition in English, 32(8), 1111–1121. https://doi.org/10.1002/anie.199311113

34 S. T. Bromley, M. Mas-Torrent, P. Hadley, and C. Rovira, “Importance of intermolecular interactions in assessing hopping mobilities in organic field effect transistors: Pentacene versus dithiophene-tetrathiafulvalene,” Journal of the American Chemical Society, vol. 126, no. 21, pp. 6544–6545, Jun. 2004, doi: 10.1021/ja049762a.

35 S. T. Bromley, F. Illas, and M. Mas-Torrent, “Dependence of charge transfer reorganization energy on carrier localisation in organic molecular crystals,” Physical Chemistry Chemical Physics, vol. 10, no. 1, pp. 121–127, 2008, doi: 10.1039/b713688a.

36 J. Spencer, L. Scalfi, A. Carof, and J. Blumberger, “Confronting surface hopping molecular dynamics with Marcus theory for a molecular donor-acceptor system,” Faraday Discussions, vol. 195, pp. 215–236, 2016, doi: 10.1039/c6fd00107f.

37 A. Bondi, J. Phys. Chem., 1964, 68, 441–451

38 C.M. Robertson, A.A. Leitch, K. Cvrkalj, D.J.T. Myles, R.W. Reed, P.A. Dube, R.T. Oakley, J. Am. Chem. Soc., 2008, 130, 14791–14801

Document signat digitalment per: CRISTINA RONCERO BARRERO

39 A.A. Leitch, X. Yu, S.M. Winter, R.A. Secco, P.A. Dube, R.T. Oakley, J. Am. Chem. Soc., 2009, 131, 7112–7125

40 C.M. Robertson, A.A. Leitch, K. Cvrkalj, R.W. Reed, D.J.T. Myles, P.A. Dube, R.T. Oakley, J. Am. Chem. Soc., 2008, 130, 8414–8425 – Paper EXP

41 P. Giannozzi, S. Baroni, N. Bonini, M. Calandra, R. Car, C. Cavazzoni, D. Ceresoli, G.L. Chiarotti, M. Cococcioni, I. Dabo, A. Dal Corso, S. de Gironcoli, S. Fabris, G. Fratesi, R. Gebauer, U. Gerstmann, C. Gougoussis, A. Kokalj, M. Lazzeri, L. Martin-Samos, N. Marzari, F. Mauri, R. Mazzarello, S. Paolini, A. Pasquarello, L. Paulatto, C. Sbraccia, S. Scandolo, G. Sclauzero, A.P. Seitsonen, A. Smogunov, P. Umari, R.M. Wentzcovitch, J. Phys. Condens. Matter, 2009, 21, 395502

42 J.P. Perdew, K. Burke, M. Ernzerhof, Phys. Rev. Lett., 1996, 77, 3865–3868

43 J.P. Perdew, K. Burke, M. Ernzerhof, Phys. Rev. Lett., 1997, 78, 1396–1396

44 S. Grimme, J. Comput. Chem., 2006, 27, 1787–1799

45 R. Dovesi, R. Orlando, B. Civalleri, C. Roetti, V. R. Saunders, and C. M. Zicovich-Wilson, Z. Kristallogr. 2005, 220, 571.

46 R. Dovesi, V. R. Saunders, C. Roetti, R. Orlando, C. M. Zicovich-Wilson, F. Pascale, B. Civalleri, K. Doll, N. M. Harrison, I. J. Bush, P. D'Arco, and M. Llunell, CRYSTAL09 User's Manual (University of Torino, Torino, 2009).

47 C. Gatti, V. R. Saunders,C. Roetti, "Crystal-field effects on the topological properties of the electron-density in molecular-crystals - the case of urea", J. Chem. Phys. 1994, 101, 10686-10696.

48 P. J. Hay and W. R. Wadt, "Ab initio effective core potentials for molecular calculations. Potentials for main group elements Na to Bi", J. Chem. Phys. 1985, 82, 284.

49 P. Durand and J. C. Barthelat, "A theoretical method to determine atomic pseudopotentials for electronic structure calculations of molecules and solids", Theor. Chim. Acta 1975, 38, 283–302.

50 K. A. Peterson, D. Figgen, E. Goll, H. Stoll, M. Dolg, "Systematically convergent basis sets with relativistic pseudopotentials. II. Small-core pseudopotentials and correlation consistent basis sets for the post-d group 16-18 elements", J. Chem. Phys. 2003, 119, 11113-11123.

51 T. Ouazzani, A. Lichanot, C. Pisani, C. Roetti, "Relaxation and electronic structure of surfaces in lithium sulphide: a Hartree-Fock ab initio approach", J. Phys. Chem. Solids 1993, 54, 1603-1611.

52 J. Heyd, J. E. Peralta, G. E. Scuseria, and R. L. Martin, "Energy Band Gaps and Lattice Parameters Evaluated with the Heyd-Scuseria-Ernzerhof Screened Hybrid Functional", J. Chem. Phys. 2005, 123, 174101.

53 M. Prencipe, Laurea Thesis (pages 87-89) (1990).

54 https://www.crystal.unito.it/basis-sets.php

Document signat digitalment per: CRISTINA RONCERO BARRERO

55 C. M. Robertson, S. M. Winter, J. A. K. Howard, M. R. Probert and R. T. Oakley, "Low temperature insights into the crystal and magnetic structure of a neutral radical ferromagnet", *Chem. Commun*. 2021, **57**, 10238-10241.

56 L. Noodleman, J. Chem. Phys., 1981, 74, 5737–5743

57 L. Noodleman, E.R. Davidson, Chem. Phys., 1986, 109, 131–143

58 R. Caballol, O. Castell, F. Illas, I. de P.R. Moreira, J.P. Malrieu, J. Phys. Chem. A, 1997, 101, 7860–7866

59 F. Illas, I. de P.R. Moreira, J.M. Bofill, M. Filatov, Phys. Rev. B, 2004, 70, 132414

60 A.D. Becke, J. Chem. Phys., 1993, 98, 5648–5652

61 C. Lee, W. Yang, R.G. Parr, Phys. Rev. B, 1988, 37, 785-789

62 M.J. Frisch, G.W. Trucks, H.B. Schlegel, G.E. Scuseria, M.A. Robb, J.R. Cheeseman, G. Scalmani, V. Barone, G.A. Petersson, H. Nakatsuji, X. Li, M. Caricato, A. Marenich, J. Bloino, B.G. Janesko, R. Gomperts, B. Mennucci, H.P. Hratchian, J.V. Ortiz, A.F. Izmaylov, J.L. Sonnenberg, D. Williams-Young, F. Ding, F. Lipparini, F. Egidi, J. Goings, B. Peng, A. Petrone, T. Henderson, D. Ranasinghe, V.G. Zakrzewski, J. Gao, N. Rega, G. Zheng, W. Liang, M. Hada, M. Ehara, K. Toyota, R. Fukuda, J. Hasegawa, M. Ishida, T. Nakajima, Y. Honda, O. Kitao, H. Nakai, T. Vreven, K. Throssell, J.A. Montgomery, Jr., J.E. Peralta, F. Ogliaro, M.J. Bearpark, J.J. Heyd, E. Brothers, K.N. Kudin, V.N. Staroverov, T. Keith, R. Kobayashi, J. Normand, K. Raghavachari, A. Rendell, J.C. Burant, S.S. Iyengar, J. Tomasi, M. Cossi, J.M. Millam, M. Klene, C. Adamo, R. Cammi, J.W. Ochterski, R.L. Martin, K. Morokuma, O. Farkas, J.B. Foresman, D.J. Fox, Gaussian09, Revision B.02, Gaussian, Inc., Wallingford CT (United Kingdom), 2016.

63 A.D. McLean, G.S. Chandler, J. Chem. Phys., 1980, 72, 5639–5648

64 R. Krishnan, J.S. Binkley, R. Seeger, J.A. Pople, J. Chem. Phys., 1980, 72, 650–654

65 R.C. Binning, L.A. Curtiss, J. Comput. Chem., 1990, 11, 1206–1216

66 S.M. Winter, K. Cvrkalj, P.A. Dube, C.M. Robertson, M.R. Probert, J.A.K. Howard, R.T. Oakley, Chem. Commun., 2009, 7306–7308

67 C.M. Robertson, A.A. Leitch, K. Cvrkalj, D.J.T. Myles, R.W. Reed, P.A. Dube, R.T. Oakley, J. Am. Chem. Soc., 2008, 130, 14791–14801

68 C. Climent, S. Vela, J. Jornet-Somoza, M. Deumal, Phys. Chem. Chem. Phys., 2019, 21, 12184–12191

69 A. D. Becke, "Density-functional thermochemistry. III. The role of exact exchange," The Journal of Chemical Physics, vol. 98, no. 7, pp. 5648–5652, 1993, doi: 10.1063/1.464913.

70 A. D. McLean and G. S. Chandler, "Contracted Gaussian basis sets for molecular calculations. I. Second row atoms, Z=11-18," The Journal of Chemical Physics, vol. 72, no. 10, pp. 5639–5648, 1980, doi: 10.1063/1.438980.

71 R. Krishnan, J. S. Binkley, R. Seeger, and J. A. Pople, "Self-consistent molecular orbital methods. XX. A basis set for correlated wave functions," The Journal of Chemical Physics, vol. 72, no. 1, pp. 650–654, 1980, doi: 10.1063/1.438955.

Document signat digitalment per: CRISTINA RONCERO BARRERO

72 R. C. Binning and L. A. Curtiss, “Compact contracted basis sets for third-row atoms: Ga–Kr,” Journal of Computational Chemistry, vol. 11, no. 10, pp. 1206–1216, 1990, doi: 10.1002/jcc.540111013.

73 M. J. Frisch et al., “Gaussian09.” Gaussian, Inc., Wallingford CT, 2013.

74 F. Aquilante et al., “Molcas 8: New capabilities for multiconfigurational quantum chemical calculations across the periodic table,” Journal of Computational Chemistry, vol. 37, no. 5, pp. 506–541, Feb. 2016, doi: 10.1002/jcc.24221.

75 rn O. Roos, R. Lindh, ke Malmqvist, V. Veryazov, and P.-O. Widmark, “Main Group Atoms and Dimers Studied with a New Relativistic ANO Basis Set,” 2004, doi: 10.1021/jp031064.

Document signat digitalment per: CRISTINA RONCERO BARRERO

PART II. RESULTS & DISCUSSION

Document signat digitalment per: CRISTINA RONCERO BARRERO

Document signat digitalment per: CRISTINA RONCERO BARRERO

Chapter 4. Periodic Electronic Structure In BisDTA Materials

In this first chapter of results, we investigate the electronic structure and magnetic behaviour of the four members of the bisDTA-derived multifunctional family of compounds introduced in Chapter 2 (namely, (S,S), (S,Se), (Se,S) and (Se,Se)) by means of electronic band structure calculations and hybrid density functional theory (DFT) based methods to rationalise their static electronic structure. The study of different open-shell magnetic solutions has been used to characterize the ground state of the four bisDTA S/Se materials and connect them to their experimental magnetic behaviour. Additionally, the analysis of the projected density of states (DOS) and Mulliken charge and spin distribution will point out to the relevant chemical positions within the bisDTA ring involved in the magnetic and electric properties. The main goal of this study consists in establishing a reference picture of the ground state electronic structure of these materials to provide a rationale for their magnetic properties and electric conduction behaviour. In addition, we also aim at establishing the extent and limitations of the electron band structure approximation to describe the electronic structure and properties of these interesting multifunctional molecular systems. The study presented in this chapter has been performed using the crystallographic data reported at 100 K[1] and a (Se,Se) additional structure at 2K[2]. To the best of our knowledge, this is the first work where a hybrid DFT approach is used to perform electronic band structure calculations of the closed-shell metallic state and the open-shell states with ferromagnetic and antiferromagnetic spin configurations of an organic radical-based conductor. In fact, the use of hybrid functionals to examine the electronic structure of organic radical-based molecular materials is still very uncommon in periodic calculations.[3] Indeed, most of the analyses of electron band structure of organic

Document signat digitalment per: CRISTINA RONCERO BARRERO

radical-based materials so far reported are based on simpler models such as extended Hückel Theory[4,5,6,7,8,9] or the generalized gradient approximation to density-functional theory.[10,11,12,13,14-19]

This Chapter is structured in a first section focused on the discussion of the nature of the ground state for bisdithiazolyl (S,S), thiaselenazolyl (S,Se) and (Se,S) and bisdiselenazolyl (Se,Se) compounds in order to address the validity of the band model to interpret their physical properties. Next, their electronic structure will be inspected to gain insight into the spin distribution within each bisDTA radical. The third and final section will deal with the magnetism of these four compounds from a periodic perspective. Accordingly, different A···B radical pair coupling schemes will be explored to rationalise the overall magnetism of the bisDTA molecular magnets under study.

4.1. Nature of the ground state.

The analysis of the electronic structure and properties of the family of selenium substituted bisdithiazolyl bisDTA multifunctional molecular materials has been performed using their simple conventional unit cell to construct the ferromagnetic (FM) and the closed-shell (CS) electronic solutions, and a 1x1x2 (according to *a*x*b*x*c* axes) supercell to construct four different broken symmetry (BS) antiferromagnetic solutions with $S_z = 0$ (see AFM, AFM1, AFM2 and AFM3 in Figure 4.1). Note that the supercell, constructed doubling the unit cell along the *c*-axis, allow us to compute different spin arrangements along the π-stacking direction.

According to the results obtained, all the systems show an open-shell ground state, in agreement with the radical nature of their constituent molecular radical entities that have one unpaired electron per molecule (see energies per unit formula relative to the FM solution listed in Table 4.1). In all cases, all open-shell solutions are well below the closed-shell CS solution (which lies *ca.* 2000 cm^{-1} above the FM solution). The CS solution is metallic and the open-shell

Document signat digitalment per: CRISTINA RONCERO BARRERO

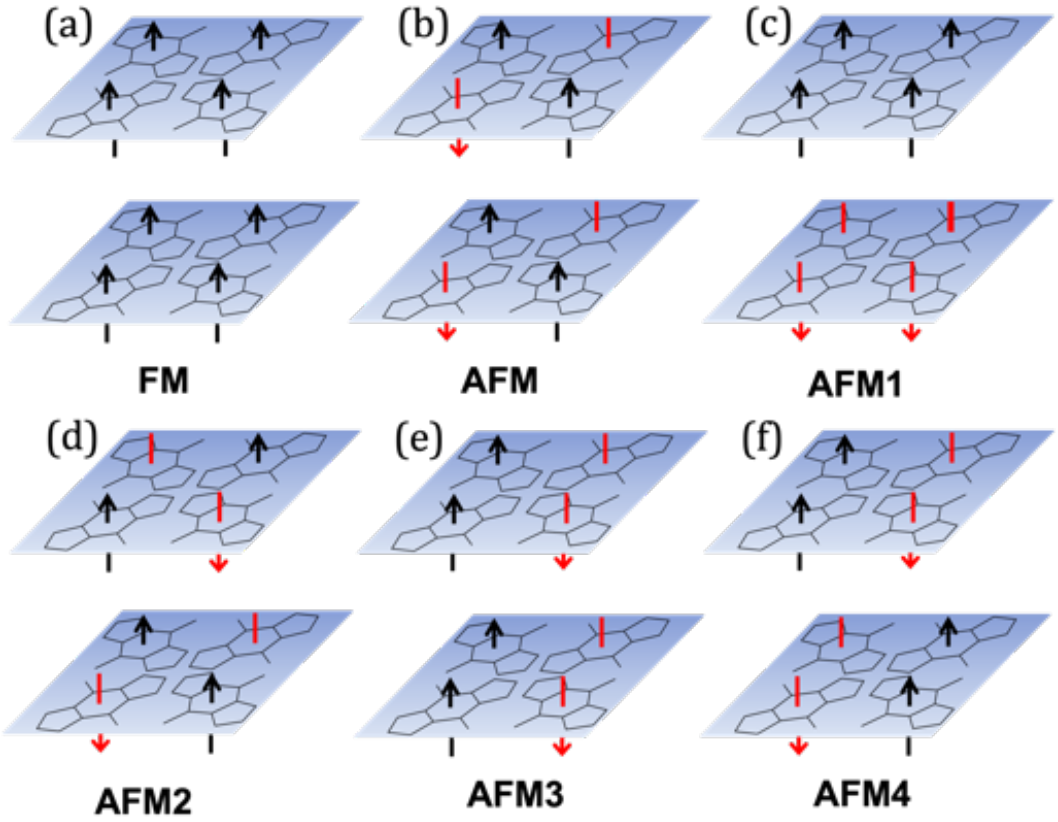

Figure 4.1. Schematic representation of the spin arrangements of the calculated (a) FM and (b-f) AFM# electronic solutions. Planes are perpendicular to the columns depicted in Figure 2.3b, i.e. to the direction of the π-stacking, and contain the centre of mass of the depicted molecules (*ab*-plane). Radicals are included to guide the eye. Spin-up and spin-down depicted in black and red, respectively.

solutions are insulating with an indirect gap around 1.3 eV (see Table 4.2), which classifies these systems as semiconductor magnetic materials. Analysis of the relative energies obtained for the different solutions shows that the ground state is different for each compound. The ferromagnetic FM solution appears to be the most stable for (S,Se) and (Se,Se) systems, whereas some antiferromagnetic AFM interactions emerge as most stable for (S,S) and (Se,S) systems. Accordingly, these systems behave as either antiferromagnet (e.g (Se,S)) or shows no magnetic order if the interactions are small enough (e.g. (S,S)). The different stabilities of the studied solutions can be correlated with the experimental magnetic behaviour of the systems.[1] The (S,Se) and (Se,Se) systems are reported to behave as bulk ferromagnets, and their AFM# states lie above 5.3 cm^{-1} for (S,Se) and 7.5 cm^{-1} for (Se,Se). On the other hand, the (Se,S) derivative, that has

Document signat digitalment per: CRISTINA RONCERO BARRERO

Table 4.1. Energy difference per unit formula relative to the ferromagnetic FM solution in cm^{-1} for the four bisDTA-derived compounds studied in this work. Note that AFM# refers to four different broken symmetry (BS) open-shell antiferromagnetic AFM solutions (see Figure 4.1 for spin arrangement). The corresponding values of the CS solution in meV are listed between brackets. For all compounds the experimental crystal structure parameters determined at 100K have been considered whereas for (Se,Se) compound we also include the results for the structure at 2K (last row).

System	CS	AFM	AFM1	AFM2	AFM3	AFM4
(S,S)	2795 (347)	9.2	3.8	–0.7	3.9	1.2
(S,Se)	2478 (307)	23.1	16.2	9.2	5.3	17.2
(Se,S)	2042 (253)	9.6	–1.1	1.3	4.1	-0.3
(Se,Se)	2463 (305)	18.8	11.0	15.0	7.5	13.0
	2418 (300)	18.9	15.2	18.7	7.3	17.3

been experimentally characterized as a spin-canted antiferromagnet, presents the AFM1 solution as the most stable one (1.1 cm^{-1} below the FM solution) in which FM layers are connected antiferromagnetically. Finally, (S,S) shows two almost degenerated ground state solutions (the energy difference is just -0.7 cm^{-1}), the FM and the AFM2 with AFM chains whose radicals are then antiferromagnetically connected along *a*- and *b*-axes. Experimentally, by analysing the magnetic susceptibility measurements, it has been suggested that the observed trend for this (S,S) compound can be explained through a competition between weak local ferromagnetic interactions and weaker antiferromagnetic ones.**¡Error! Marcador no definido.** Therefore, for all the systems, UDFT calculations have been able to capture the magnetic nature of the ground state, as it has been shown by direct comparison with the experimental data.

The analysis of the associated band gaps to the UDFT calculations show that band gaps depend on the magnetic solution, ranging from 1.30-1.45 eV for (S,S), 1.13-1.30 eV for (S,Se), 1.25-1.36 eV for (Se,S), and 1.15-1.24 eV for (Se,Se) (see Table 4.2). Notice that, in the case of (Se,Se), the values for the low temperature solution are almost the same 1.15-1.25 eV. It can be observed that the value of the band gap follows the same tendency than the conductivity

Document signat digitalment per: CRISTINA RONCERO BARRERO

Table 4.2. Calculated band gaps (in eV) of the FM and different BS solutions (see Figure 4.1 for spin arrangement) for S/Se bisDTA-compounds. The two numbers in the FM solution correspond to the $\alpha - \alpha$ and lowest $\alpha - \beta$ gap. Experimental electric conductivity is also given.

System	T/K	σ/ S·cm^{-1}	FM	AFM
(S,S)	100	$3.2 \cdot 10^{-6}$	2.58/1.30	1.34
(S,Se)	100	$1.0 \cdot 10^{-4}$	2.11/1.13	1.15
(Se,S)	100	$2.2 \cdot 10^{-5}$	2.17/1.25	1.26
(Se,Se)	100	$3.0 \cdot 10^{-4}$	2.08/1.15	1.17
	2		2.11/1.15	1.18

System	T/K	AFM1	AFM2	AFM3	AFM4
(S,S)	100	1.43	1.45	1.36	1.43
(S,Se)	100	1.28	1.30	1.31	1.21
(Se,S)	100	1.35	1.36	1.27	1.37
(Se,Se)	100	1.24	1.26	1.24	1.22
	2	1.22	1.24	1.25	1.20

values, with larger values corresponding to lower conductivities (compared with the experimental σ conductivities at 300K listed in Table 4.2). Yet the differences among the band gaps are not large enough to explain by themselves the conductivities found experimentally. Interestingly enough, the band gap is sensitive to the magnetic solution and a significant change of ~0.15 eV for (S,S) and (S,Se) and ~0.11 eV for (Se,S) and (Se,Se) is observed when switching from the FM to the AFM# solutions.

The fact that the closed-shell CS solution is metallic and quite close in energy to the ground state (250-350 meV per unit formula according to Table 4.1) suggests that conductivity in these materials entails different conduction mechanisms, which are temperature-dependent, and that the charged species may have comparable stability. This situation limits the utility of the rigid band model to interpret their properties upon charge injection in the system. However, the characterisation of the electronic structure provides an essential starting point to understand the nature of the ground state conductivity and the magnetic properties of the four isostructural bisDTA-systems.

Document signat digitalment per: CRISTINA RONCERO BARRERO

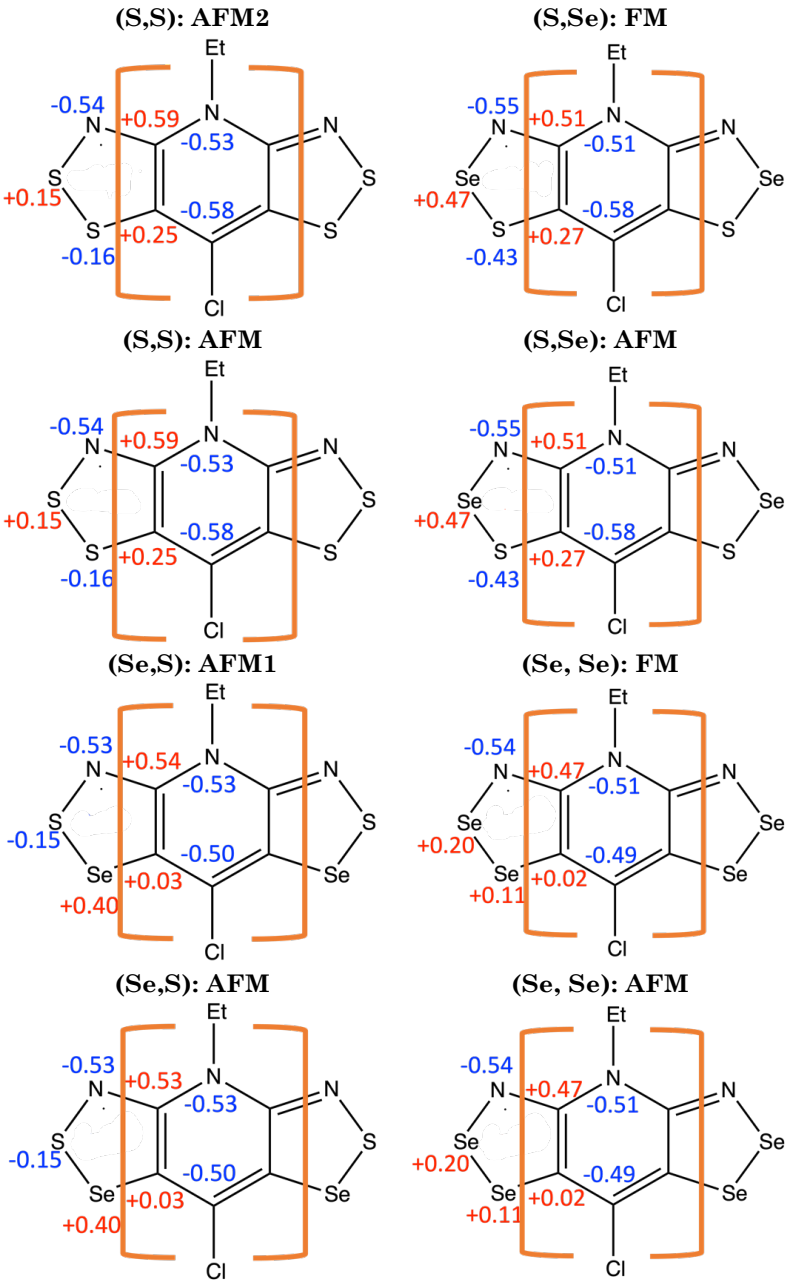

Figure 4.2. Atomic charges (in electrons) obtained from Mulliken analysis for the ground state GS solutions of the systems (top row) and AFM solution (bottom row). Values for the other electronic solutions show small differences (< 0.02) with respect to the values shown here and represent the same electronic distribution for all the molecular entities. See definition of E_1, E_2 and central ring demarcated by brackets.

4.2. Electronic structure.

Further insight in the electronic structure of the systems can be gained by a detailed inspection of charge and spin distribution from Mulliken population analysis for the lowest energy solution of each material (see

Document signat digitalment per: CRISTINA RONCERO BARRERO

Figure 4.2). Although Mulliken charges and spin densities should be taken cautiously, they can provide interesting qualitative information to rationalise the electron distribution in the materials. As a first result, it is important to stress the fact that the values of charges and spin densities are almost independent of the magnetic solution and, hence, the system shows neutral paramagnetic molecular entities with well-defined charge and spin distributions. Even though this can be expected from the molecular nature of these materials, these values have important implications to interpret the structure and properties of these systems.

Regarding the atomic charges, it can be observed that the atoms belonging to the central ring have similar values for all the systems (for a definition, see ring delimited by brackets in Figure 4.2). However, important differences appear when comparing the atoms in the outer rings along the series. While the N atom has a large negative charge of *ca.* -0.54e in all cases, the atoms in E_1 position have negative (positive) charge if being S (Se), whereas atoms in E_2 positions have positive charge if being Se and both positive/negative if S. The E_1-E_2-N charge alternation can be responsible for the tilting and slippage of the molecular units along the *c*-axis that avoids perfect or eclipsed overlapping between radicals along the π-stacking. In turn, this molecular arrangement also reduces the charge repulsion when the N atom of one molecule lays closer to the E_2 position of a nearby molecule (displaced towards the centre of the ring). The subtle interplay between these local interactions becomes important in crystals formed by packing of neutral radicals where weak π-π interactions favour π-stacks and dipole-dipole cancellation orders the resulting columnar structures (C_i and C_4 symmetry operators).

The analysis of the Mulliken spin densities shows that spin distributions are also almost independent of the particular magnetic solution and, thus, each radical can be considered a local S = ½ effective spin particle in order to describe magnetic properties of the systems (see comparison between systems FM and AFM

Document signat digitalment per: CRISTINA RONCERO BARRERO

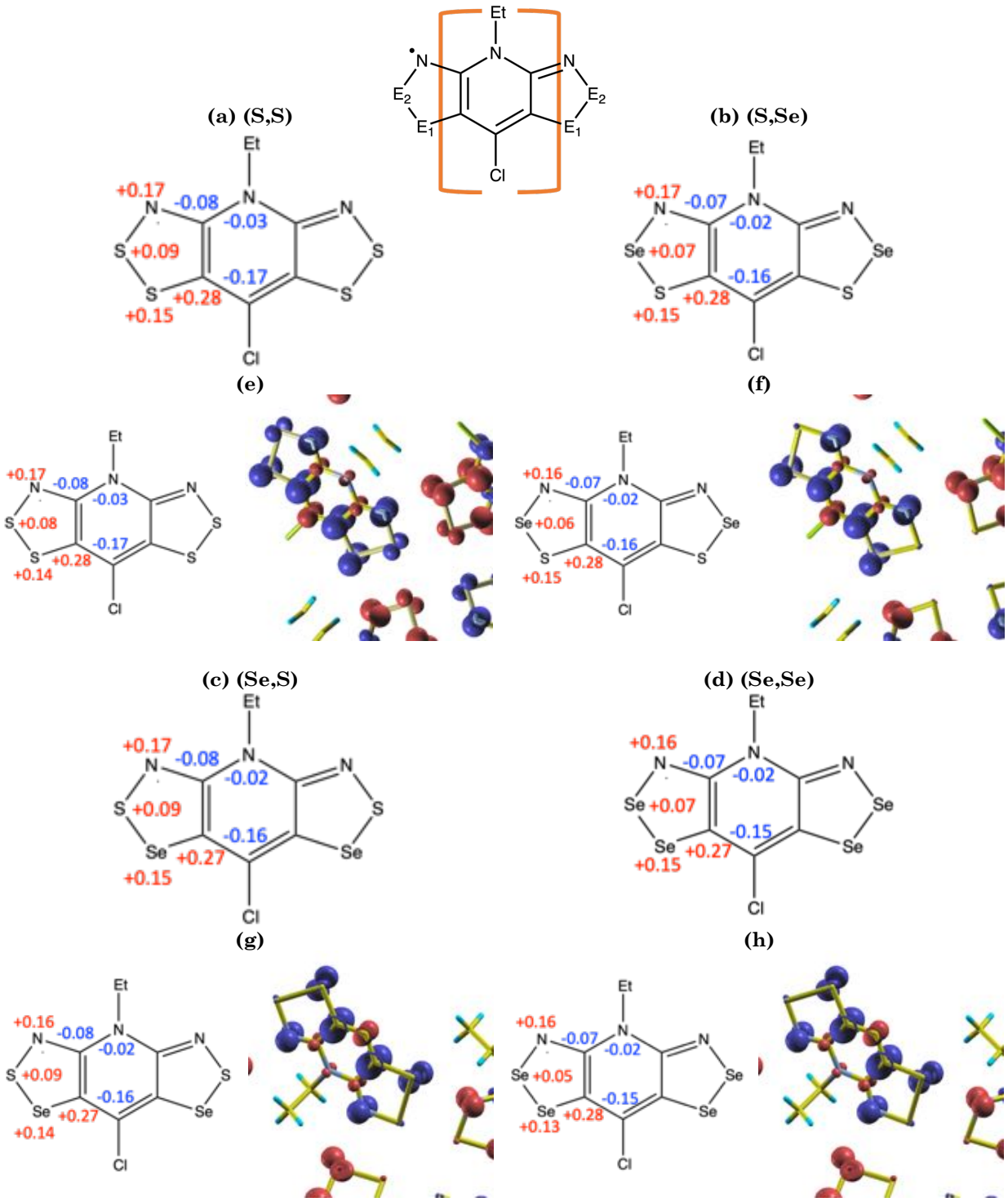

Figure 4.3. Atomic spin densities (in electrons) obtained from Mulliken analysis for the FM (a-d) and AFM solution (e-h) solutions of the (a,e) (S,S), (b,f) (S,Se), (c,g) (Se,S) and (d,h) (Se,Se) systems. Colour code: Alpha and beta spin densities in red and blue, respectively (0.005 a.u. isosurface). These solutions have been chosen to illustrate that these values show small differences (< 0.03) between electronic solutions. See definition of E_1, E_2 and central ring demarcated by brackets.

Document signat digitalment per: CRISTINA RONCERO BARRERO

solutions represented in Figure 4.3). The population analysis shows that one unpaired electron is delocalised over the π-system of each molecular building block and the atomic spin is larger on N, E_1 heteroatoms, and on the C atom of the central ring connected to Cl (see Figure 4.3; note that the central ring denoted by brackets shows similar spin density distribution irrespective of the bisDTA radical). Note that the AFM has been chosen to simplify the comparison since similar values are obtained for all the solutions. This spin distribution implies that the magnetic interactions governing the magnetic properties of these systems are by no means evident from direct observation of the crystal structure since many different intermolecular contacts are possible as shown below, in the following section.

Additional information on the electronic structure of these systems can be obtained from the analysis of the band structure and the projected density of states (see Figures 4.4 and 4.5). The study of the band structure of all four materials using X-Ray data at 100 K shows that, as introduced earlier, all the systems behave as magnetic semiconductors with a gap of *ca.* 1.3 eV and present similar narrow bands with dispersions almost independent of the magnetic solution. Comparison among the four bisDTA derivatives shows small differences regarding the bands dispersion between them. In Figure 4.4, the band structure of the ground state solutions (namely, AFM2 solution for (S,S), FM for (S,Se) and (Se,Se) and AFM1 for (Se,S)) are represented to aid in the comparison between systems (see Appendix 3 for the remaining solutions). It can be observed that the upper valence bands have a small dispersion (*ca.* 0.2 eV that is slightly larger for the (S,S) compound). Yet the conduction band shows more differences in terms of band dispersion: (S,Se) shows a value of 0.25 eV that is significantly larger than the 0.15-0.18 eV values of the remaining systems. This feature may be an explanation for the larger conductivity of this compound in the bisDTA S/Se series that is not justified by the trend in the insulating gap.

Document signat digitalment per: CRISTINA RONCERO BARRERO

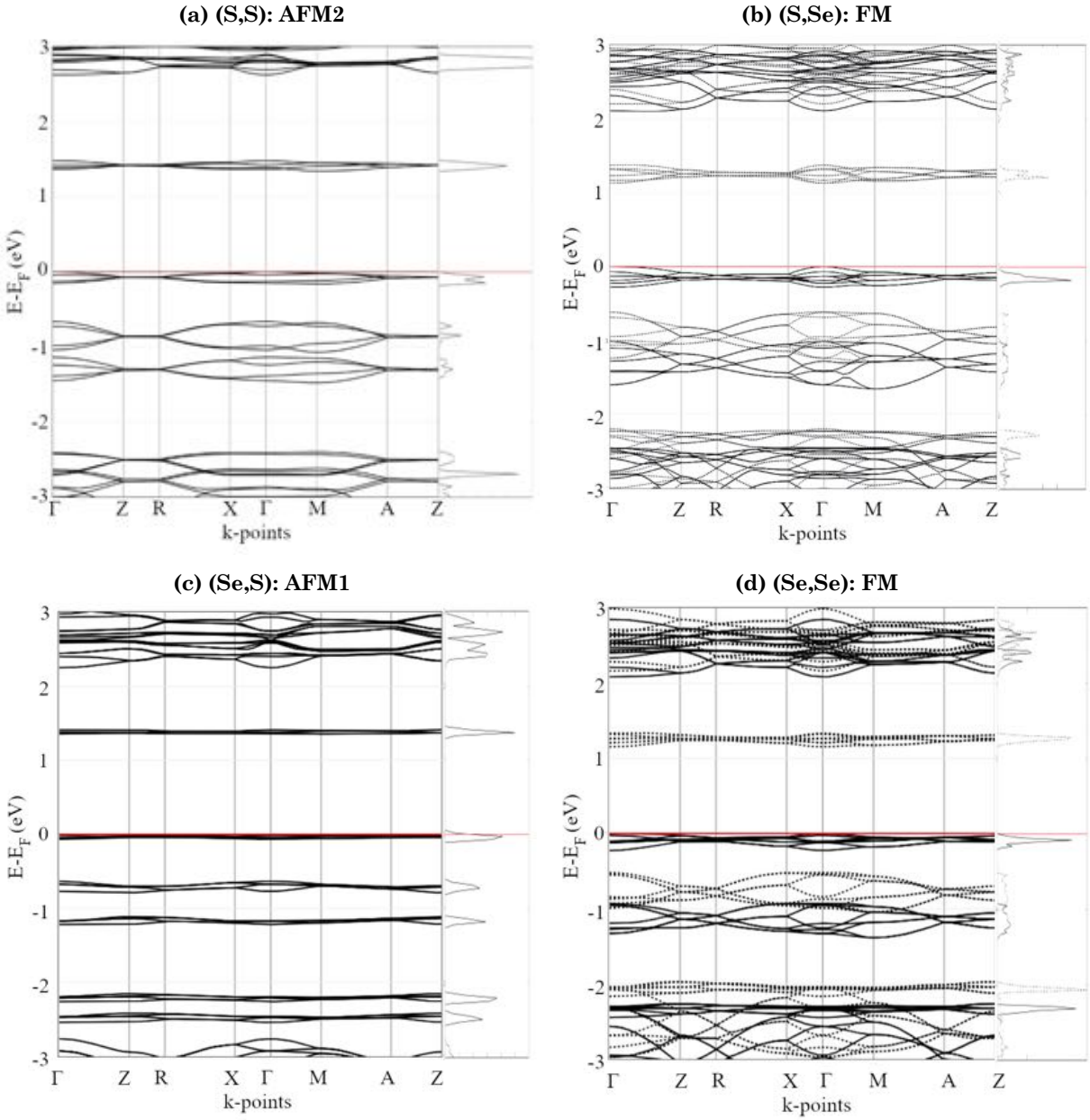

Figure 4.4. Band structure plots and normalized density of states plots of the ground state solutions for all four bisDTA materials, i.e., AFM2 solution for (S,S), FM for (S,Se) and (Se,Se) and AFM1 for (Se,S) compounds. Note that calculations have been carried out using X-Ray data at 100 K.

Additionally, the analysis of the (Se,Se) band structure at 2K shows no relevant modifications on neither the band gap (see values in Table 4.2) nor on band dispersion (see FM solution in Figure 4.5 and Appendix 2 for remaining solutions). Note that the FM solution represented in Figure 4.5 has been obtained in a 1x1x2 supercell, which does not affect the result obtained, but makes the bands more corrugated if compared with the simple cell calculation shown in Figure 4.4.

Document signat digitalment per: CRISTINA RONCERO BARRERO

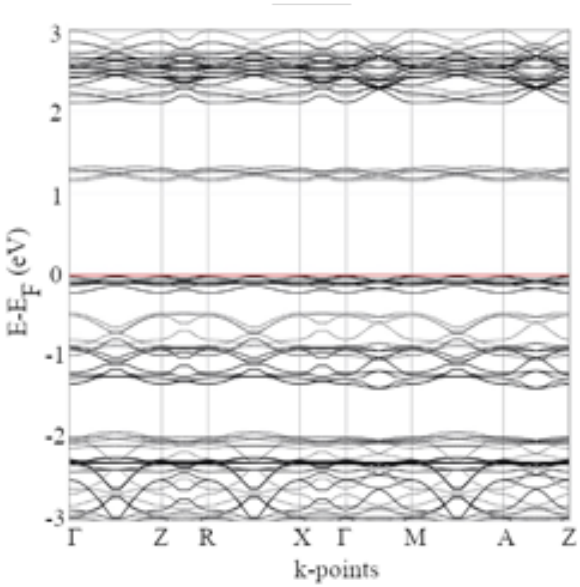

Figure 4.5. Band structure plot of the (Se,Se) FM solution. The calculation has been carried out using the 2 K crystallographic data in a 1x1x2 supercell.

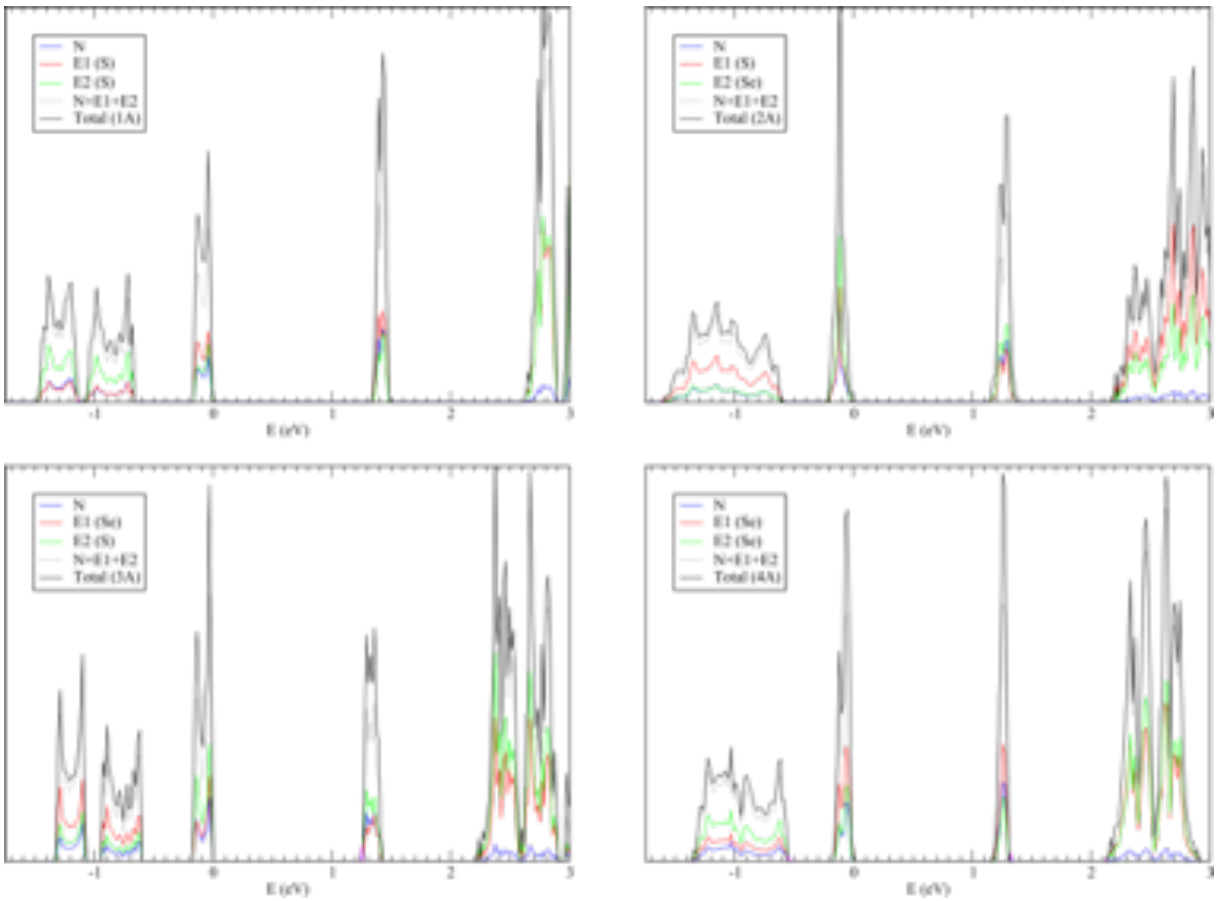

Figure 4.6. Atom projected density of states plots of the AFM solutions for the studied compounds. The top of the valence bands has been set at 0 eV and the AFM solution is used to simplify the comparison between systems (similar for the different solutions except for spin polarization). The ß-density is mirror equivalent and has not been represented for simplification.

Document signat digitalment per: CRISTINA RONCERO BARRERO

The analysis of the projected density of states shows that the upper valence and bottom conduction bands of all four materials are dominated by E_1, E_2 and N π- contributions (see Figure 4.6). The fact that the N-E_1-E_2 heteroatoms have a strong participation in both the valence and the conducting bands defining the insulating state is a clear indication that these atoms will have a decisive contribution in defining the effective conduction paths for electrical conductivity.

4.3. Magnetic interactions.

It has been shown that the spin distribution of the individual paramagnetic centres is almost independent of the particular magnetic solution and, hence, each radical can be considered a local S = ½ effective spin particle in order to describe magnetic properties of the title compounds. In addition, the fact that the systems show magnetic ordering at low temperature deserves a further analysis to identify and calculate the dominant magnetic coupling interactions. As has been introduced in Chapter 2, the description of exchange coupling will be based on the use of the well-known two-body Heisenberg-Dirac-van Vleck spin Hamiltonian (HDVV) in which the isotropic interaction between localized magnetic moments $\widehat{\boldsymbol{S}}_{\boldsymbol{A}}$ and $\widehat{\boldsymbol{S}}_{\boldsymbol{B}}$ is given by

$$\widehat{H} = -2\sum_{A,B}^{N} J_{AB}\widehat{\boldsymbol{S}}_{\boldsymbol{A}} \cdot \widehat{\boldsymbol{S}}_{\boldsymbol{B}} \qquad \text{Eq. 4.1.}$$

where the sum runs over all different pairs of spin centres. Note that with this definition, positive (negative) J_{AB} values correspond to FM (AFM) interactions. This model is expected to provide a suitable description of the low energy states of the materials due to the well-defined character of the magnetic centres and its independency on the spin configuration. The extraction of the value of the corresponding magnetic couplings in the present context takes advantage of the BS approach to describe the spin polarised electronic solutions to depict different spin orderings.[20-22] If the strong localisation limit of the spin mapping is considered,[23,24,] it is

Document signat digitalment per: CRISTINA RONCERO BARRERO

assumed that the diagonal form of the Heisenberg Hamiltonian (Eq. 4.1) is valid and, thus, the corresponding Ising model (Eq. 4.2) provides the suitable mapping to extract the value of the magnetic couplings between radicals from the energy differences.[25]

$$H = -2\sum_{A>B} J_{AB} S_A^z S_B^z \qquad \text{Eq. 4.2.}$$

Direct observation of the crystal packing indicates that the most relevant magnetic coupling will take place between radicals connected: (i) along either *a*- or *b*-axis (J_{ab}) since both axes are equivalent by symmetry, (ii) in diagonal (J_d) within a given *ab*-layer, and (iii) along any two π-stacked *ab*-layers (J_π) (see Figure 4.7a). Considering the energies of the spin arrangements previously reported for all four S/Se bidDTA-compounds (see Figure 4.1 and Table 4.1), the relationships between these energies and J_π (interplane), and J_{ab} and J_d (in-plane) magnetic interactions are given in Figure 4.7b (assuming $J_d = 0$). This leads to an inconsistent system of equations, which provides very different J_{AB} values depending on the set of equations used in the least square fitting procedure. This is a clear indication that other lateral and/or interplane magnetic interactions are also important and with a magnitude comparable to those three considered. In fact, not knowing exactly which radicals are interacting magnetically results in many possible different sets of J_{AB} values. We can thus conclude that a detailed analysis of the magnetic coupling between particular pairs of radicals is exceedingly decisive to understand which are the dominant magnetic couplings between A···B radicals in order to correctly describe the magnetic properties of these systems.

Based on a distance analysis of molecular contacts, Oakley and col. have suggested in a previous study of bisDTA compounds[**¡Error! Marcador no definido.**,26] that lateral interplane interactions (corresponding to J_{ac} in Figure 4.7a) can be also important to understand the magnetic properties of these systems. At a first sight, the magnitude of J_{ac} is expected to be the least

Document signat digitalment per: CRISTINA RONCERO BARRERO

important in view of distance and overlap of spin density distributions (see Figure 4.3 and Table 4.3).

(a)

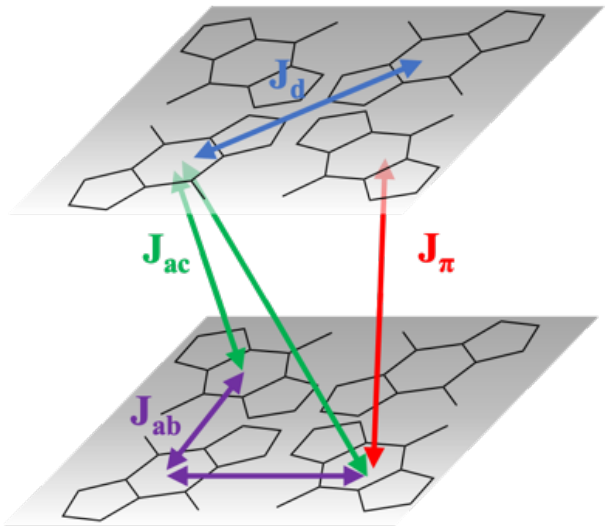

(b)

$$E_{AFM} - E_{FM} = 2J_{ab} + 2J_{ac}$$
$$E_{AFM1} - E_{FM} = J_{\pi} + 2J_{ac}$$
$$E_{AFM2} - E_{FM} = 2J_{ab} + J_{\pi}$$
$$E_{AFM3} - E_{FM} = J_{ab} + J_{d} + J_{ac}$$
$$E_{AFM4} - E_{FM} = J_{ab} + J_{d} + J_{ac} + J_{\pi}$$

Figure 4.7. (a) Schematic representation of J_{ab} , J_d (in-plane), and J_{π} , J_{ac} (interplane) magnetic interactions. (b) Relationships between energies of four different spin states to extract the aforementioned in-plane and interplane magnetic couplings. FM and AFM# are in agreement with Figure 4.1. Energies for spin states are reported in Table 4.1.

A preliminary analysis of the intermolecular distances seems to be able to provide the most relevant through space interactions in order to establish the dominant magnetic coupling constants in the materials. However, this by no means provides a simple and univocal assignation since the molecular topology and the possible contacts between neighboring radicals are complex and strongly dependent on the definition of each pair considered. In Table 4.3 we provide a set of 6 relevant contacts between A and B molecular entities forming a pair to which the J_{AB} interaction can be assigned. Direct inspection of the crystal packing hints at the obvious J_{π} interaction as the main magnetic coupling. However, this simplest assumption will be proven not to be correct, since the lateral contacts (both in plane and interplane interactions described in Figure 4.7)

Document signat digitalment per: CRISTINA RONCERO BARRERO

will be shown to play a non-negligible role. The choice of pairs of radicals that might exhibit magnetic coupling has been done in terms of distances

Table 4.3. Intermolecular distance analysis (in Å) of the studied magnetic contacts. Distances between molecular mass centroids and the shortest contacts between relevant atomic positions have been listed (see Figure 4.7 for J_{AB} notation). Distances have been measure from the crystallographic data at 100K.

System		d. cent.	$N_A\cdots N_B$	$N_A\cdots E_{1B}$	$N_A\cdots E_{2B}$	$E_{2A}\cdots E_{2B}$	$E_{2A}\cdots E_{1B}$
(S,S)	**π**	4.03	4.03	**3.53**	3.76	4.03	3.68
	d	11.17	6.54	6.53	5.19	**3.90**	5.46
	ab	8.37	5.71	**3.35**	4.24	3.49	3.52
	ac	8.00	4.67	3.53	3.48	**3.34**	4.30
(S,Se)	**π**	4.02	4.02	**3.55**	3.77	4.02	3.74
	d	11.24	6.68	6.70	5.19	**3.76**	5.51
	ab	8.43	5.83	**3.41**	4.26	**3.40**	3.61
	ac	8.04	4.76	3.56	3.47	**3.27**	4.40
(Se,S)	**π**	4.09	4.09	**3.58**	3.86	4.09	3.68
	d	11.34	6.72	6.65	5.32	**3.96**	5.52
	ab	8.13	4.81	3.65	3.63	**3.39**	4.37
	2c	8.48	5.79	**3.28**	4.35	3.55	3.45
(Se,Se)	**π**	4.13	4.13	**3.65**	3.91	4.13	3.78
	d	11.44	6.84	6.83	5.31	**3.83**	5.61
	ab	8.20	4.89	3.70	3.61	**3.36**	4.53
	ac	8.56	5.89	**3.34**	4.34	3.46	3.59

between two atoms belonging to radical A and radical B. In this case, the $N_A\cdots N_B$, $N_A\cdots E_{1B}$, $N_A\cdots E_{2B}$. $E_{2A}\cdots E_{2B}$, and $E_{2A}\cdots E_{1B}$ represent the shortest values observed in the structures. Clearly, the $N_A\cdots E_{1B}$ and $E_{2A}\cdots E_{2B}$ suggest that the set of J_{AB} parameters considered in this work are the most relevant since other possible contacts become significantly distant and the corresponding magnetic couplings are expected to be small. This shows the difficulty in assigning a univocal interaction path and an exhaustive inclusion of other pair interactions becomes cumbersome and, hence, we limit ourselves to the set of J_{AB} couplings considered.

Document signat digitalment per: CRISTINA RONCERO BARRERO

We stress that despite our preliminary assumptions, the results obtained (see Table 4.4) show that the J_{ac} interaction corresponds to the next relevant intermolecular contact and should be taken into account for

Table 4.4. Calculated values of J_{ab}, J_d, J_{ac} and J_π dominant magnetic couplings (in cm^{-1}) for all four bisDTA-derived compounds studied in this work.

System	T / K	J_{ab}	J_d	J_{ac}	J_π
(S,S)	100	1.2	–0.5	3.4	–3.0
(S,Se)	100	3.5	–1.4	7.0	4.1
(Se,S)	100	2.5	–1.1	2.4	–3.8
(Se,Se)	100	5.6	–1.0	3.6	4.1
	2	5.5	–1.0	3.7	8.2

consistency. Hence, in an attempt to find an appropriate set of J_{AB} magnetic couplings to describe the magnetic solutions considered in this work we made a last test using the J_{ab} and J_d (in-plane), and J_{ac} and J_π (interplane) magnetic interactions In this case, the J_{AB} values obtained using the least square fitting procedure with this full set of equations (reported in Table 4.4) are consistent and almost independent of the set of equations considered, being the (S,Se) system the one that shows larger deviations.

The values of the calculated magnetic couplings are consistent with the experimentally observed magnetic behaviours with some remarks: (i) dominant interactions are FM for (S,Se) and (Se,Se) although the numerical values are too small to explain the critical temperatures observed for these bulk ferromagnets; (ii) competition between J_{ab}, J_{ac} and J_π could justify the no magnetic order response of (S,S) as a complex 3D magnetic topology, and (iii) competition between J_{ab}, J_{ac} and J_π leads to a complex magnetic topology for (Se,S) dominated by the J_π coupling that may explain the antiferromagnetic behaviour upon lowering temperature. Yet the observed spin canting for (Se,S) is beyond the possibilities of the present computational approach.

Document signat digitalment per: CRISTINA RONCERO BARRERO

Notice that in-plane interactions (represented here by J_{ab} and J_d) are frustrated, which suggest that either long-range magnetic correlations or structure effects play an important role at low temperature due to the competition between J_{ab}, J_d and J_{ac} interactions. This clearly illustrates the difficulties to suggest a consistent set of couplings to be considered as potential magnetic interactions for this kind of molecular magnetic systems. To come with the right set of J_{AB}'s requires complementary information that has to be validated from different approaches in order to provide a complete description of the magnetic properties of the systems.

We conclude this Chapter by noting that to fully understand the magnetic properties of these materials it is absolutely essential to take into account both the complex magnetic topology of the systems with competing ferro- and antiferromagnetic interactions, which are not evident from direct observation of the crystal packing, and the long-range order. Evidencing thus that a bottom-up analysis using dimer clusters and ab initio calculations will be necessary to tackle the magnetic properties of these four bisDTA S/Se materials. Yet the results provided by the present periodic calculations establish valuable information on how to proceed with the modelling and rationalisation of the structure and properties of these interesting multifunctional magnetic semiconductors that are a challenging problem for present day computational modelling methods and models of electronic structure.

4.4. Conclusions

Hybrid DFT electronic band structure calculations are able nowadays to give reliable information on the ground state, electrical conductivity and magnetic properties in many different complex molecular systems. However, very few attempts have been reported dealing with multifunctional magnetic molecular materials, like bisDTA analogues

Document signat digitalment per: CRISTINA RONCERO BARRERO

studied in this work, whose unpaired electrons that are delocalised over molecular π-systems are also responsible for the electronic conductivity of the materials. This merges in a single compound two of the most difficult problems faced by current DFT methods: open-shell systems and electron localisation/delocalisation.

Relying on the overall balanced description provided by hybrid DFT functionals, and especially B3LYP for organic and organometallic magnetic systems, the calculations show that the systems behave as paramagnetic semiconductors in which the unpaired electrons reside in the π-systems of individual molecular entities. In all cases, the spin-unrestricted magnetic solutions have energies well below the closed-shell solutions. Nevertheless, the small energy difference of *ca.* 250 meV per chemical formula unit suggests that the electronic conduction properties will have contributions from band and hopping mechanisms. This fact thus precludes a simple rationalisation using a rigid band model.

The density of states clearly shows that the systems behave as narrow band (0.2-0.3 eV dispersion) open-shell semiconductors with 1.15-1.40-eV indirect gap separating valence and conduction bands. The bands defining the gap arise mainly from the π-orbitals of the N-E_2-E_1 sitting on the outer rings of the molecular entities, with minor participation of other atoms. This is a clear indication that the properties of these systems are dominated by the nature of the atoms in these positions. The relative magnitude of the calculated gaps is in line with the observed conductivity properties of the systems but a more complete analysis beyond the rigid band model is required to understand the different behaviour of the (Se,S) and (S,Se) systems.

The charge and spin distributions are almost independent of the magnetic solution and describe the systems as formed by neutral paramagnetic molecular entities with one unpaired electron per molecular

Document signat digitalment per: CRISTINA RONCERO BARRERO

entity. From the analysis of charge distribution, the observed E_1-E_2-N charge alternation provides an explanation for the tilting and slippage of the molecular units along the *c*-axis that avoids perfectly eclipsed radicals along the π-stacking by displacing the negatively charged N atom towards the centre of the ring and closer to the E_2 position of a nearby molecule to optimise attractive/repulsive interactions.

Regarding the spin distribution of the systems, each radical can be considered as a local S = ½ effective spin particle and the magnetic properties of the systems can be described by means of a two-body HDVV spin Hamiltonian with isotropic interactions between localised magnetic moments representing each radical. The calculated ground state for each system is consistent with the experimentally observed magnetic behaviour, although for (S,Se) compound additional effects may take place at lower temperatures. Additionally, a detailed analysis of the magnetic coupling interactions clearly indicates that the systems have intricate magnetic topologies in which lateral ferromagnetic interactions are of the same order than J_π along the π-stacking direction. This fact is at odds with the common assumption that the J_{AB} couplings along the π-stack are usually the dominant interactions. Even though the magnetic parameters considered in the mapping procedure provide a consistent description of the electronic solutions here obtained, Chapter 5 will provide a detailed investigation of all the magnetic interactions required to univocally establish which are the most significant couplings to rationalise the magnetic properties of the systems.

4.5. References

1 C. M. Robertson, A. A. Leitch, K. Cvrkalj, R. W. Reed, D. J. T. Myles, P. A. Dube and R. T. Oakley, "Enhanced conductivity and magnetic ordering in isostructural heavy atom radicals," J. Am. Chem. Soc., 2008, 130, 8414–8425.

Document signat digitalment per: CRISTINA RONCERO BARRERO

2 C. M. Robertson, S. M. Winter, J. A. K. Howard, M. R. Probert, and R. T. Oakley, “Low temperature insights into the crystal and magnetic structure of a neutral radical ferromagnet”, Chem. Comm., 2021, 57(79), 10238-10241

3 K. Lekin, A. A. Leitch, A. Assoud, W. Yong, J. Desmarais, J. S. Tse, S. Desgreniers, R. A. Secco, R. T. Oakley, "Benzoquinone-Bridged Heterocyclic Zwitterions as Building Blocks for Molecular Semiconductors and Metals”, Inorg. Chem., 2018, 57, 4757–4770.

4 L. Beer, J. L. Brusso, A. W. Cordes, R. C. Haddon, M. E. Itkis, K. Kirschbaum, D. S. MacGregor, R. T. Oakley, A. A. Pinkerton, R. W. Reed, "Resonance-Stabilized 1,2,3-Dithiazolo-1,2,3-dithiazolyls as Neutral π-Radical Conductors", J. Am. Chem. Soc., 2002, 124, 9498-9509.

5 L. Beer, J.F. Britten, J.L. Brusso, A.W. Cordes, R.C. Haddon, M.E. Itkis, D. S. MacGregor, R.T. Oakley, R.W. Reed, C.M. Robertson, "Prototypal Dithiazolodithiazolyl Radicals: Synthesis, Structures, and Transport Properties", J. Am. Chem. Soc., 2003, 125, 14394-14403.

6 A. Mailman, S. M. Winter, X. Yu, C. M. Robertson, W. Yong, J. S. Tse, R. A. Secco, Z. Liu, P. A. Dube, J. A. K. Howard, R. T. Oakley, "Crossing the Insulator-to-Metal Barrier with a Thiazyl Radical Conductor", J. Am. Chem. Soc. 2012, 134, 9886−9889.

7 X. Yu, A. Mailman, K. Lekin, A. Assoud, C. M. Robertson, B.C. Noll, C. F. Campana, J. A. K. Howard, P.A. Dube, R.T. Oakley, "Semiquinone-Bridged Bisdithiazolyl Radicals as Neutral Radical Conductors", J. Am. Chem. Soc. 2012, 134, 2264−2275.

8 A. A. Leitch, K. Lekin, S. M. Winter, L. E. Downie, H. Tsuruda, J. S. Tse, M. Mito, S. Desgreniers, P. A. Dube, S. Zhang, Q. Liu, C. Jin, Y. Ohishi, R. T. Oakley, "From Magnets to Metals: The Response of Tetragonal Bisdiselenazolyl Radicals to Pressure", J. Am. Chem. Soc. 2011, 133, 6051–6060.

9 T. Kubo, A. Shimizu, M. Sakamoto, M. Uruichi, K. Yakushi, M. Nakano, D. Shiomi, K. Sato, T. Takui, Y. Morita, K. Nakasuji, "Synthesis, Intermolecular Interaction, and Semiconductive Behavior of a Delocalized Singlet Biradical Hydrocarbon", *Angew. Chem. Int. Ed.* 2005, **44**, 6564-6568.

10 J.W. L. Wong, A. Mailman, K. Lekin, S. M. Winter, W. Yong, J. Zhao, S. V. Garimella, J. S. Tse, R. A. Secco, S. Desgreniers, Y. Ohishi, F. Borondics, R. T. Oakley, "Pressure Induced Phase Transitions and Metallization of a Neutral Radical Conductor", J. Am. Chem. Soc. 2014, 136, 1070−1081.

11 A. Mailman, J. W. L. Wong, S. M. Winter, R. C. M. Claridge, C. M. Robertson, A. Assoud, W. Yong, E. Steven, P. A. Dube, J. S. Tse, S. Desgreniers, R. A. Secco, R. T. Oakley, "Fine Tuning the Performance of Multiorbital Radical Conductors by Substituent Effects", J. Am. Chem. Soc. 2017, 139, 1625−1635

Document signat digitalment per: CRISTINA RONCERO BARRERO

12 A. Mailman, A. A. Leitch, W. Yong, E. Steven, S. M. Winter, R. C. M. Claridge, A. Assoud, J. S. Tse, S. Desgreniers, R. A. Secco, R. T. Oakley, "The Power of Packing: Metallization of an Organic Semiconductor", J. Am. Chem. Soc. 2017, 139, 2180−2183.

13 A. Mailman, C. M. Robertson, S. M. Winter, P. A. Dube, and R. T. Oakley, "The Importance of Electronic Dimensionality in Multiorbital Radical Conductors," Inorg. Chem., 2019, 58, 6495–6506.

14 J. Huang, M. Kertesz, "One-Dimensional Metallic Conducting Pathway of Cyclohexyl-Substituted Spiro-Biphenalenyl Neutral Radical Molecular Crystal", *J. Am. Chem. Soc.* 2006, **128**, 1418-1419.

15 N. Tenn, N. Bellec, O. Jeannin, L. Piekara-Sady, P. Auban-Senzier, J. Íñiguez, E. Canadell, D. Lorcy, "A Single-Component Molecular Metal Based on a Thiazole Dithiolate Gold Complex", *J. Am. Chem. Soc.* 2009, **131**, 16961–16967.

16 G. Yzambart, N. Bellec, G. Nasser, O. Jeannin, T. Roisnel, M. Fourmigué, P. Auban-Senzier, J. Íñiguez, E. Canadell, D. Lorcy , "Anisotropic Chemical Pressure Effects in Single-Component Molecular Metals Based on Radical Dithiolene and Diselenolene Gold Complexes", *J. Am. Chem. Soc.* 2012, **134**, 17138−17148.

17 T. Kushida, S. Shirai, N. Ando, T. Okamoto, H. Ishii, H. Matsui, M. Yamagishi, T. Uemura, J. Tsurumi, S. Watanabe, J. Takeya, S. Yamaguchi, "Boron-Stabilized Planar Neutral π-Radicals with Well-Balanced Ambipolar Charge-Transport Properties", *J. Am. Chem. Soc.* 2017, **139**, 14336-14339.

18 Y. Le Gal, T. Roisnel, P. Auban-Senzier, N. Bellec, J. Íñiguez, E. Canadell, D. Lorcy, "Stable Metallic State of a Neutral-Radical Single-Component Conductor at Ambient Pressure", *J. Am. Chem. Soc.* 2018, **140**, 6998−7004.

19 Y. Kobayashi, K. Hirata, S. N. Hood, H. Yang, A. Walsh, Y. Matsushita, K. Ishioka, "Crystal structure and metallization mechanism of the π-radical metal TED", *Chem. Sci.* 2020, **11**, 11699-11704.

20 L. Noodleman, *J. Chem. Phys.* 1981, **74**, 5737–5743.

21 L. Noodleman and E. R. Davidson, , *Chem. Phys.* 1986, **109**, 131–143.

22 R. Caballol, O. Castell, F. Illas, I. de P. R. Moreira, and J. P. Malrieu, *J. Phys. Chem. A*, 1997, **101**, 7860–7866.

23 Moreira, I. D. P. R., & Illas, F. "A unified view of the theoretical description of magnetic coupling in molecular chemistry and solid state physics. *Phys. Chem. Chem. Phys.,* 2006, **8**, 14, 1645–1659.

24 I. de P. R. Moreira, C. J. Calzado, J-P. Malrieu, F. Illas, *New J. Phys.* 2007, **9**, 369.

Document signat digitalment per: CRISTINA RONCERO BARRERO

25 P. Rivero, I. de P. R. Moreira, F. Illas. " Spin Hamiltonian effective parameters from periodic electronic structure calculations". J. Phys.: Conf. Series 2008, 117, 012025.

26 C. M. Robertson, D. J. T. Myles, A. A. Leitch, r. W. Reed, B. M. Dooley, N. L. Frank, P. A. Dube, l. K. Thompson and R. T. Oakley, "Ferromagnetism in a heavy atom heterocyclic radical conductor," *J. Am. Chem. Soc.*, 2007, **129**, 12688-12689.

Document signat digitalment per: CRISTINA RONCERO BARRERO

Chapter 5. Disentangling The Magnetic Exchange Network in bisDTA Materials

In previous Chapter 4, the electronic structure of the system was characterized using UDFT-BS periodic calculations. Results showed that all four bisDTA S/Se materials are paramagnetic semiconductors formed by neutral molecular entities that can be considered as local S=1/2 spin moieties with a magnetic ordering consistent with the observed experimental properties at low temperature. Based in previous reported studies[1,2] and a preliminary distance-based analysis, , we proposed a set of relevant J_{AB} magnetic interactions between A···B pairs of radicals to describe low energy magnetic solutions. The different sets of resultant exchange couplings were consistent with distinct feasible intricate magnetic topologies. This fact indicated that the complete identification of all the relevant interactions for all four bisDTA S/Se systems is beyond the periodic model. A more in-depth study, with a complete cluster evaluation of all relevant J_{AB} magnetic interactions between A···B pairs of radicals in the structure, was thus proved to be required for the identification of all the magnetic interactions in order to rationalize the magnetism of these materials.

In this chapter, the dominant magnetic interactions of the four bisDTA materials and the effect of the S/Se substitution on their macroscopic magnetic response are analysed following a first principles bottom-up working strategy (FPBU). In periodic calculations, the set of computed J_{AB} was limited by the size of the supercell since just the spin orientation of the explicit atoms could be modified, and by the convergence of the BS calculations with intermediate S_z values (i.e.: $0 < S_z < N/2$ being N the number of magnetic centres in the supercell), which failed when evaluating some spin solutions with a spin arrangement showing large spin polarization and symmetry breaking of the

Document signat digitalment per: CRISTINA RONCERO BARRERO

supercell. Using a cluster model, we can perform a more in-depth analysis of all the possible magnetic contacts between A···B radicals within the crystal.

Reported experimental studies[1,2] show that J_{AB} interactions along the π-stacking direction in bisDTA systems are significantly affected by small distortions of the crystal packing. Those studies aimed at explaining the observed differences on conductivity and magnetic properties arising from variations in the central ring substituents. However, in order to clarify the magnetic behaviour of the different systems at low and room temperatures it will be shown that those small structural changes may also explain the differences among the four compounds at the electronic level. Following a systematic working procedure, we have evaluated the relevant J_{AB} magnetic exchange couplings between radical pairs using the available X-ray data of each crystal at 100 K[3], and compared to those J_{AB} calculated using optimised X-ray crystal structures at 0K, by means of first-principles calculations. It must be stressed that crystal optimisations will allow us to explain the FM reported behaviour in (S,Se) and (Se,Se) at low temperature proving to be an alternative when experimental crystallographic data below the critical magnetic temperature, T_C, are not available. Yet, in order to have the entire picture of magnetic and conducting properties of these materials at the electronic level upon changes on temperature, it is also relevant to have structural information at temperatures above the T_C[4]. Our results show that, in molecule-based materials whose magnetism is highly affected by structural changes, availability of crystallographic data at temperatures close to T_C is crucial in order to understand the key microscopic contributions responsible for the physical properties of technological interest under study.

5.1. Analysis of X-Ray data reported at 100 K

The four selected bisDTA-derived compounds exhibit a completely different magnetism depending on the S/Se substitution in E_1 and E_2 positions. Let us remind here that (S,S) shows no magnetic order at low temperatures and (Se,S)

Document signat digitalment per: CRISTINA RONCERO BARRERO

as a spin canted antiferromagnet, while (S,Se) and (Se,Se) behave as bulk ferromagnets (see Figure 2.1). Therefore, the magnetic response is clearly dependent on the S/Se position on the bisDTA-radical as well as on the distance between them in adjacent radicals. Besides distance, other structural effects (*e.g.* latitudinal and longitudinal slippages) that have subtle implications on the properties also have to be analysed in order to understand the observed variability in the magnetic behaviour of the systems. The analysis of both the singly occupied molecular orbital (SOMO) and the spin density of the monomer to understand which are the relevant distances and, thus, the interactions that have to be considered shows that the unpaired electron is delocalised over the DTA fused rings (see Figure 5.1 for SOMO and spin density of the bisDTA S/Se radicals). In all systems, the SOMO of the molecular radical consists of a π-orbital, which is composed by the p-atomic orbitals of the two thiazyl groups with both E_2 and E_1 positions contributing to the orbital almost equally. Analysis of the spin density shows a negatively charged region centred on the two thiazyl groups. Therefore, both spin densities and SOMOs are consistent with those obtained using periodic calculations.

The evaluation of J_{AB} exchange couplings will reveal that, although all four materials are isostructural, the subtle differences in their electronic structure and relative crystal packing will lead to very different values of J_{AB} magnetic interactions between pairs of radicals and, in turn, distinct macroscopic magnetic behaviour (see inset in Figure 2.1). Taking pure bisdithiazolyl (S,S) as reference, a general trend along the series is observed with Se incorporation. While (S,S) material behaves as a paramagnet without long-range magnetic order observed at low temperature, incorporation of Se enhances the magnetic interactions, regardless of the sign, leading to different magnetic orderings. For E_2-substituted thiaselenazolyl (S,Se) and bisdiselenazolyl (Se,Se) materials, bulk ferromagnetic ordering is observed below 12.8 K and 17.0 K, respectively. In contrast, when the heavier heteroatom is in the E_1 position, the resultant thiaselenazolyl (Se,S) material exhibits a spin canted antiferromagnetic response below 14.0 K.

Document signat digitalment per: CRISTINA RONCERO BARRERO

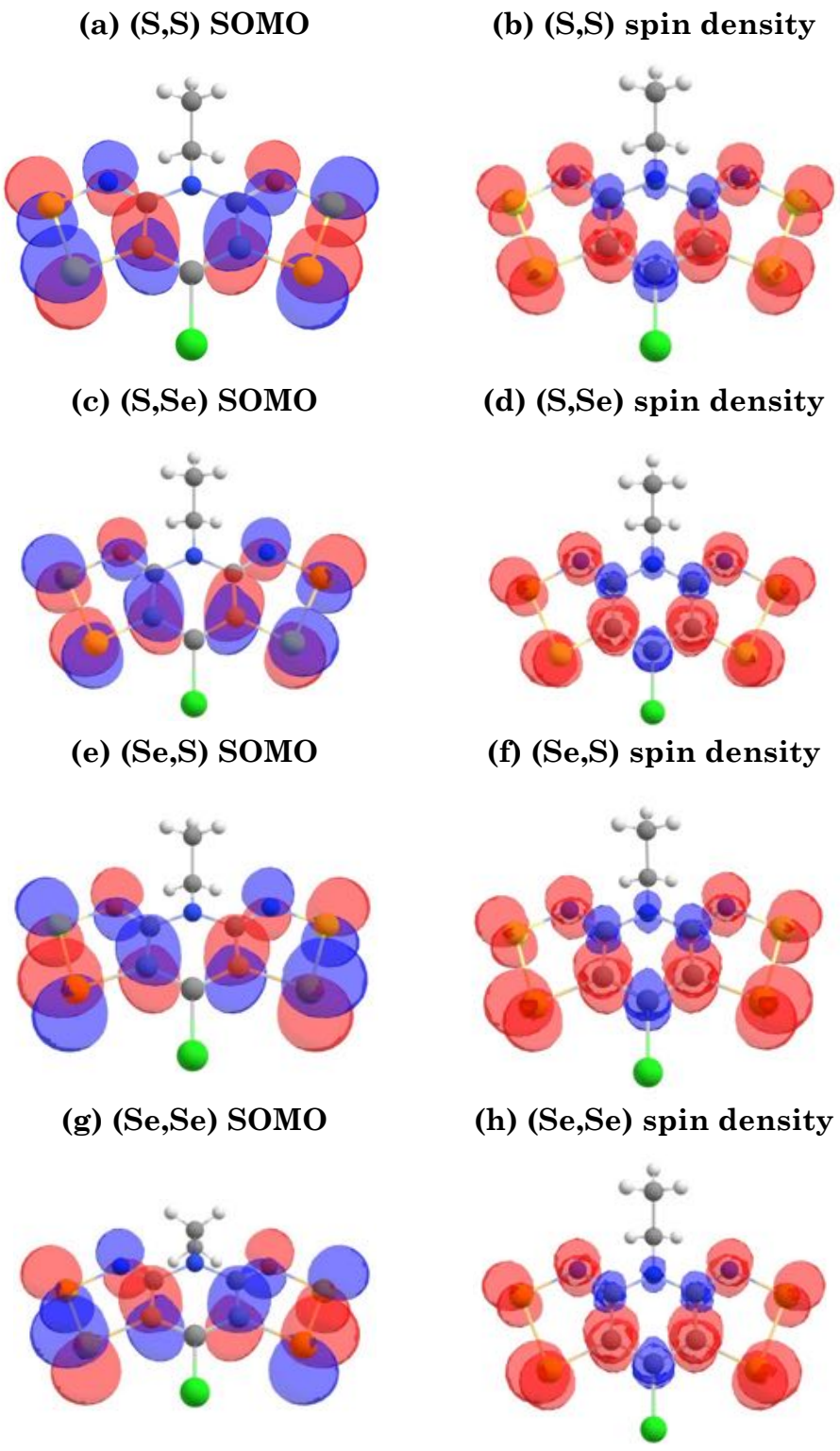

Figure 5.1. SOMO (left column) and spin density (right column) of the four S/Se bisDTA monomers calculated at UB3LYP/6-311+G(d,p) level. Positive and negative contributions are represented with red and blue colours, respectively (0.002 a.u. isosurface).

Document signat digitalment per: CRISTINA RONCERO BARRERO

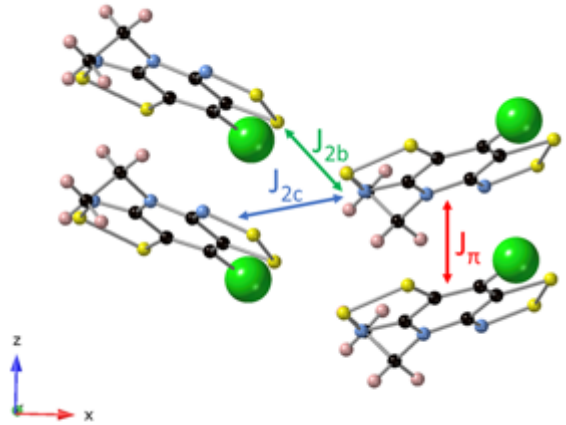

Figure 5.2. Schematic representation of the three relevant J_{AB} magnetic interactions that contribute to the macroscopic magnetism in all four bisDTA compounds. Note that J_{2b}, J_{2c} couplings lie on *ab*-plane and J_{π} coupling runs along *c*-axis.

After an exhaustive assessment of which pairs of radicals have to be considered to evaluate the magnetically relevant couplings between bisDTA radicals at 100 K, our analysis concluded that 13 pairs may contribute to the overall magnetism of each one of these four compounds (see Chapter 3 Section 3.3.1 for details regarding the dimer selection). However, after evaluation of J_{AB}, only 3 radical pairs have been found to contribute to the magnetism of the title 4 compounds (see Table 5.1 for the resultant non-negligible J_{AB} exchange interactions, and Figure 5.2 for a schematic representation).

According to our calculations, the four materials present FM interactions on the *ab*-plane (see J_{2b} and J_{2c} in Table 5.1), ranging from +1.5 cm^{-1} (Se,S) to +7.2 cm^{-1} (S,Se). In contrast, when non negligible, the exchange coupling along the π-stack is AFM (see J_{π} in Table 5.1): -5.6 cm^{-1} for (S,S), -12.4 cm^{-1} for (Se,S), and -7.4 cm^{-1} for (Se,Se). The negative sign of the π-stack interaction (-12.4 cm^{-1}) could be consistent with the expected AFM behaviour in (Se,S). Regarding (S,S), experimentalists suggested that the paramagnetism observed could be due to competing AFM and FM interactions, which are actually encountered in the 100K crystal structure (-5.6 cm^{-1} along π-stack and -3.8 cm^{-1} along *a*- and *b*-axes). However, bulk ferromagnetism of (Se,Se) is incompatible with the measured AFM interaction along the π-stacking (-7.4 cm^{-1}). Same conclusion applies to

Document signat digitalment per: CRISTINA RONCERO BARRERO

Table 5.1. Exchange couplings (in cm^{-1}) computed at UB3LYP/6-311+G(d,p) level using the X-ray crystallographic data at 100 K (J_{AB}) and optimised crystal data at 0 K (J_{AB} 0K). $E_2\cdots E_2$ and shortest $E_2\cdots E_1$ distances (in Å) between radicals are given. Also crystal orientation of all three radical pairs within the crystal is given (notice that *a*- and *b*-axes are equivalent due to $P\bar{4}2_1m$ symmetry).

System	Radical pair	orientation	Dist ($E_2\cdots E_2$) /Å	Dist ($E_2\cdots E_1$) /Å	J_{AB} /cm^{-1}
(S,S)	J_π	*c*-axis (π-stacking)	4.03	3.68	-5.6
	J_{2b}	ac(=bc)-plane	3.49	3.52	<0.1
	J_{2c}	*a(=b)*-axis	3.34	4.30	+3.8
(S,Se)	J_π	*c*-axis (π-stacking)	4.02	3.74	+0.3
	J_{2b}	ac(=bc)-plane	3.40	3.61	+0.4
	J_{2c}	*a(=b)*-axis	3.27	4.40	+7.2
(Se,S)	J_π	*c*-axis (π-stacking)	4.09	3.68	-12.4
	J_{2b}	ac(=bc)-plane	3.54	3.45	+1.5
	J_{2c}	*a(=b)*-axis	3.40	4.37	+3.4
(Se,Se)	J_π	*c*-axis (π-stacking)	4.13	3.78	-7.4
	J_{2b}	ac(=bc)-plane	3.46	3.58	+0.1
	J_{2c}	*a(=b)*-axis	3.36	4.53	+5.6

(S,Se): bulk ferromagnetism is not in agreement with calculated J_{AB} couplings defining a 2D magnetic topology (+7.2 cm^{-1} along *a*- and *b*-axes).

5.1.1 Periodic versus Cluster models for J_{AB} magnetic exchange evaluation

Overall, the non-negligible magnetic interactions characterized using dimer clusters were the same than those proposed in the periodic model. However, both analyses present important differences with respect to the sign and magnitude of some interactions. In order to properly compare the results obtained let us first analyse the differences between the nomenclature used in both models.

In the cluster model, the central N atom of the pyridine ring is regarded as a magnetic site identifier and the *ab*-planes are defined with respect to the position of this central N atom (see topological planes in green in Figure 5.3). On the other hand, in Chapter 4, the in-plane interactions were assigned to the

Document signat digitalment per: CRISTINA RONCERO BARRERO

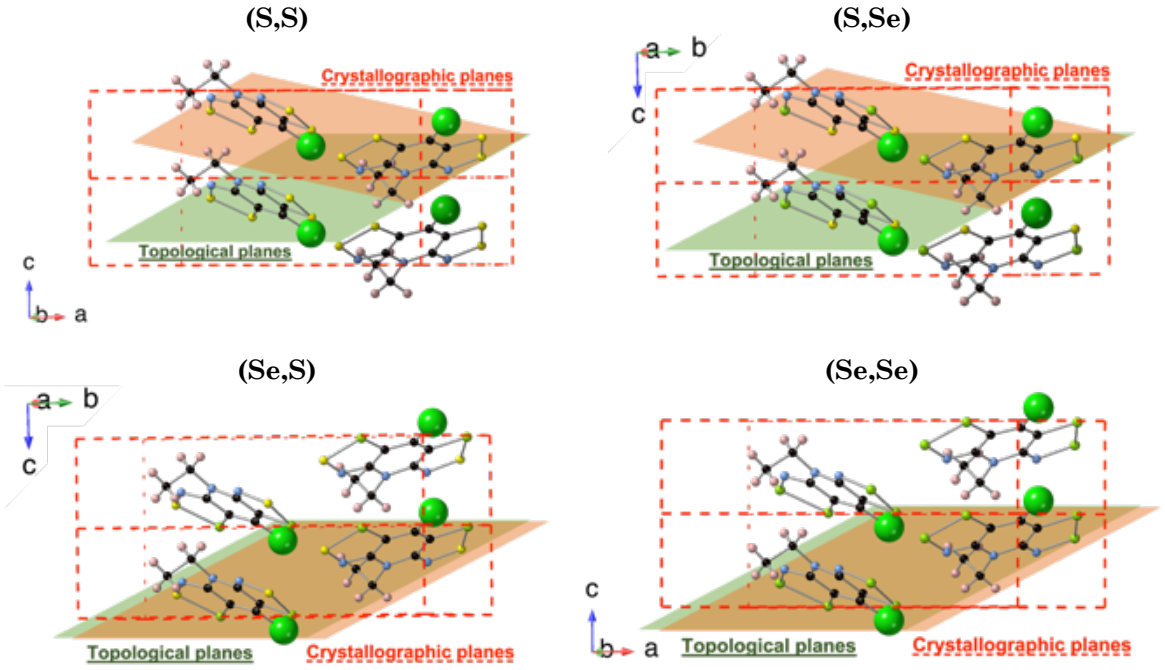

Figure 5.3. Representation of the named *ab* "crystallographic" (in orange) and "topological" (in green) planes based in the criterion used in periodic and cluster analysis, respectively.

Table 5.2. Comparison between the magnetic exchange couplings J_{AB} obtained using the cluster and periodic models. Note that the nomenclature used is the one employed in the cluster evaluation. (see Chapter 3 Section 3.3.1 for further details about the employed terminology)

System	model	J_{π}	J_{3b}	J_{2b}	J_{2c}
(S,S)	cluster	-5.6	-0.4	<0.1	+3.8
	periodic	-3.0	-0.5	+1.2	+3.4
(S,Se)	cluster	+0.3	-0.6	+0.4	+7.2
	periodic	+4.1	-1.4	+2.5	+7.0
(Se,S)	cluster	-12.4	-0.3	+1.5	+3.4
	periodic	- 3.8	-1.1	+2.4	+2.5
(Se,Se)	cluster	-7.4	-0.6	+0.1	+5.6
	periodic	+4.1	-1.0	+3.6	+5.6

adjacent dimers belonging to the same unit cell (see crystallographic planes in orange in Figure 5.3). These differences do not affect the calculations but are important when comparing both results since, as can be observed in Figure 5.3, the mapping of J_{AB} exchange couplings between cluster and periodic models depends on the S/Se bisDTA system (see Table 5.2 for comparison between both sets of J_{AB}). Specifically, the extracted J_{AB} from cluster and periodic models are

Document signat digitalment per: CRISTINA RONCERO BARRERO

the same for (Se,S) and (Se,Se) since both topological and crystallographic planes match. Contrarily, the mapping is different for (S,S) and (S,Se), although the resulting classification of J_{AB} in terms of topological and crystallographic planes is common for both materials.

Results obtained with both models present significant differences regarding (i) the value (e.g. J_{II} ranges from -12.4 cm^{-1} to -3.8 cm^{-1} for (Se,S) and from +0.3 cm^{-1} to +4.1 cm^{-1} for (S,Se) using cluster and periodic models, respectively), and (ii) the sign (e.g. J_{II} ranges from -7.4 cm^{-1} using a cluster model to +4.1 cm^{-1} using a periodic analysis for (Se,Se)) of the interaction. The small differences could be attributed to large polarization in the pair models, even though spin density distribution and SOMO obtained using both models are comparable (see Figure 5.4). However, there is a plethora of small magnetic interactions that can be individually evaluated using a cluster model, but cannot be properly assessed using the periodic approach. The reason being that the periodic model requires putting forward a guess of allegedly non-negligible J_{AB} interactions, which are selected as a function of distances between radicals. Since there are many different possibilities of assigning J_{AB} coupling to a given radical pair, if the guess is not correct, the set of equations used to extract the value of J_{AB}'s will be inconsistent and, in turn, will lead to meaningless (or, at its best, less accurate) magnetic coupling values.

The magnetic topology defined by J_{AB} calculated using dimer cluster models with the X-Ray crystallographic data at 100 K and the cluster J_{AB} (listed in Table 5.1) for bisdithiazolyl (S,S) and bisdiselenazolyl (Se,Se) consists of AFM chains (in red, running along the *c*-axis) connected into a 3D network by FM interactions along the *a*- and *b*-axes (in blue) (see Figure 5.5a,d). The similarity between magnetic topologies could be explained by the fact that both materials present the same heavy heteroatom (either S or Se) in both E_1 and E_2 positions and, despite the larger distances due to the larger atomic radius of Se, the interactions are

Document signat digitalment per: CRISTINA RONCERO BARRERO

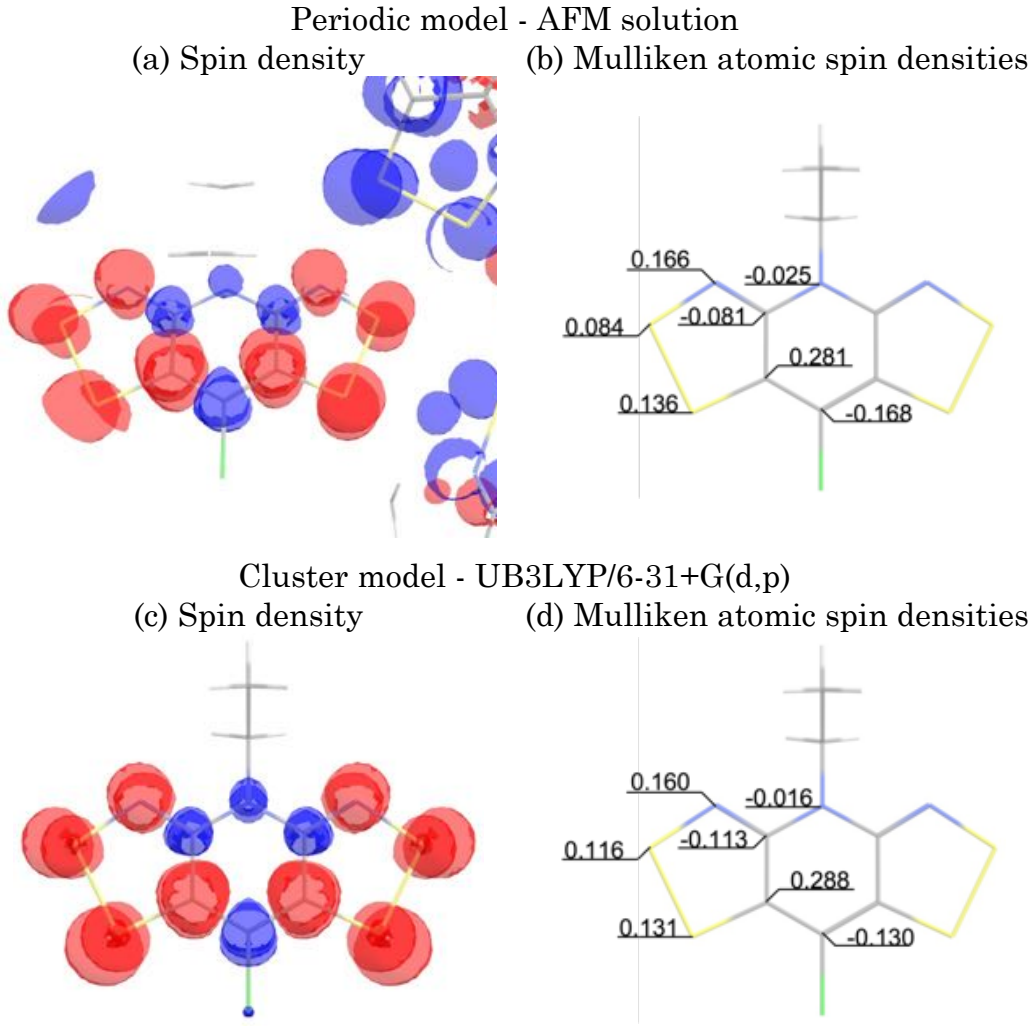

Figure 5.4. Spin density distribution (a, c) and Mulliken atomic spin densities (b, d) in electrons for the (S,S) radical monomer using (a, b) the AFM solution from the periodic model, and (c, d) the isolated monomer cluster at UB3LYP/6-31+G(d,p) level. Colour code: Alpha and beta spin densities in blue and red, respectively (0.002 a.u. isosurface).

equivalent in both systems. Strikingly, the close similarity of the resulting magnetic topologies together with the AFM nature of J_{II} cannot possibly explain the lack of long-range magnetic order of (S,S) and the bulk ferromagnetism of (Se,Se) at the same time.

Analyses of the results for the two mixed thiaselenazolyl (S,Se) and (Se,S) systems show that the position of the Se atoms affects substantially the value of the interactions in the radical pair. The (S,Se) magnetic topology consists of almost isolated 2D FM *ab*-planes (see Figure 5.5b), which would fail at explaining

Document signat digitalment per: CRISTINA RONCERO BARRERO

(a) **(S,S)**

$E_2\cdots E_2$ distance /Å	J_{AB} /cm^{-1}
4.03	-5.6
3.34	3.8

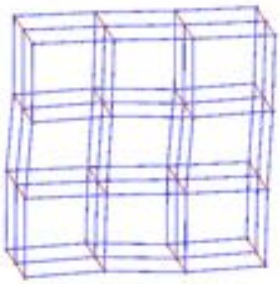

(b) **(S,Se)**

$E_2\cdots E_2$ distance /Å	J_{AB} /cm^{-1}
3.27	7.2

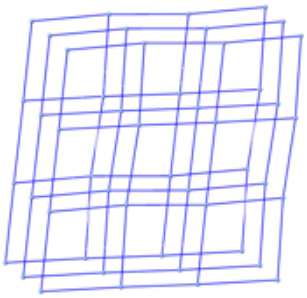

(c) **(Se,S)**

$E_2\cdots E_2$ distance /Å	J_{AB} /cm^{-1}
4.09	-12.4
3.40	3.4
3.54	1.5

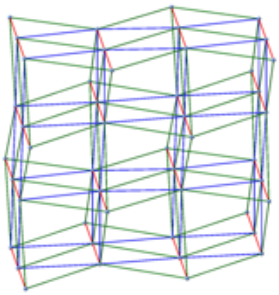

(d) **(Se,Se)**

$E_2\cdots E_2$ distance /Å	J_{AB} /cm^{-1}
4.13	-7.4
3.36	5.6

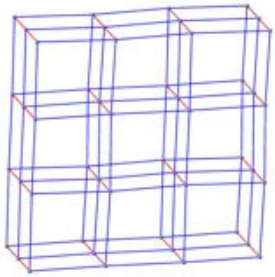

Figure 5.5. Magnetic topology and significant J_{AB} exchange interactions using 100 K X-Ray structures between radicals for (a) (S,S) , (b) (S, Se) , (c) (Se,S) , and (d) (Se,Se) compounds. Note that $E_2\cdots E_2$ distances are extracted from Table 5.1. Colour code (according to Figure 4): red = π-stack magnetic coupling along *c*-axis; blue and green = in-plane magnetic couplings.

the bulk ferromagnetism of this material. In contrast, the (Se,S) magnetic topology consists of AFM chains along the π-stack (in red) which are then coupled into a 3D network by two non-equivalent weaker set of FM interactions (in blue and green) (see Figure 5.5c). Note that the (Se,S) system presents the most intricate magnetic topology and the largest AFM coupling along the π-stack. In fact, the competition between AFM and FM exchange interactions might be the reason for (Se,S) to experimentally behave as a spin-canted antiferromagnet.[1]

The next step in order to compute the macroscopic magnetic properties, once the magnetic topology has been characterized, is to identify the smallest number of radicals that will be able to represent all the J_{AB} interactions in the same ration as they appear in the magnetic topology. This will provide a cluster representation of the infinite magnetic topology, *aka* the *minimal magnetic model*.

Document signat digitalment per: CRISTINA RONCERO BARRERO

5.1.2 Minimal magnetic models

Due to restrictions on the size of the magnetic model, two magnetic models containing 16 radical centres and accounting for the most important magnetic interactions have been chosen to explore the magnetic response of (S,S), (Se,S) and (Se,Se) (namely, magnetic susceptibility as a function of temperature, $\chi(T)$). The magnetic topology of these three bisDTA compounds at 100K is 3D, and the magnetic models have been selected to consider (i) the importance of the π-stacking interaction by elongating the unit cell along the *c*-axis, and (ii) the cooperativity of the magnetic interactions along the *ab*-plane by extending the model along the *a*-axis (which is equivalent to the *b*-axis) (see Figure 5.6). In order to account for both effects (c-axis and ab-plane interactions), the calculated $\chi T(T)$ data from magnetic models (i) and (ii) has been averaged with the aim to provide results for a resultant virtual "64-radical" model (see a representation of the three models in Figure 5.6). For (S,Se) at 100 K, a 2D magnetic model was used instead since the magnetic topology was found to be 2D (see Figure 5.7).

To sum up, before calculating the macroscopic magnetic properties of these four bisDTA S/Se materials, we can anticipate that, using the X-Ray data reported at 100 K, the magnetic topology of (S,S) and (Se,S) might explain the experimental measurements (see Figure 5.5a,c). However, the magnitude of the FM interactions in compounds (S,Se) and (Se,Se) is believed to be too small to explain their experimentally observed bulk ferromagnetism (see Figure 5.5b,d), as will be next corroborated by the simulation of their $\chi T(T)$ magnetic susceptibility data.

Results show that, as was anticipated, both (S,S) and (Se,S) computed $\chi T(T)$ magnetic susceptibilities obtained using the X-Ray crystallographic structures characterised at 100 K reproduce the experimental $\chi T(T)$ values (see Figure 5.8). One can easily realise that the simulation for (Se,S) accurately mimics the whole experimental curve, while data for (S,S) slightly deviates when cooling down

Document signat digitalment per: CRISTINA RONCERO BARRERO

from 60 K. On the other hand, results for E_2 Se-substituted materials fail completely at reproducing the experimental data (Figure 5.8).

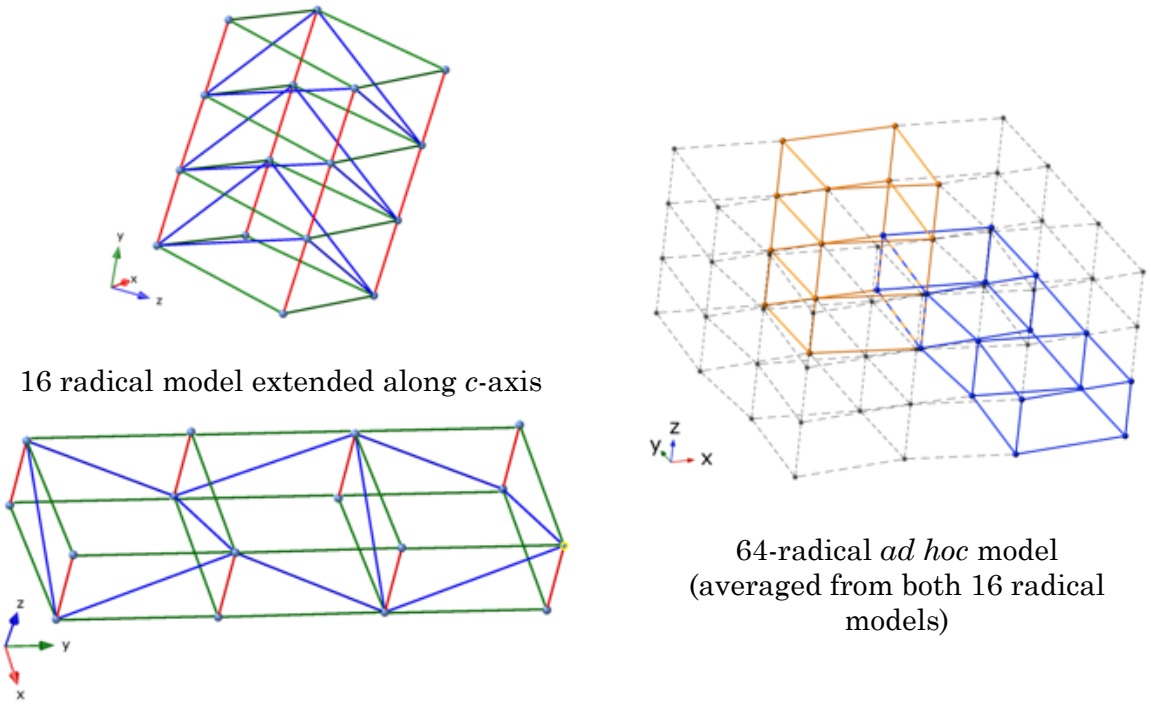

16 radical model extended along *c*-axis

64-radical *ad hoc* model (averaged from both 16 radical models)

16 radical model extended along *a*-axis (equivalent to *b*-axis)

Figure 5.6 Magnetic models used to describe (S,S), (Se,S) and (Se,Se) at 100 and 0 K, and (S,Se) at 0 K.

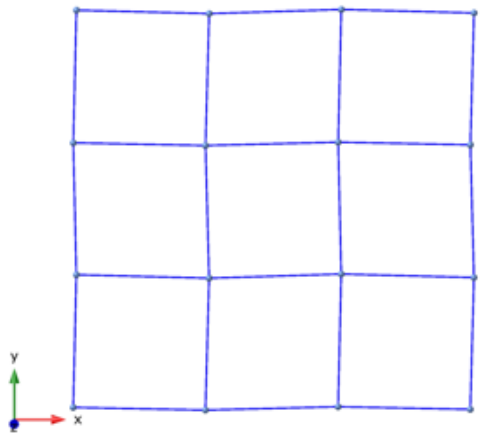

Figure 5.7 Magnetic model of (S,Se) at 100K

Document signat digitalment per: CRISTINA RONCERO BARRERO

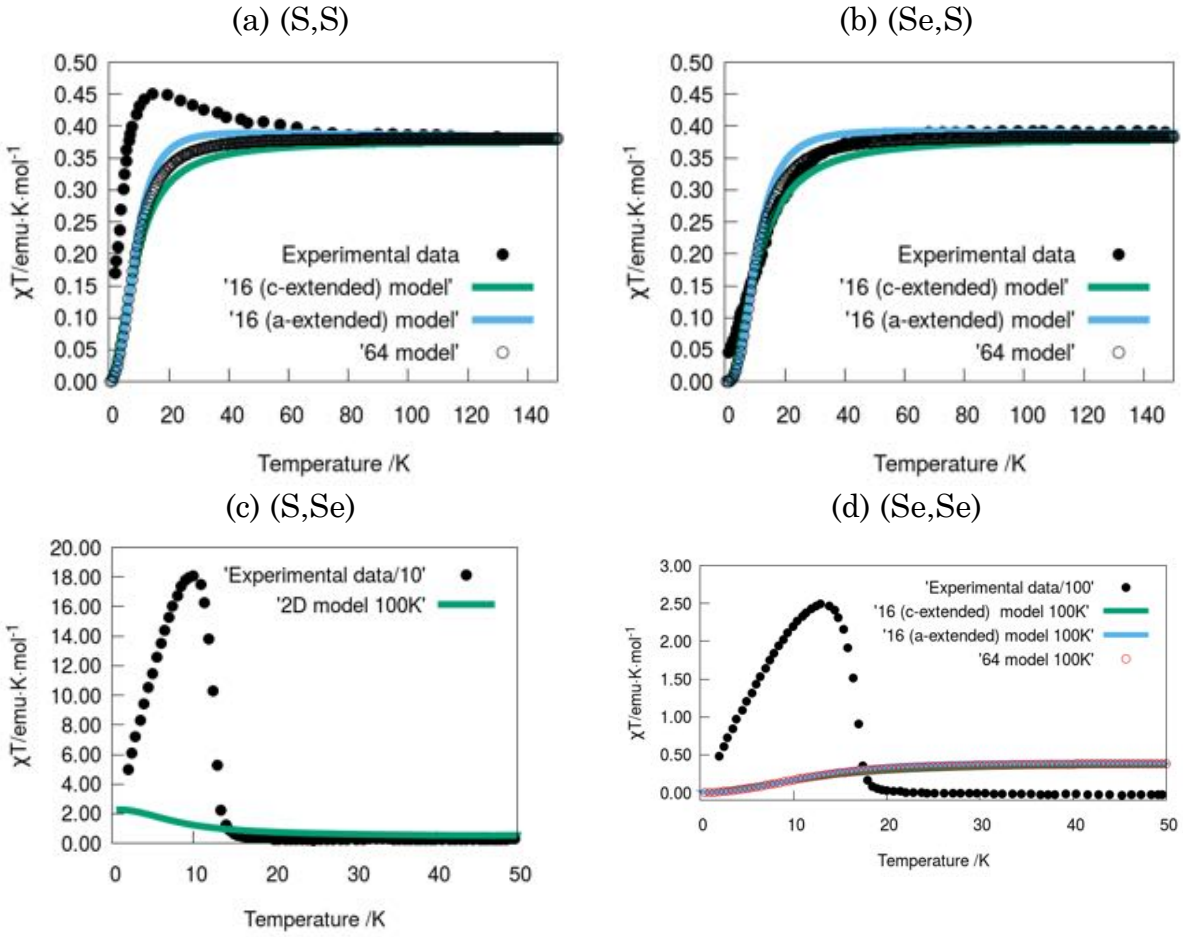

Figure 5.8. Comparison between calculated and experimental magnetic susceptibility χT(T) calculated using J_{AB}(X-Ray data at 100 K) for (a) bisdithiazolyl (S,S), (b) thiaselenazolyl (S,Se) and (c) (Se,S) and (d) bisdiselenazolyl (Se,Se). Magnetic models have been represented in Figure 5.6 and 5.7.

Although our calculated J_{AB}'s are within the range of values reported for this kind of radicals,[1] the simulated χT(T) data cannot possibly result in the experimentally observed large values for (S,Se) and (Se,Se) whose maximum χT value reaches *ca.* 200 emu·K·mol^{-1} at *ca.* 10K for (S,Se) and *ca.* 15K for (Se,Se).[3] In addition, the spin multiplicity of the ground state for (Se,Se) is found to be a singlet (*i.e.* $<S^2>=0$), which is incompatible with a bulk ferromagnetic material. Previous studies,[2] meant to explain the differences between analogous materials with different substituents, have shown that magnetism on these systems is highly sensitive to small geometry variations. Small changes due to differences in crystal packing (e.g., caused by the steric hindrance effect of the substituents) result in important changes on the exhibited magnetism. In fact, it was proven[5]

Document signat digitalment per: CRISTINA RONCERO BARRERO

that changing the slippage between nearby radicals along the π-stacking direction, the magnetic interaction could change from extremely AFM to FM. Therefore, if magnetism is so dramatically dependent on geometry changes, it is likely that those changes undergone by that the crystal packing of the neutral molecular entities upon temperature cooling/heating result in changes on the value of J_{AB} exchange couplings. We believe that geometry optimisations will be an exceedingly valuable tool to assess the magnetic interactions that might be important at 0 K for (S,Se) and (Se,Se) compounds and, thus, provide a better description of their electronic structure and properties.

5.2. Interpreting the magnetic response using optimised crystal packing at 0 K

Geometry optimisations using PBE-D2 and periodic boundary conditions have been carried out for all four bisDTA materials in order to obtain the best estimate of their structure at 0 K. Although both the optimisation procedure and PBE functional have certainly limitations, the resultant crystal packing of all four bisDTA neutral radicals will provide an educated guess on how changes upon contraction (at 0 K) affect the magnetic coupling between bisDTA radicals. Following the same FPBU strategy applied to the X-Ray structure data (see previous Section 5.1), all symmetry-unique pairs of radicals were extracted from the optimised crystal packing, and their J_{AB} magnetic interactions evaluated. Although distances between pairs of radicals have not varied substantially after optimisation (see Table 5.3 for a full comparison of distances between radicals before and after geometry optimisation), in general the magnetic couplings at 0 K become more FM, or less AFM (see Table 5.3 for all J_{AB} values and Figure 5.9 for magnetic topologies at 0 K). Yet, there are some important changes. For instance, the (Se,Se) π-stacking J_{π} magnetic interaction has changed sign (from -7.4 cm^{-1} to +2.2 cm^{-1}) after the $E_2 \cdots E_2$ distance decreases from 4.13 to 4.09 Å. In addition, some exchange couplings that were negligible at 100 K are now significant: (i) FM in J_{2b} of (S,S) and J_{π} of (S,Se); (ii) AFM in J_{2c} of (S,Se) and J_{2b} of (Se,Se).

Document signat digitalment per: CRISTINA RONCERO BARRERO

s

Table 5.3. Exchange J_{AB} couplings (in cm^{-1}) computed at UB3LYP/6-311+G(d,p) level using the X-ray crystallographic data at 100 K, and the optimised crystal data at 0 K. Note that $E_2 \cdots E_2$ and shortest $E_2 \cdots E_1$ distances (in Å) between radicals are given for comparison purposes. Also crystal orientation of all three radical pairs with significant J_{AB} interactions within the crystal is given (notice that *a*- and *b*-axes are equivalent due to $P\bar{4}2_1m$ symmetry).

System	Radical pair	orientation	Dist ($E_2 \cdots E_2$) / Å		Dist ($E_2 \cdots E_1$) / Å		J_{AB} /cm^{-1}	
			0 K	100 K	0 K	100 K	0 K	100 K
(S,S)	J_π	*c*-axis (π-stacking)	4.01	4.03	3.69	3.68	-1.45	-5.60
	J_{2b}	ac(=bc)-plane	3.40	3.49	3.25	3.52	3.73	0.01
	J_{2c}	*a(=b)*-axis	3.25	3.34	4.23	4.30	5.36	3.80
(S,Se)	J_π	*c*-axis (π-stacking)	3.95	4.02	3.74	3.74	7.77	0.30
	J_{2b}	ac(=bc)-plane	3.37	3.40	3.58	3.61	-2.11	0.35
	J_{2c}	*a(=b)*-axis	3.07	3.27	4.22	4.39	11.51	7.20
(Se,S)	J_π	*c*-axis (π-stacking)	4.09	4.09	3.74	3.68	-8.01	-12.40
	J_{2b}	ac(=bc)-plane	3.61	3.54	3.48	3.44	0.66	1.50
	J_{2c}	*a(=b)*-axis	3.17	3.40	4.16	4.36	7.19	3.40
(Se,Se)	J_π	*c*-axis (π-stacking)	4.09	4.13	3.81	3.78	2.22	-7.40
	J_{2b}	ac(=bc)-plane	3.49	3.46	3.60	3.58	-1.36	0.09
	J_{2c}	*a(=b)*-axis	3.20	3.36	4.40	4.53	8.67	5.60

The resulting magnetic topologies at 0 K (Figure 5.9) are, in general, more intricate than at 100 K (Figure 5.5). The only exception being the (Se,S) material that presents a less corrugated magnetic topology formed by FM planes (+7.2 cm^{-1} along *a*- and *b*-axes) connected antiferromagnetically along the π-stacking direction (-8.0 cm^{-1}). The remaining bisDTA-materials present 3D magnetic topologies formed by FM planes connected by competing FM and AFM interactions along the third crystallographic axis (see Figure 5.9). Magnetic models

Document signat digitalment per: CRISTINA RONCERO BARRERO

(a) **(S,S)**

$E_2\cdots E_2$ distance /Å	J_{AB} /cm^{-1}
4.01	-1.5
3.40	+3.7
3.25	+5.4

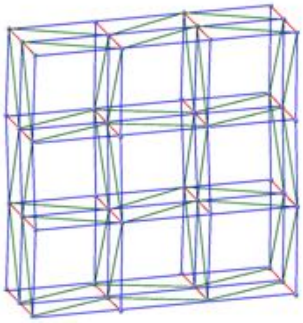

(b) **(S,Se)**

$E_2\cdots E_2$ distance /Å	J_{AB} /cm^{-1}
3.95	+7.8
3.07	-2.1
3.37	+11.5

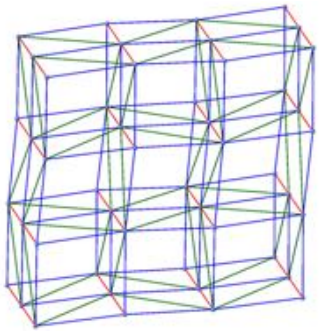

(c) **(Se,S)**

$E_2\cdots E_2$ distance /Å	J_{AB} /cm^{-1}
4.09	-8.0
3.17	+7.2

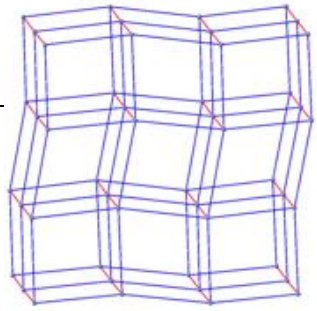

(d) **(Se,Se)**

$E_2\cdots E_2$ distance /Å	J_{AB} /cm^{-1}
4.09	+2.2
3.49	-1.4
3.20	+8.7

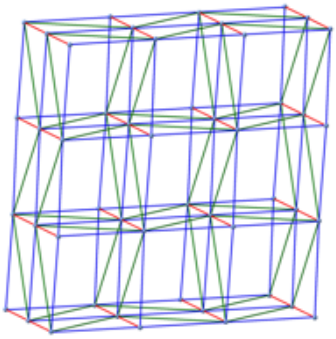

Figure 5.9. Magnetic topology and significant J_{AB} interactions using 0 K optimised structures for (a) (S,S) , (b) (S,Se) , (c) (Se,S) , and (d) (Se,Se) compounds. Colour code: red = π-stacking magnetic coupling along *c*-axis (J_{π}); blue and green = in-plane magnetic couplings (J_{2b} , J_{2c}).

models have been extracted from these new magnetic topologies analogously to the 100 K topologies, to then calculate their macroscopic magnetic susceptibility, $\chi T(T)$.

We must highlight that with these new J_{AB} interactions at 0 K, the global magnetic topology picture for (S,Se) and (Se,Se) systems is equivalent: a 3D FM network with weaker AFM contacts (see -2.1 cm^{-1} for (S,Se) and -1.4 cm^{-1} for (Se,Se) in green in Figures 5.9b,d). At this point, it is interesting to stress the presence of a small AFM interaction (-1.4 cm^{-1}) within the 3D FM network (+8.7 and +2.2 cm^{-1}) in the (Se,Se) system. Yet, the (Se,Se) magnetic topology at 0 K may now be compatible with FM ordering since both the FM couplings (+8.7 cm^{-1}) are stronger than these AFM interactions (-1.4 cm^{-1}) and there are FM π-stacking

Document signat digitalment per: CRISTINA RONCERO BARRERO

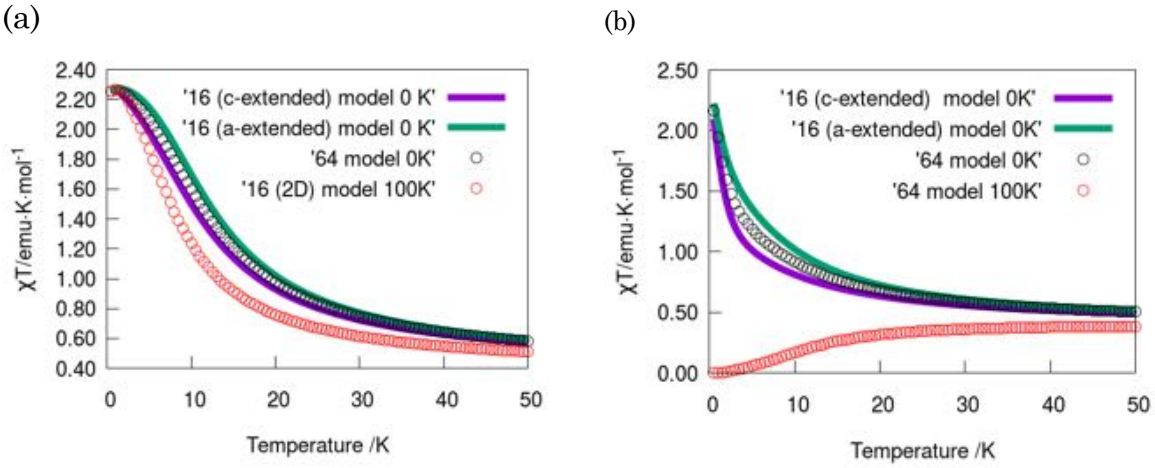

Figure 5.10. Magnetic susceptibility χT(T) curves calculated using J_{AB} evaluated with the crystallographic structure at 100 K (X-Ray data, in red), and at 0 K (optimised structure, in black) for (a) (S,Se) and (b) (Se,Se).

interactions (+2.2 cm^{-1}) competing with those just mentioned weaker AFM contacts. The same reasoning can be applied to (S,Se) molecular material.

For (S,Se) at 0 K and (Se,Se) at 100 and 0K, the magnetic models used are the 16-radical model extended either along the *a*- or *c*-axes and the analogous to a 64-radical 3D model made from averaging the χT(T) data obtained using the two 16 radical models (see Figure 5.6 for a reminder). For (S,Se) at 100 K, a 16-radical 2D model was used instead (see Figure 5.7). Therefore, upon lowering temperature, important changes in the magnetic interactions for both (S,Se) and (Se,Se) appear, which could successfully explain their experimentally observed bulk ferromagnetic behaviour. For (S,Se), the magnetic topology converts from 2D to 3D, which can thus agree with being a bulk ferromagnet. In fact, their ground state is captured to have a high spin multiplicity (to be compared with a singlet ground state at 100 K for (Se,Se)). Lastly, it must be mentioned that simulations of χT(T) using the magnetic topology at 0 K agree with an overall bulk FM response (see Figure 5.10). Thus it is finally possible to conclude that (S,Se) and (Se,Se) materials behave as ferromagnets. However, once more, the values of J_{AB}'s at 0 K are not large enough as to be able to numerically reproduce the experimentally reported χT(T) magnetic susceptibility data.

Document signat digitalment per: CRISTINA RONCERO BARRERO

5.3. Extracting magnetic information from spin correlation

Representations of the spin correlation for the ground state using both (Se,Se) geometries at 100 K (X-Ray) and 0 K (optimised) show how magnetic centres are coupled (see Figure 5.11). In agreement with its magnetic topology, the spin ground state for the X-Ray structure at 100 K consists of planes of FM coupled spins (in blue, Figure 5.11a) which are then antiferromagnetically interconnected (in red, Figure 5.11a) (see short- and long-range spin-spin correlation in Figure 5.11a top and bottom, respectively), resulting in an overall antiferromagnet at low temperatures (see χT(T) data in red, Figure 5.10b). This situation is reversed when inspecting the spin correlation using the optimised crystal data at low temperature (0 K): the (Se,Se) system exhibits a ferromagnetically ordered ground state with relatively strong both short- and long-range FM interactions (see Figure 5.11b, and Figure 5.10b for χT(T) data in black).

The representation of short- and long-range spin correlation for the (S,Se) thiaselenazolyl system shows a ferromagnetic ordered ground state using both experimental X-Ray geometry at 100 K and optimised PBE-D2 geometry at 0 K. The main difference is that the magnetic topology is low dimensional (2D) at 100 K (see Figure 5.12a), whereas it is three-dimensional (3D) at 0 K (see Figure 5.12b). Despite the presence of weak AFM inter-stack J_{AB} at 0 K (J_{2c} = -2.1 cm^{-1}), the (S,Se) system presents a global FM ordering due to the propagation of short- and long-range interactions along all three crystallographic directions. This propagation will indeed also affect the critical temperature of the material.

For (S,Se) material, the experimental critical temperature is 12.8 K.[1] Using the 2D magnetic topology of the X-Ray data at 100 K, the C_p and C_s maxima were *ca.* 8 K and 5 K, respectively (see Figure 5.13a). These results must be compared with those obtained using the 3D magnetic topology of the optimised crystal data at 0 K, where C_p and C_s maxima become *ca.* 12.2 K and 10 K, respectively (see Figure 5.13b). It is thus clear that the magnetic topology at low

Document signat digitalment per: CRISTINA RONCERO BARRERO

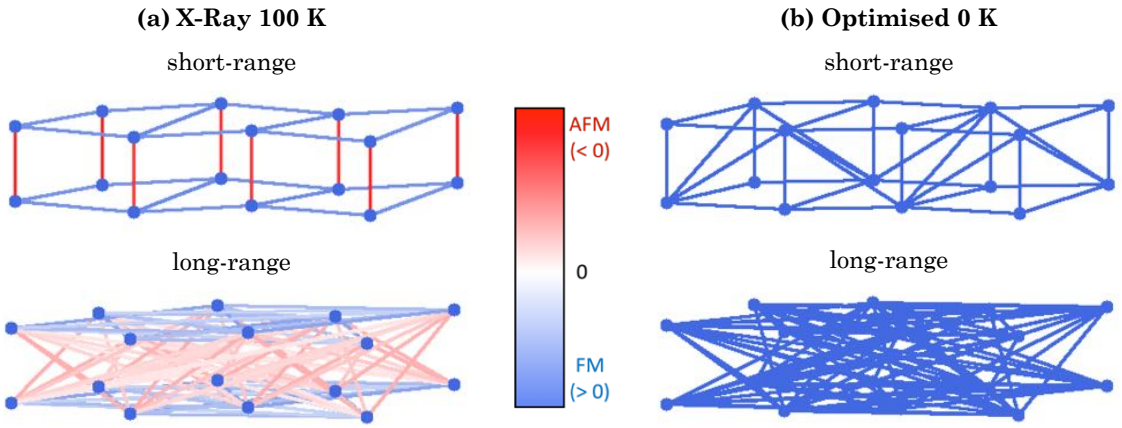

Figure 5.11. Short- and long-range spin exchange density matrix elements, P_{ij} , of the ground state for (Se,Se) system obtained using (a) X-Ray data at 100 K, and (b) 0 K optimised geometry data. Colour encodes for the sign of the interaction: blue means FM spin alignment and red stands for AFM alignment. Intensity of colour represents the relative strength of the interaction.

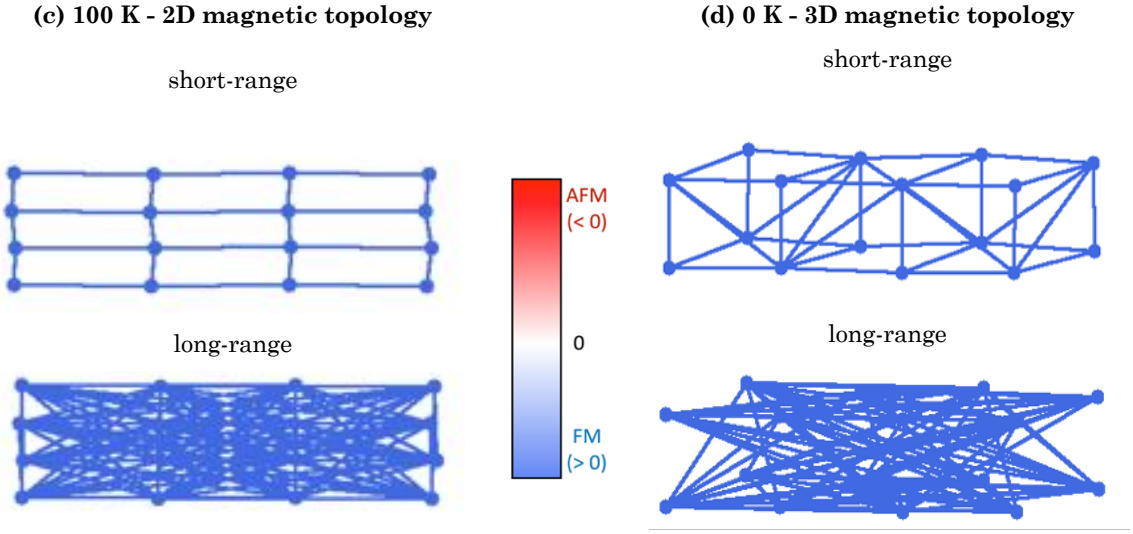

Figure 5.12. Short- and long-range spin exchange density matrix elements, P_{ij} , of the ground state for (S,Se) system obtained using (a) X-Ray data at 100 K, and (b) 0 K optimised geometry data. Colour encodes for the sign of the interaction: blue means FM spin alignment and red stands for AFM alignment. Intensity of colour represents the relative strength of the interaction.

temperature is necessary to portrait adequately the electronic structure of (S,Se) in the region close to the T_C critical temperature. The difference between $T_{C,max}$ for C_s and C_p shows a slower decrease of the long-range interactions at 0 K (see higher intensity of blue lines at 20 K in Figure 5.13b compared to 5.13a), as well

Document signat digitalment per: CRISTINA RONCERO BARRERO

as an increase of the 3D propagation of the spin coupling due to enhanced short-range interactions at low temperature (0 K) compared to higher temperature (100 K, X-Ray) (see evolution of short- and long-range spin correlation upon temperature (2K in blue, 8K@100K / 12.2K@0K in orange & 20K in red) inset in Figure 5.13). It is important to remark that $C_s(T)$ has negative values because it describes the evolution of $\langle S^2 \rangle$ as a function of temperature for a ferromagnet. A ferromagnetically ordered material, whose maximum $\langle S^2 \rangle$ value is achieved at 0 K, will thus present a negative slope due to the loss of the spin parallel alignment by thermal effects.

To sum up, thanks to the optimised crystal structures at 0 K, the true picture of the magnetism of (S,Se) and (Se,Se) has been disclosed. Magnetic couplings between radicals, magnetic topology, spin multiplicity of ground state, magnetic response, spin alignment, as well as short- and long-range correlations, they all agree with the overall macroscopic magnetism of both systems. However, the large FM values experimentally measured for $\chi T(T)$ magnetic susceptibilities at T_C (*ca.* 200 emu·K·mol^{-1}) for these two bisDTA compounds are still not quantitatively reproduced. We do know that molecule-based systems with π-arrangement of radicals, such as the title bisDTA compounds, are highly sensitive to structural changes.[5] In fact, specific studies in the literature analyse the dependence of the J_{AB} magnetic interactions along the π-stacking on the longitudinal and latitudinal slippages (along x- and y-axes, respectively) of two adjacent bisDTA radicals along the π-stack (see Figure 5.13 for details).[1,2] Therefore, detection and screening of the potential geometrical variables that may affect the value of J_{AB} exchange coupling could give us crucial information on which changes need to undergo the material in order to achieve the strong FM interaction that experimentalists have observed through $\chi T(T)$ magnetic susceptibility measurements.

Document signat digitalment per: CRISTINA RONCERO BARRERO

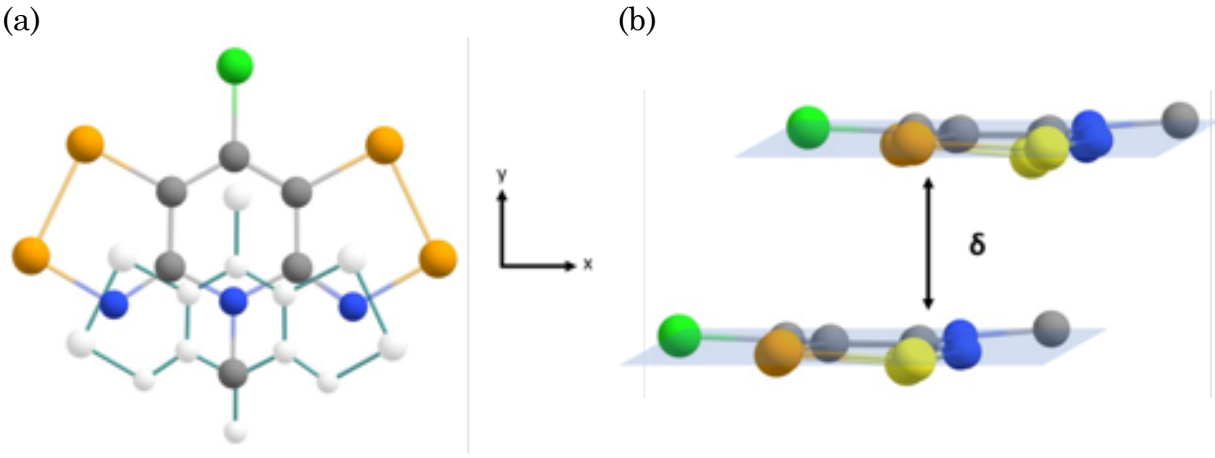

Figure 5.13. (a) Representation of a pair of bisDTA radicals along the π-stacking direction showing longitudinal and latitudinal slippages (along x- and y-axes, respectively). Note that the ethyl substituent has been omitted for simplicity. Bottom monomer in white for contrast and visualization purposes. (b) Pair of bisDTA radicals piled up at a δ interplanar distance parallel to the π-stacking.

5.4. Magneto-structural correlations

Relationships between structure and magnetic interactions are difficult to establish in molecule-based materials because slight changes in the intermolecular arrangement between radicals might have substantial consequences in terms of magnetic response. Let us stress here that finding magneto-structural correlations for materials formed from neutral molecules as building blocks will encounter more marked difficulties since dispersion interactions are the driving forces to induce the resulting crystal structure. Previous studies[2] established some dependencies between the slippage of π-stacked bisDTA-radicals and their J_{AB} coupling. Indeed, slippage was explored along x- and y-axes at a fixed interplanar distance (δ) of 3.5 Å, in accordance with that observed between bisDTA radicals in the X-Ray crystal packing characterised at 100 K[3] (see Figure 5.13). The reported magneto-structural correlation maps were computed with π-stacked radical pairs constructed with optimised UB3LYP/6-31G(d,p) monomers, in which ethyl and Cl substituents were replaced by hydrogen atoms. This study concluded that, as was observed experimentally, small variation in the tetragonal packing of the title four bisDTA

Document signat digitalment per: CRISTINA RONCERO BARRERO

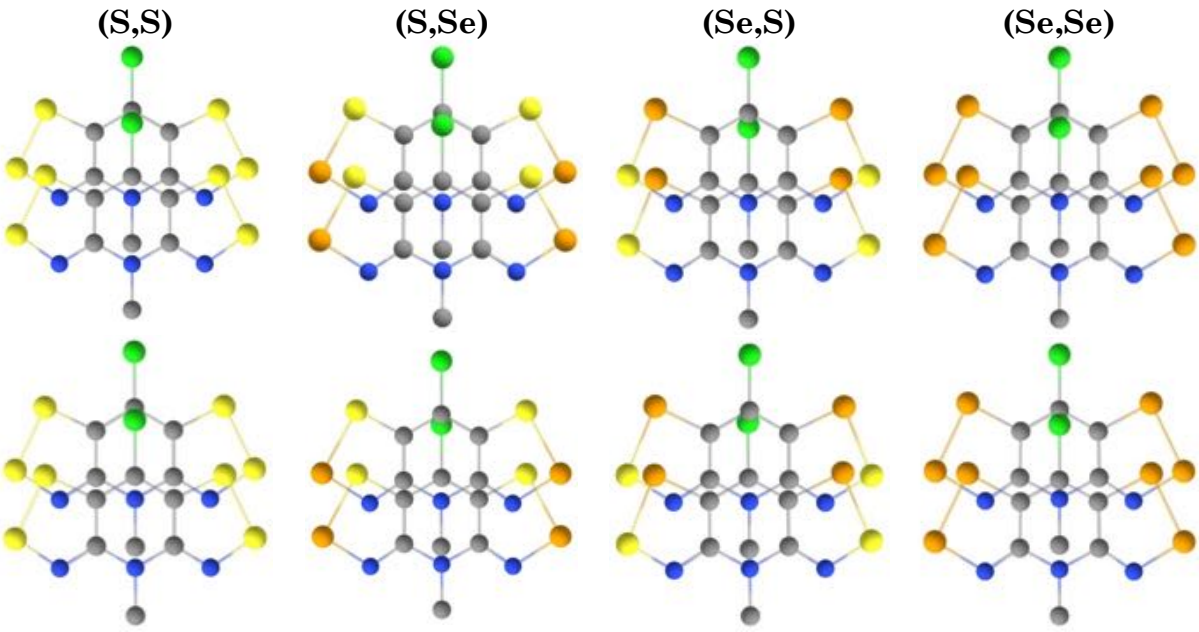

Figure 5.14 Representation of dimers along the π-stacking for all four bisDTA compounds extracted from the X-Ray crystallographic data at 100K (top row) and the PBE-D2 optimised crystals at 0K (bottom row). Note that changes from 100K to 0K geometries cannot be appreciated from direct observation of the radicals pair; a detailed comparison in terms of internuclear distances is instead required.

derivatives has strong effects on the value of the stacking J_{AB} interaction. In fact, substituents do not just introduce bulk protection but also can tune the magnetism by shifting the relative position of stacked radicals, even changing its interaction from AFM to FM.

For the title bisDTA compounds we indeed inferred that, even though all J_{AB} interactions are affected by the contraction of the geometry upon decreasing temperature, certain π-stack J_{AB} pairwise interactions are able to change the global picture of the overall magnetism. Therefore, our objective focused at elucidating the effects on J_{AB} spin coupling observed when relaxing the geometry at 0 K, *i.e.* on potential temperature effects on J_{AB} for a given bisDTA compound. With this aim in mind, we re-explored the correlation maps of J_{AB} magnetic coupling as a function of interplanar distance (δ) and longitudinal (x) and latitudinal (y) slippages between radicals (see Figure 5.13 for its definition) at UB3LYP/6-311+G(d,p) level for the (Se,Se) compound using a pair of radicals along the π-stack extracted from the X-Ray crystal data at 100 K (see Figure 5.15). Note that in our study no substituent was replaced by hydrogen atoms,

Document signat digitalment per: CRISTINA RONCERO BARRERO

and that the 6-311+G(d,p) basis set was used to include diffuse functions, which are very useful to describe heavy atoms (e.g. S, Se, Cl), on top of polarization functions. It was observed that the effect due to the longitudinal (x) slippage could be neglected, since the crystal packing of the four bisDTA compounds does not exhibit this type of slippage (see Figure 5.14 for (Se,Se) pair and Figure 5.15a for correlation map). We can anticipate that this correlation map shows that the (Se,Se) material can transition from AFM to FM due to structural changes (see projection in Figure 5.15a for colour change from AFM in blue to FM in red), which can be in turn related to temperature changes. Accordingly, it can be concluded that the leading magnetic behaviour in J_{π} is mainly driven by a latitudinal slippage (FM for 1.80-2.15Å y-slippage; AFM for values of y-slippage larger than 2.15Å), and its magnitude is then finely tuned by the interplanar δ distance (δ <3.46Å). In fact, the correlation map for (Se,Se) predicts the -1.57 cm^{-1} value of the J_{π} stacking magnetic interaction for the (Se,Se) compound that was recently characterised at 2 K[6] (see △ in Figure 5.15a; note that J_{π} at 2 K has been evaluated at UB3LYP/6-311+G(d,p) level).

Finally, upon temperature cooling/heating it is likely there might be intra-monomer changes as well as intermolecular contraction/expansion, as those explored by varying the slippage and interplanar distance between radicals. Therefore, the sensitivity to structural changes has been further tested by re-calculating the (Se,Se) magneto-structural correlation map using as bisDTA monomer the radical extracted from the optimised crystal data at 0 K (see Figure 5.15b). Comparison between those two magneto-structural correlation maps for (Se,Se) (Figures 5.15a and 5.15b) shows that there is indeed an enlargement of the FM region upon monomer relaxation (y-slippage now ranges from 1.85 to 2.25Å), which encompasses the geometry of the FM π-stacking (Se,Se) pair of radicals encountered at 0 K (+2.2 cm^{-1}). It thus follows that small changes due to geometry relaxation not only between radicals (intermolecular) but also at the intra-monomer level clearly affect the conditions for orthogonal overlap between SOMOs and, in turn, for FM interaction. However, at the light of these correlation

Document signat digitalment per: CRISTINA RONCERO BARRERO

(a) Pair of radicals extracted from experimental 100 K crystal structure

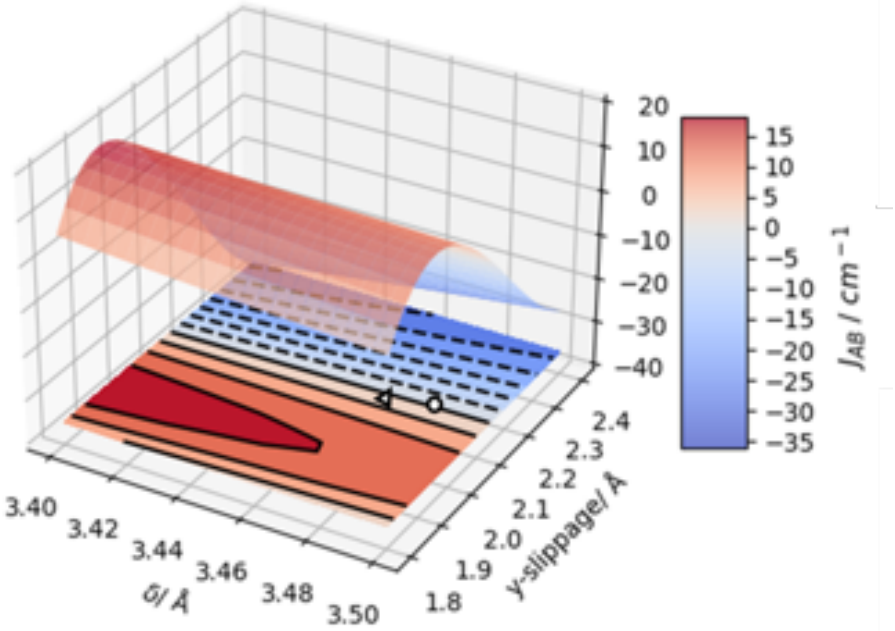

(b) Pair of radicals extracted from optimised 0 K crystal structure

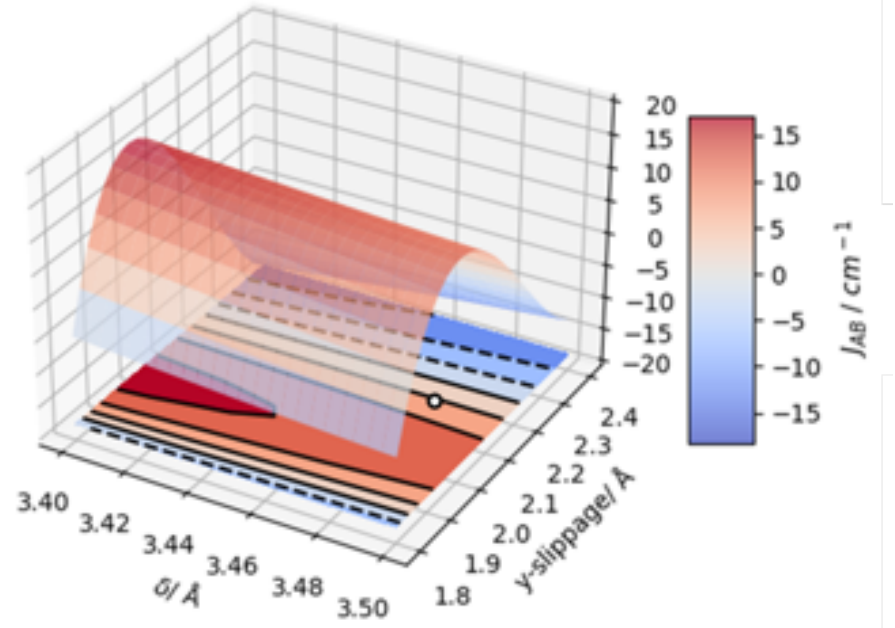

Figure 5.15. Magneto-structural correlation maps of a π-stacked pair of (Se,Se) radicals as a function of δ interplanar distance and latitudinal (y) slippage. Pair models have been constructed using (a) the X-Ray 100 K monomer from Ref. [3]and (b) the 0 K optimised monomer at PBE-D2 level. All J_{AB} are computed at UB3LYP/6-311+G(d,p) level. Values of J_{AB} magnetic coupling calculated using (Se,Se) π-stacked radicals at 100 K (○) and 2 K (△) X-Ray data are located in correlation map (a), while that at 0 K (○) is placed in correlation map (b).

Document signat digitalment per: CRISTINA RONCERO BARRERO

maps, even in the best-case scenario, the numerical values of the π-stacking magnetic interactions preclude to obtain magnetic susceptibility values of the actual order measured by experiments in polycrystalline samples (note that maximum χT(T) value reaches *ca.* 200 emu·K·mol^{-1} at T_C for (S,Se) and (Se,Se) bulk ferromagnets). In fact, the large values experimentally measured for χT(T) would require ferromagnetic J_{AB} values that are much larger than any of the J_{AB}'s reported for this type of compounds. Irrespective of whether the discrepancy between the computed and measured value may be attributed to theory or experiment, it is clear that the magneto-structural correlation maps are able to predict the variations of J_{AB} for bisDTA derivatives. The resultant correlation maps show that the stacking J_{AB} magnetic interaction is highly sensitive to variations on latitudinal (y) slippage, and that interplanar δ distance and intramonomer geometry are exceedingly important factors controlling the temperature at which long-range magnetic ordering emerges.

5.5. Conclusions

It has been observed that changing S by its Se heavier alternative in the molecular skeleton of these bisDTA materials introduces not just more diffuse orbitals, and hence a larger overlap between nearby radicals, but also small changes in the crystal packing that considerably affect their magnetic properties. These effects have indeed been evidenced analysing the 100 K magnetic topologies of the materials. Pure bisdithiazolyl (S,S) and bisdiselenazolyl (Se,Se) systems present a 3D magnetic topology of ferromagnetic planes connected antiferromagnetically. On the other hand, mixed thiaselenazolyl (S,Se) and (Se,S) materials present different magnetic topologies due to the Se position. It has been observed that Se substitution in the E_1 position substantially enlarges the antiferromagnetic interaction, resulting in the spin-canted antiferromagnetic behaviour of (Se,S). Contrarily, Se in E_2 position shifts the π-staking interaction to positive values resulting in the ferromagnetic 2D topology of (S,Se). Strikingly, the 100 K magnetic topology only agrees with experiment for (S,S) and (Se,S) compounds, while for (S,Se) and (Se,Se) fails to portrait the significant magnetic

Document signat digitalment per: CRISTINA RONCERO BARRERO

couplings. The position of the heteroatoms in the neutral organic radical is thus crucial in the resultant properties of the materials.

Following the FPBU working strategy with the 100 K structures, we have been able to rationalise the macroscopic susceptibility of (S,S) and (Se,S) materials. (S,Se) and (Se,Se) derivatives have been found to be more sensitive to thermal effects, and the expected global ferromagnetic picture cannot be inferred using X-Ray data at 100 K. Upon optimisation of the crystal structure, the magnetic topologies at 0 K of both materials show clear differences, due to the fact that the π-stacking (*c*-axis) coupling is the most affected by the geometry rearrangements upon temperature cooling. The J_{π} magnetic interactions along the stacking have increased their ferromagnetic character after optimisation from +0.3 cm^{-1} to +7.8 cm^{-1} in (S,Se) and from -7.4 cm^{-1} to +2.2 cm^{-1} in (Se,Se). The expected FM spin arrangement for a bulk ferromagnet is thus obtained in both cases. Results have been corroborated comparing the experimental T_C with computed $T_C(C_s)$ and $T_C(C_P)$ for (S,Se). Reported geometries at temperatures close to T_C are thus of vital importance to describe correctly the microscopic magnetic behaviour of molecular materials whose crystal structure is driven by weak cohesive forces (reduced to dispersion or weak N···S / N···Se electrostatic interactions) between the constituent neutral molecular entities. Therefore, in absence of crystallographic data, fixed cell PBE-D2 optimisations are a very useful tool for the qualitative evaluation of the thermal effects in both the geometry and the microscopic magnetic interactions at temperatures below the critical magnetic temperature. This holds true in our case because (i) our target systems are organic radical based materials (whose crystal packing is mainly driven by dispersion interactions), (ii) dispersion interactions are adequately described using Grimme (D2) approximation, and (iii) fixed cell optimisations are possible since cell parameters could be extrapolated from available experimental crystallographic data at two different higher temperatures (namely, 100 and 295 K).[3]

Document signat digitalment per: CRISTINA RONCERO BARRERO

Magneto-structural correlation maps have evidenced the high sensitivity of the π-stacking J_{π} magnetic couplings to variations according to latitudinal slippage and interplanar distances. In fact, these correlation maps enable to locate both the J_{π}(X-Ray @100K) and the J_{π}(0 K) interactions for (Se,Se) close to the FM and AFM boundary region as well as recently reported J_{π}(2 K)[6]. This frontier region is believed to explain the anomalous AFM interactions observed for the (Se,Se) bulk ferromagnet at 100 K, since clearly π-stacking J_{π} interactions are very sensitive to subtle structural modifications of the crystal packing, which can be actually used to tune the very experimental response.

All in all, magnetic coupling between radicals, magnetic topology, spin multiplicity of ground state, magnetic response, spin alignment, short- and long-range correlations, as well as magneto-structural correlation maps have proven themselves to be exceedingly useful tools to gain insights into the true picture of the overall macroscopic magnetism of the S/Se bisDTA family of multifunctional materials.

5.6. References

1 Robertson, C. M., Leitch, A. A., Cvrkalj, K., Myles, D. J. T. T., Reed, R. W., Dube, P. A., & Oakley, R. T. (2008). Ferromagnetic ordering in bisthiaselenazolyl radicals: Variations on a tetragonal theme. Journal of the American Chemical Society, 130(44), 14791–14801. https://doi.org/10.1021/ja8054436

2 Leiten, A. A., Yu, X., Winter, S. M., Secco, R. A., Dube, P. A., Oakley, R. T., Leitch, A. A., Yu, X., Winter, S. M., Secco, R. A., Dube, P. A., Oakley, R. T., & Ls, O. (2009). Structure and property correlations in heavy atom radical conductors. Journal of the American Chemical Society, 131(20), 7112–7125. https://doi.org/10.1021/ja900853t

3 Robertson, C. M., Leitch, A. A., Cvrkalj, K., Reed, R. W., Myles, D. J. T., Dube, P. A., Oakley, R. T., & Ls, O. (2008). Enhanced conductivity and magnetic ordering in isostructural heavy atom radicals. Journal of the American Chemical Society, 130(26), 8414–8425. https://doi.org/10.1021/ja801070d

4 M. Deumal, J.M. Rawson, A.E. Goeta, J.A.K. Howard, R.C.B. Copley, M.A. Robb, J.J Novoa, Chem. Eur. J., 2010, 16, 2741–2750

Document signat digitalment per: CRISTINA RONCERO BARRERO

5 T. Francese, J. Ribas-Arino, J.J. Novoa, R.W.A. Havenith, R. Broer, C. de Graaf, M. Deumal, Phys. Chem. Chem. Phys., 2018, 20, 20406–20416

6 C.M. Robertson, S.M. Winter, J.A.K. Howard, M.R. Probert, R.T. Oakley, Chem. Commun. 2021, 57, 10238-10241

Document signat digitalment per: CRISTINA RONCERO BARRERO

Chapter 6. Hopping Transport in bisDTA Materials

Chapter 5 has dealt successfully with the distinct magnetism of bisdithiazolyl (S,S), mixed bisthiaselenazolyl (S,Se) and (Se,S) and bisdiselenazolyl (Se,Se) compounds. Now it is the turn to gain insights into the electric properties exhibited by these four selected bisDTA systems depending on the S/Se content and its position (see Figure 6.1)[1]. Specifically, the electric conductivity ($\sigma_{E_1E_2}$) increases as $\sigma_{SS} < \sigma_{SeS} < \sigma_{SSe} < \sigma_{SeSe}$ (see values for σ in S cm^{-1} at 300K in Figure 6.1b). Although a conductivity rising was expected with the incorporation of Se, mixed thiaselenazolyl (S,Se) and (Se,S) materials demonstrate that the particular positions occupied by the heteroatoms (E_1 or E_2, see Figure 6.1a) within the ring also affects the magnitude of the conductivity, being σ_{SSe} at 300K one order of magnitude larger than σ_{SeS}. Activation energies (E_a) obtained using the experimental conductivity data range from 0.43 eV to 0.19 eV (see E_a values listed in Figure 6.1b). Bearing in mind that conductivities present an Arrhenius-like behaviour, with values that increase when heating, E_a's for the title compounds indicate that a hopping mechanism is expected to prevail in this family of bisDTA compounds. Yet, we will have to challenge the validity of the hopping mechanism since the slight decrease of E_a from 0.43 eV in (S,S) to 0.19 eV in (Se,Se) might hint at entering to an intermediate (hopping / band) regime of charge transport, which would require another approach to be studied. Note that, at the crossroad to whether address the study of these four isostructural bisDTA-compounds from either a pure band or a pure hopping perspective, the results obtained using periodic calculations showed that the band structure of the title compounds exhibits narrow bands of 0.2-0.3 eV dispersion and indirect band gaps of 1.15-1.40 eV (see Chapter 4). Although in line with the experimental

Document signat digitalment per: CRISTINA RONCERO BARRERO

a)

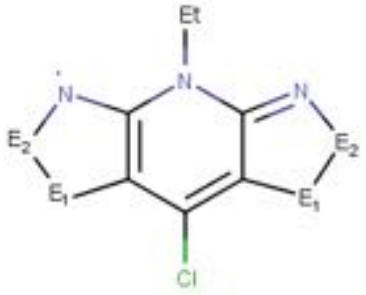

b)

	E_a (eV)	σ (S cm^{-1}) [T=300K]	Magnetic properties at low T	T_c (K)
(S,S)	0.43	$3.2 \cdot 10^{-6}$	No long-range order	--
(S,Se)	0.27	$1.0 \cdot 10^{-4}$	Bulk FM	12.8
(Se,S)	0.31	$2.2 \cdot 10^{-5}$	Spin-canted AFM	14.0
(Se,Se)	0.19	$3.0 \cdot 10^{-4}$	Bulk FM	17.0

Figure 6.1. The family of bisDTA materials studied in this work: (a) the radicals are classified according to whether E_1 and E_2 positions are S or Se atoms, (b) Activation energy (E_a) and conductivities (σ) at 300 K extracted from Ref.[1]

behaviour, these calculated data resulted to be insufficient to explain their conductivity, suggesting the necessity to study the title compounds using either an intermediate or a hopping model (in agreement with what the values of E_a hint at).

Hereafter, in this chapter, we will focus on interpreting the distinct conductivity exhibited by pure bisdithiazolyl (S,S), mixed thiaselenazolyl (S,Se) and (Se,S), and pure bisdiselenazolyl (Se,Se) compounds. Despite slight differences in distance and tilting angles, all four materials show analogous tetragonal $P\bar{4}2_1m$ crystal packing, which will allow us to develop a unique bottom-up working strategy and compare directly the microscopic differences responsible for the experimentally measured conductivities. It must be also stressed that no experimental evidence suggests whether the resulting electric conductivity is due to holes or electrons and, hence, both mechanisms will have to be investigated. The electric conductivity of these four bisDTA-derivative crystals which, despite remaining activated, increases two orders of magnitude from (S,S) to (Se,Se), will indeed make possible to further test the dim limits of the hopping mechanism applicability in single component radical conductors.

Document signat digitalment per: CRISTINA RONCERO BARRERO

6.1. Marcus rate equation parameters: Electronic coupling and Reorganization energy

Charge transport in the hopping regime is described as the result of subsequent jumps of charge between sites, *i.e.* between radical molecules of each bisDTA materials under study. The rate constant of each possible jump is computed using the widely known Marcus equation[2] which in our case depends mainly on two parameters: the H_{DA} electronic coupling and the λ reorganization energy.[3,4] We will thus evaluate the electric conductivity by computing the parameters that control these hopping rates by means of first-principles calculations. The analysis of these parameters and, subsequently, the comparison between systems will allow us to untangle the electronic/structural factors responsible for the different conductivities of these compounds. We will now proceed to discuss in detail the results regarding the calculation of electronic couplings (Section 6.1.1), reorganization energies (Section 6.1.2), rate constants (Section 6.2), mobility and spin-carrier density (Section 6.3), and ultimately electric conductivity (Section 6.3).

6.1.1 H_{DA} Electronic coupling

First, a complete analysis of each crystal has been performed in order to select the pairs of bisDTA radicals that are to be candidates to present a non-negligible H_{DA}. Although all 4 materials share the same crystallographic packing, the substitution of S by Se introduces small deviations in the arrangement of the four distinct radicals, which have been found to be crucial in the description of their J_{AB} magnetic interactions and may be also relevant for H_{DA}. In fact, improvement in charge migration in all 4 materials under study is believed to arise from E_2 Se-substituted compounds due to tighter $E_2\cdots E_2$ intermolecular contacts when Se is in this position. Therefore, the $E_2\cdots E_2$ distance has been taken as selection criteria for D···A pairs of bisDTA-monomers (where D/A stands for bisDTA radical acting as donor/acceptor in the charge transfer process), with a 7.0 Å threshold (note that Van der Waals Se···Se distance is *ca.* 3.8 Å[5]).

Document signat digitalment per: CRISTINA RONCERO BARRERO

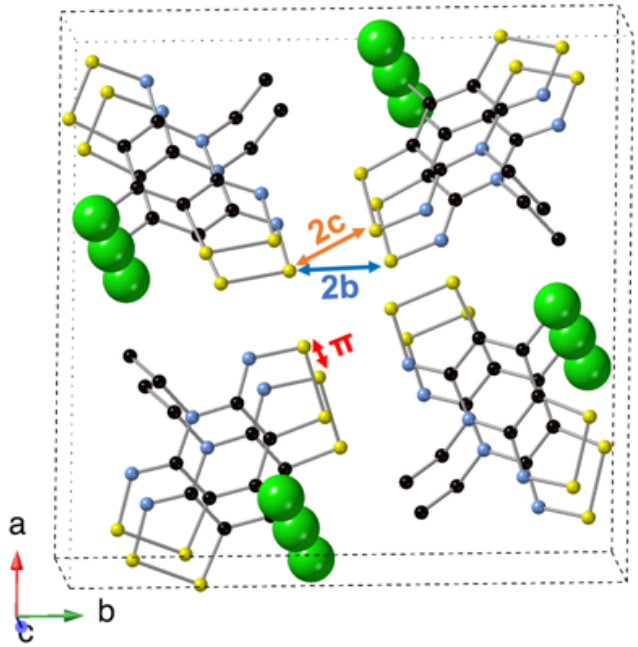

Figure 6.2. Representation of the primary candidates to present relevant H_{DA} in all four bisDTA candidates (full sampling of the 13 dimer clusters studied can be found in the Chapter 3 Section 3.3.1). Note hydrogen atoms have been omitted for clarity.

After an exhaustive evaluation of the intermolecular distances in the crystal, 13 pairs of radicals have been selected as potential candidates (see Chapter 3 Section 3.3.1 for a detailed analysis of the selection of D···A pairs of bisDTA monomers). The complete analysis of the relevant J_{AB} magnetic interactions, discussed in the preceding chapter, showed that lateral magnetic interactions are enlarged when radical pairs present a closer $E_2 \cdots E_2$ contact, being the so-called 2b and 2c lateral contacts which contribute the most to the magnetism (see representation of 2# and π-stacking contacts in Figure 6.2). However, no evidence sustains yet that H_{DA} are analogously affected. The mapping of all possible H_{DA} will reveal the effects of Se-substitution and which are the relevant contacts for the description of $\bar{\bar{\sigma}}$ conductivity.

As discussed in Chapter 3, there is an exact relation between the diabatic and adiabatic state energies in a two-monomer system (see Eq.6.1).

$$E_{1,2} = \frac{1}{2}(E_A + E_D \pm \sqrt{(E_A - E_D)^2 + 4|H_{DA}|^2} \qquad \text{Eq.6.1.}$$

Document signat digitalment per: CRISTINA RONCERO BARRERO

where E_A and E_D are the energy of the initial and final states in the diabatic potentially energy surface (PES) and E_1 and E_2 are the ground and first excited state adiabatic energies, respectively, using the transition state geometry. Hence, with Eq. 6.1, it is possible to compute the H_{DA} electronic coupling using the two diabatic solutions obtained at CASSCF level, and one adiabatic solution which will be computed by performing a state interaction (restricted active space state interaction, RASSI[6]) of the diabatic wavefunctions. Unfortunately, the calculation of these diabatic solutions is not straightforward. In fact, there are a lot of techniques reported in order to deal with this task.[3,4] Initially, we tried to compute these localized solutions. Yet it was only possible to correctly converge some of them (see hole H_{DA} electronic couplings between two π-stacked radicals, $H^{+}_{\pi,\mathrm{diab}}$, in Table 6.1). In order to overcome this convergence problem, the symmetry of the systems was used to simplify Eq. 6.1. Accordingly, H_{DA} was found to be half the energy splitting between E_2 and E_1 adiabatic energies (Eq. 6.2).

$$\Delta E_{12} = E_2 - E_1 = 2|H_{DA}| \qquad \text{Eq.6.2.}$$

Comparison between H_{AD} obtained by means of the diabatic-adiabatic relationship (Eq 6.1, $H^{+}_{\pi,dib}$) and those computed by means of the above energy-splitting-in-dimer method (Eq. 6.2, H^{+}_{π}) shows that the resulting values are numerically analogous. Therefore, electronic couplings were computed using adiabatic energies with CASSCF state-average calculations.

Table 6.1 H^{+}_{π} electronic coupling computed using adiabatic energies with CASSCF state-average calculations (Eq. 6.2) and $H^{+}_{\pi,dib}$ using Eq. 6.1. Note that the value of $H^{+}_{\pi,diab}$ for (S,Se) is missing due to convergence problems (N.C.).

	(S,S)	(S,Se)	(Se,S)	(Se,Se)
$H^{+}_{\pi,\mathrm{diab}}$	32.42	N.C.	58.29	43.75
H^{+}_{π}	31.72	32.22	58.59	49.78

The Koopmans' theorem is another commonly used approximation to evaluate H_{DA}.[7] Within the Restricted Hartree-Fock RHF framework, this theorem states that the first ionization energy of the molecule is equal to the energy of the highest occupied molecular orbital (HOMO) in absolute value, assuming

Document signat digitalment per: CRISTINA RONCERO BARRERO

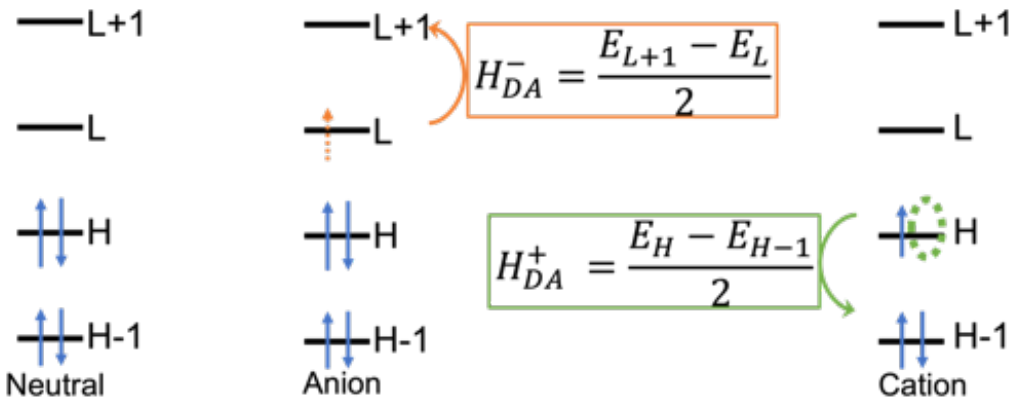

Figure 6.3. Schematic representation of the Koopman's theorem applied to a closed-shell singlet moiety for the evaluation of electron (H_{DA}^{-}) and holes (H_{DA}^{+}) electronic couplings. Note that H and L stand for HOMO and LUMO, respectively.

that the orbitals of the ion are equal to those of the neutral molecule. Within this approach, electron (H_{DA}^{-}) and hole (H_{DA}^{+}) electronic couplings can be evaluated by means of differences between the energies of molecular orbitals (MOs) close to HOMO in a dimer cluster model (see Figure 6.3). Koopmans' theorem method provides an approximation that avoids the sometimes laborious and computational costly evaluation of adiabatic solutions for closed-shell systems. Even though this theorem has been successfully employed in closed-shell systems, the hypothesis assuming that HOMO/HOMO-1 and LUMO+1/LUMO orbitals govern the description of hole and electron mobility fails when applied to open-shell materials constituted by monoradical centres using spin unrestricted formalisms. Indeed, in this type of materials, according to Koopmans' theorem, first excitation energies for positively and negatively charged systems would have to be evaluated using the same pair of orbitals, *i.e.* the singly occupied molecular orbitals of the dimer cluster (SOMO, S_1 and S_2 in Figure 6.4). This obviously prevents the individual evaluation of H_{DA}^{+} and H_{DA}^{-} for open-shell singlet moieties (e.g. two S=1/2 radicals) according to Koopmans' theorem. It is then a must to adapt Koopmans' theorem to this new scenario.

Here, a new proposal for open-shell materials will be probed based on Restricted Open-shell Density Functional Theory RODFT calculations. Although

Document signat digitalment per: CRISTINA RONCERO BARRERO

Figure 6.4. Schematic representation of Koopmans' adapted theorem for an open-shell dimer cluster.

previously attempted[8], we believe that –for the four isomorphous bisDTA compounds– the Koopmans' adapted method will provide a better estimation to assess the importance of the electronic coupling between donor and acceptor, because $\bar{H}_{DA,K}$ gives a mean value accounting for both hole and electron charge transfers. SOMO energies (E_{S1} and E_{S2}) are obtained at ROB3LYP/6-311+G(d,p) level using cluster models with a pair of radicals. This assumption will be challenged by comparing the RODFT results with those calculated according to the evaluation of the energy of their adiabatic ground and first excited states at CASSCF level of theory (according to Eq. 6.2). Let us remind here that H_{DA} values obtained using simplified Eq. 6.2 when contrasted to those obtained from general Eq. 6.1 were found to be in agreement and, thus, reliable.

As mentioned earlier, a previously performed analysis of cluster models showed that the preferential radical···radical contacts might occur in the so-called 2# direction (where # stands for b and c letters, see representation in Figure 6.2). Also π-stacked monomers are known to be a preferred path for conduction in these systems. Hence, dimers of 2b/2c radicals and π-stacked monomers will be the first analysed by evaluation of the energy of their adiabatic ground and first excited states (see results obtained using Eq. 6.2 in Table 6.2). This analysis will aim at testing the above-proposed Koopmans' theorem adaptation based on RODFT calculations, which once tested –if valid– will be used to evaluate all remaining 10 dimers.

Document signat digitalment per: CRISTINA RONCERO BARRERO

Table 6.2 Electronic coupling (in meV) for holes (H_{DA}^{+}) and electrons (H_{DA}^{-}) charge transport obtained according to Eq. 6.2. Notice that r_{DA} distances are measured as the shortest distance between N···E$_1$ atoms (in Å)

	(S,S)			**(S,Se)**			**(Se,S)**			**(Se,Se)**		
	r_{DA}	H_{DA}^{+}	H_{DA}^{-}	r_{DA}	H_{DA}^{+}	H_{DA}^{-}	r_{DA}	H_{DA}^{+}	H_{DA}^{-}	r_{DA}	H_{DA}^{+}	H_{DA}^{-}
π	3.53	31.72	26.81	3.55	32.22	29.03	3.58	58.59	37.63	3.65	49.78	28.07
2b	3.35	80.84	65.87	3.41	102.40	87.40	3.28	144.00	124.60	3.34	149.47	130.62
2c	3.53	21.45	42.65	3.56	62.62	39.95	3.65	12.32	14.83	3.70	24.77	45.01

Comparison between the mean value of $\bar{H}_{DA}$ obtained with CASSCF first excitation energies and $\bar{H}_{DA,K}$ values computed using $\bar{H}_{DA,K} = (E_{S1} - E_{S2})/2)$ evidences that our adaptation of Koopmans' theorem, although it cannot be applied to evaluate H_{DA}^{+} and H_{DA}^{-}, can be used to predict which contacts are potentially relevant (see Figure 6.5 for comparison). This first screening provides a reasonable estimate of $\bar{H}_{DA}$ values, saving time and computational resources. Once the validity of the here-proposed Koopmans' adapted theorem has been successfully asserted, the method was used to scan the 10 remaining directions of the crystal packing showing that, in fact, only 3 pairs of radicals were suitable candidates to contribute to the conductivity of the 4 materials under study (namely, π-stack, 2b and 2c pairs of radicals) (see all results obtained in Table 6.3).

Table 6.3 Computed $\bar{H}_{DA,\,K}$ for the 13 pairs of radicals selected because might exhibit a non-negligible electronic coupling. Note that the largest contributions are due to 2b, 2c and π pairs for the four bisDTA S/Se materials.

	1a	**1b**	**1c**	**2a**	**2b**	**2c**	**3a**	**3b**	**3c**	**8a**	**8b**	**8c**	**π**
(S,S)	4.38	1.02	4.38	2.54	63.66	32.39	4.32	4.43	4.32	2.78	0.03	2.78	20.46
(S,Se)	4.64	1.04	4.62	10.61	87.82	90.97	4.73	7.43	4.73	3.30	0.00	3.29	15.27
(Se,S)	9.85	2.17	9.83	4.26	13.17	104.60	7.16	3.79	7.16	2.45	0.01	2.45	43.44
(Se,Se)	10.16	2.55	10.16	16.88	108.78	56.63	6.04	6.44	6.04	2.35	0.00	2.35	33.99

Document signat digitalment per: CRISTINA RONCERO BARRERO

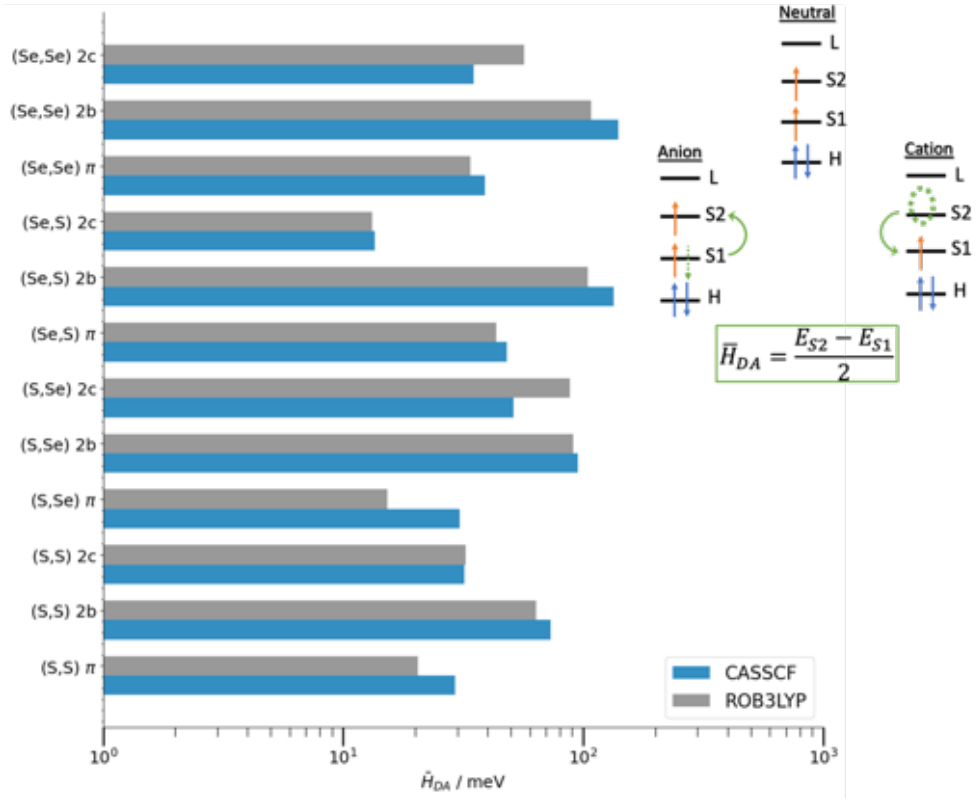

Figure 6.5. Comparison between evaluated $\bar{H}_{DA,\,K}$ using Koopmans' adapted theorem (in grey) and the $\bar{H}_{DA}$ value resulting from averaging hole (H_{DA}^{+}) and electron (H_{DA}^{-}) transfer (CASSCF, in blue). Inset: schematic representation of the proposed equation for the evaluation of the electronic coupling $\bar{H}_{DA,\,K}$ at ROB3LYP level.

The computed H_{DA}^{+} and H_{DA}^{-} values of the selected pairs at CASSCF level, reported in Table 6.2, show a predominance of $H_{2\mathrm{b}}$ in all the systems under study, which increases from (S,S) to (Se,Se) with the Se content. Interestingly, thiaselenazolyl materials present an increase of $H_{2\mathrm{b}}$ when Se is in the E_1 position, which is counter-intuitive with the observed trend for σ. This means that in this case there will be another factor that plays an important role, which (as we will show) it is not the λ reorganization energy, but the ρ_C density of charge carriers. When comparing (Se,S) and (S,Se), it is also observed that, although the incorporation of Se in the E_2 position does not increase $H_{2\mathrm{b}}$ values, it enlarges $H_{2\mathrm{c}}$ (mostly $H_{2\mathrm{c}}^{+}$), which may open an additional path to conduction, improving potentially the averaged charge transport in the (S,Se) material. Note that, for all four systems, computed H_{DA}^{-} are less significant than their H_{DA}^{+} counterpart in the corresponding predominant electronic couplings (see, for instance,

Document signat digitalment per: CRISTINA RONCERO BARRERO

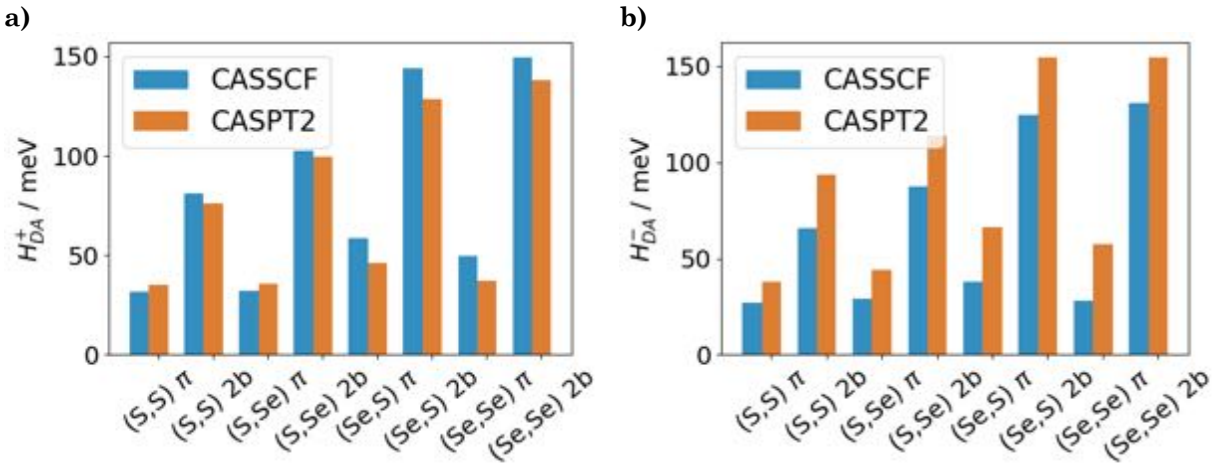

Figure 6.6. Comparison between CASPT2 and CASCF values of (a) hole H_{DA}^{+} and (b) electron H_{DA}^{-} electronic couplings for π and 2b pairs of radicals.

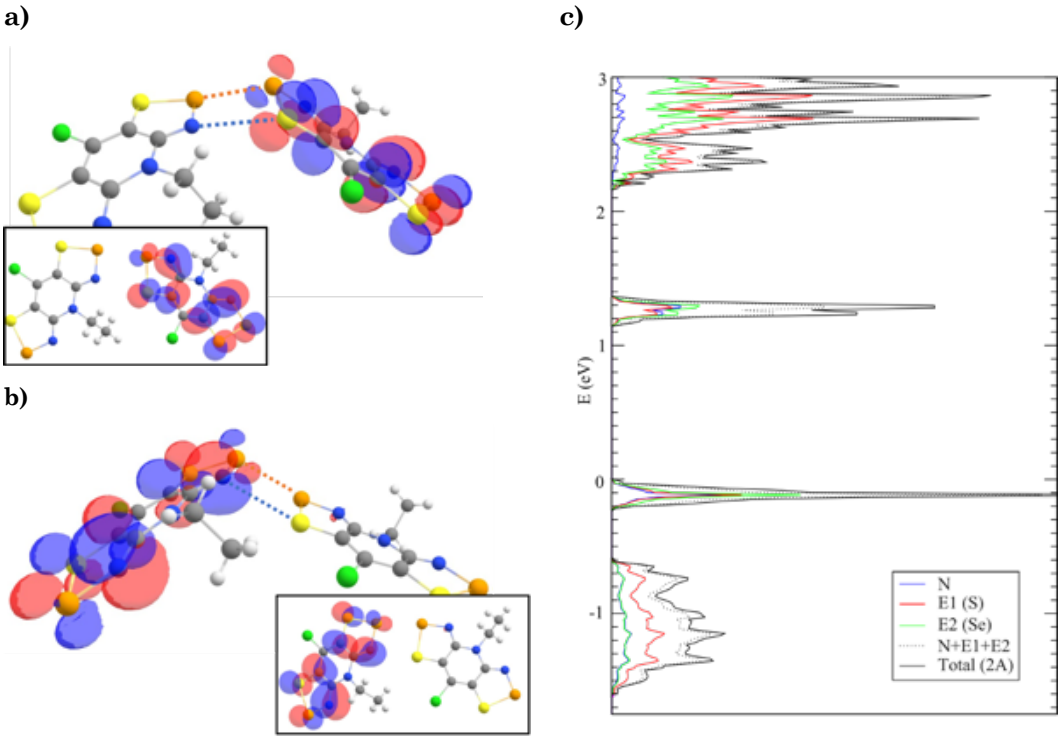

Figure 6.7. Singly occupied natural orbitals of (S,Se) of the first root at CASSCF(13,14) level of (a) 2b and (b) 2c pairs of radicals. Note that N··E_1 and E_2··E_2 contacts are depicted in orange and blue dashed lines, respectively. See inset for a top view of the two bisDTA moieties cluster (perpendicular to the π-stacking direction) (0.03 a.u isosurface). (c) Projected density of states (DOS) of (S,Se).

Document signat digitalment per: CRISTINA RONCERO BARRERO

2b and π for (S,S), (Se,S) and (Se,Se) systems; 2b and 2c for (S,Se) system in Table 6.2), which might hint at hole conduction as the most important contribution to charge transport. CASPT2 re-evaluation of H_{π} and H_{2b} shows analogous results than CASSCF values, which indicates that dynamic electron correlation can be neglected when evaluating the H_{DA} tendency (see Figure 6.6 for comparison between CASPT2 and CASSCF values of hole H_{DA}^{+} and electron H_{DA}^{-} electronic couplings).

Once all significant H_{DA} electronic couplings have been identified and evaluated, we will explore plausible structure-property correlations. As a matter of fact, structure-property effects in neutral molecule-based materials, as the four title compounds here studied, are difficult to establish due to their sensitivity to small distortions in the crystal packing (*e.g.* latitudinal and longitudinal slippage, tilting angle with respect to the π-stacking direction and interplanar distance), that can easily arise from substituents or external stimuli (*e.g.* pressure)[1,9]. The rationalization of correlations between structural parameters and macroscopic properties, such as magnetism and conductivity, is thus exceedingly difficult because there is a plethora of possible geometrical contributions to the microscopic interactions between radicals. It has been observed that N, E_1 and E_2 have a strong contribution in the valence and conduction bands, which might anticipate their importance in the definition of the conduction paths (see projected DOS for (S,Se) in Figure 6.7c and discussion in Chapter 4). Indeed, their importance can be corroborated by visual observation of the singly occupied natural orbitals of the pairs (see Figure 6.7a,b for CASSCF(13,14) singly occupied orbitals of 2c and 2b pairs for (S,Se) material and
Figure **6.8** for the remaining materials).

An analysis of all the possible distances between these N, E_1 and E_2 positions revealed that the largest H_{DA} generally occurs when the $N\cdots E_1$ distance (r_{DA}) shrinks. There is however an exception: for (S,Se), the $N\cdots E_1$ shrinking criterion cannot explain why H_{2c}^{+} increases. Instead, this enhancement might be attributed to a reduced $E_2\cdots E_2$ distance in this structure due to variations in the

Document signat digitalment per: CRISTINA RONCERO BARRERO

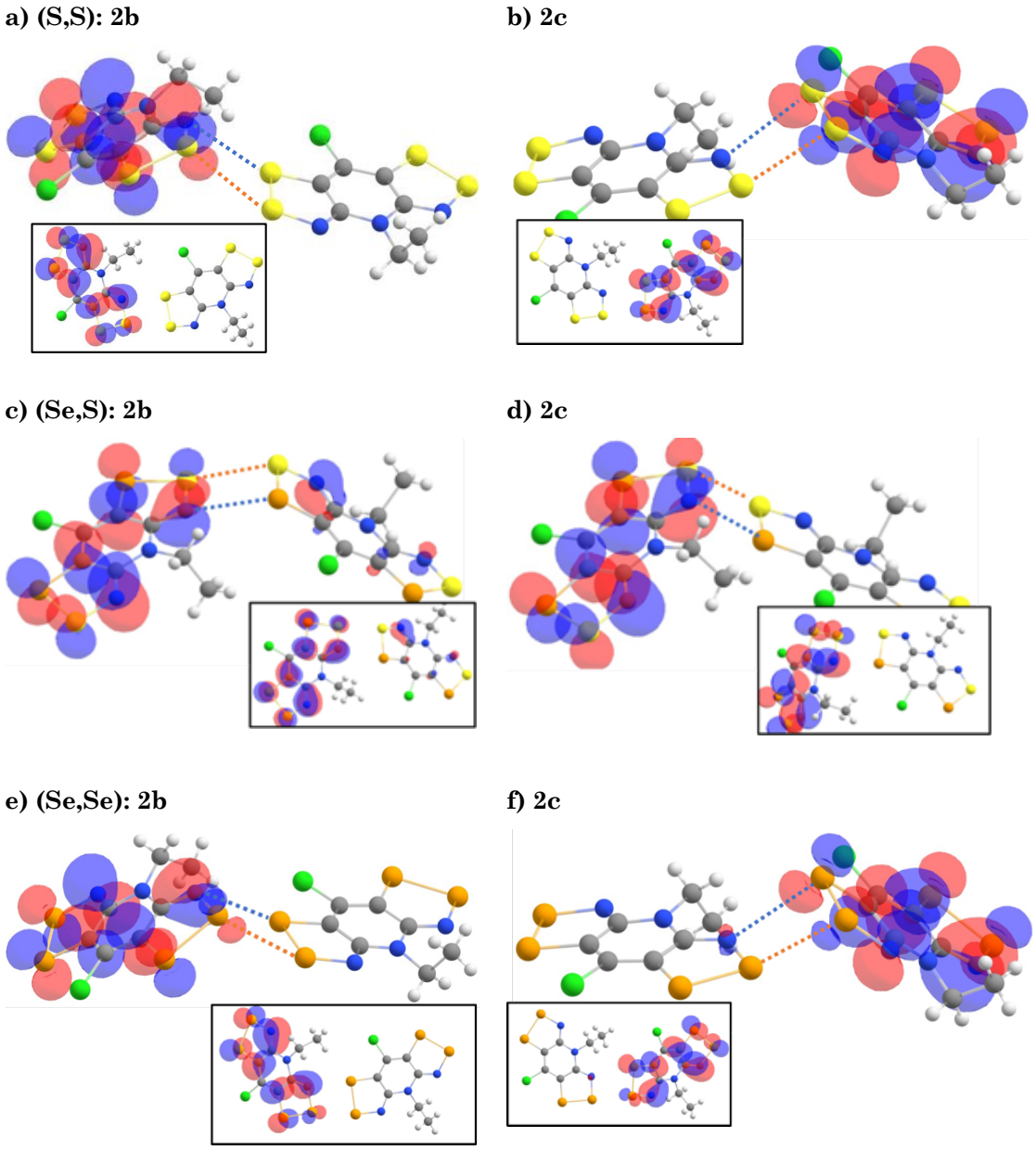

Figure 6.8. Singly occupied natural orbitals of (S,S) (a,b), (Se,S) (c,d) and (Se,Se) (e,f) materials of the first root at CASSCF(13,14) level of (a,c and d) 2b and (b,d and f) 2c pairs of radicals. Note that N··E_1 and E_2··E_2 contacts are depicted in orange and blue dashed lines, respectively. See inset for a top view of the two bisDTA moieties cluster (perpendicular to the π-stacking direction) (0.03 a.u isosurface).

Document signat digitalment per: CRISTINA RONCERO BARRERO

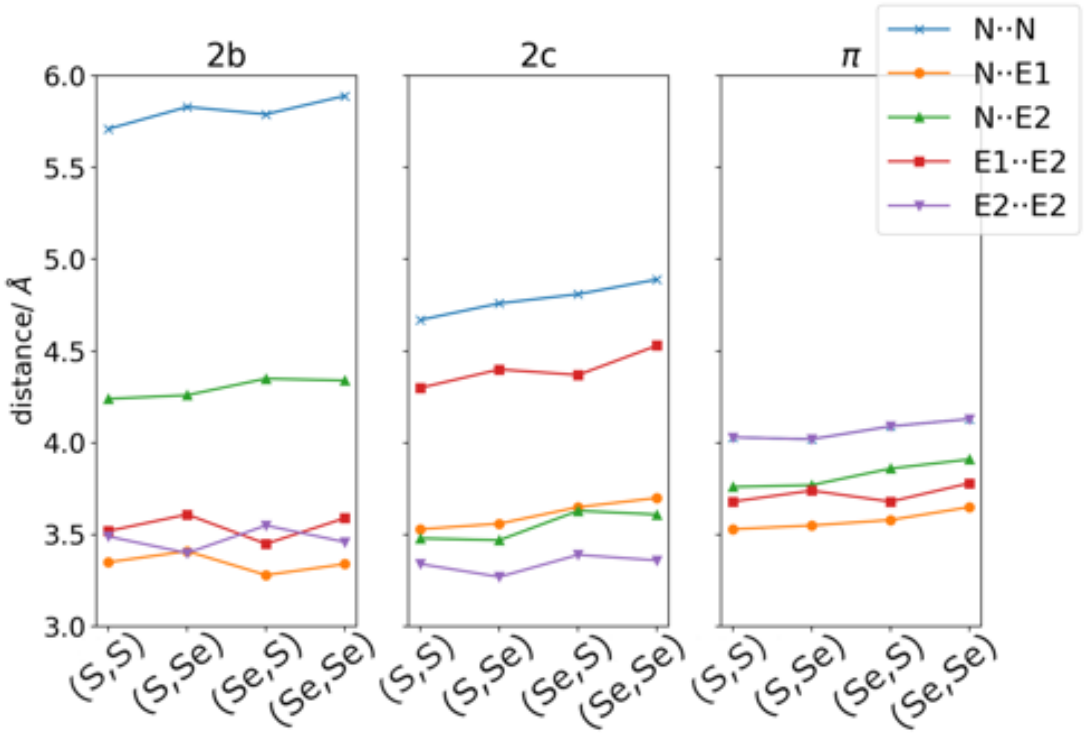

Figure 6.9. Distance analysis between the N, E1 and E2 lateral positions in the 2b, 2c and π pairs of radicals of the four bisDTA S/Se systems.

tilting angle (see r_{DA} in Table 6.2 and a complete analysis in Figure 6.9). All in all, despite the complexity of the system and the amalgam of effects, the visual inspection of the frontier orbitals gives valuable insight about the contacts in 2b, 2c and π bisDTA S/Se radical pairs that have the largest H_{DA} electronic coupling and, thus, may contribute the most to the overall conductivity.

6.1.2 λ Reorganization energy

According to our results, H_{DA} values show a slight preference for hole conduction in all four bisDTA compounds (namely, $H_{\mathrm{DA}}^{+} > H_{\mathrm{DA}}^{-}$, in Table 6.2). Calculation of λ at UB3LYP, CASSCF and CASPT2 levels of theory will provide insight on the energy cost for the radical to adapt to charge transfer in order to adjust the extra charge. The reorganization energy (λ) of the four bisDTA materials is computed using a single isolated monomer model following the 4-point scheme (Eq. 6.3), illustrated in Chapter 3 Section 3.2.1.2.

Document signat digitalment per: CRISTINA RONCERO BARRERO

$$\lambda = [E_c(R^N) + E_N(R^C)] - [E_c(R^C) + E_N(R^N)] \qquad \text{Eq.6.3.}$$

Our data evidence that the tendency shown by the H_{DA} electronic coupling is also persistent in the λ reorganization energy (see Table 6.4): calculated λ values show both a consistent preference for the cationic form ($\lambda^+ < \lambda^-$), irrespective of the method, and the same conduction ordering among bisDTA materials ($\lambda_{SS} > \lambda_{SSe} > \lambda_{SeS} > \lambda_{SeSe}$). Once more, mixed materials appear to not agree with the experimentally observed trend regarding the σ data, since λ_{SSe} and λ_{SeS} values seem to be exchanged with respect to the σ tendency. Differences on conductivity between mixed thiaselenazolyl materials will be shown to arise from the fact that charge, although delocalized due to the resonant forms of the system, may not be equally stabilized in both E_1/E_2 positions due to the different electronegativity of the chemical environment.

Table 6.4. Reorganization energies (λ, in meV) at UB3LYP, CASSCF and CASPT2 levels for the four bisDTA materials for hole (λ^+) and electron (λ^-) conductivity.

		(S,S)	**(S,Se)**	**(Se,S)**	**(Se,Se)**
λ^+	***UB3LYP***	202.43	183.93	167.77	152.45
	CASSCF	258.47	238.69	209.80	192.43
	CASPT2	219.25	200.70	196.92	183.16
λ^-	***UB3LYP***	384.15	333.63	302.79	257.34
	CASSCF	373.66	320.71	279.39	241.35
	CASPT2	454.50	381.06	355.60	295.56

A charge distribution analysis of the optimized charged and neutral geometries (R^N and R^C) shows a clear different behaviour between the two N-E_2-E_1 moieties and the remaining atoms of the bisDTA radical (see Figures 6.10 and 6.11 for donor and acceptor charge distributions in hole charge transfer). Changes on the atomic Mulliken charges are mostly localized on the two N-E_2-E_1

Document signat digitalment per: CRISTINA RONCERO BARRERO

moieties (~75-84%), irrespective of the extra charge being hole or electron. This hints at a preference for lateral charge transfer as observed in the previous H_{DA} analysis. Further, it can be observed that (S,S) and (Se,Se) materials present an equivalent charge distribution (see Figure 6.11), which does not hold for mixed compounds. In fact, mixed materials exhibit the largest charge values when Se is in the E_2 position (-1.41 in the two N-E_2-E_1 groups for (S,Se) *vs.* 0.66 in (Se,S)), which might explain the observed difference between the λ reorganization energy in both mixed bisDTA compounds (see Figure 6.10).

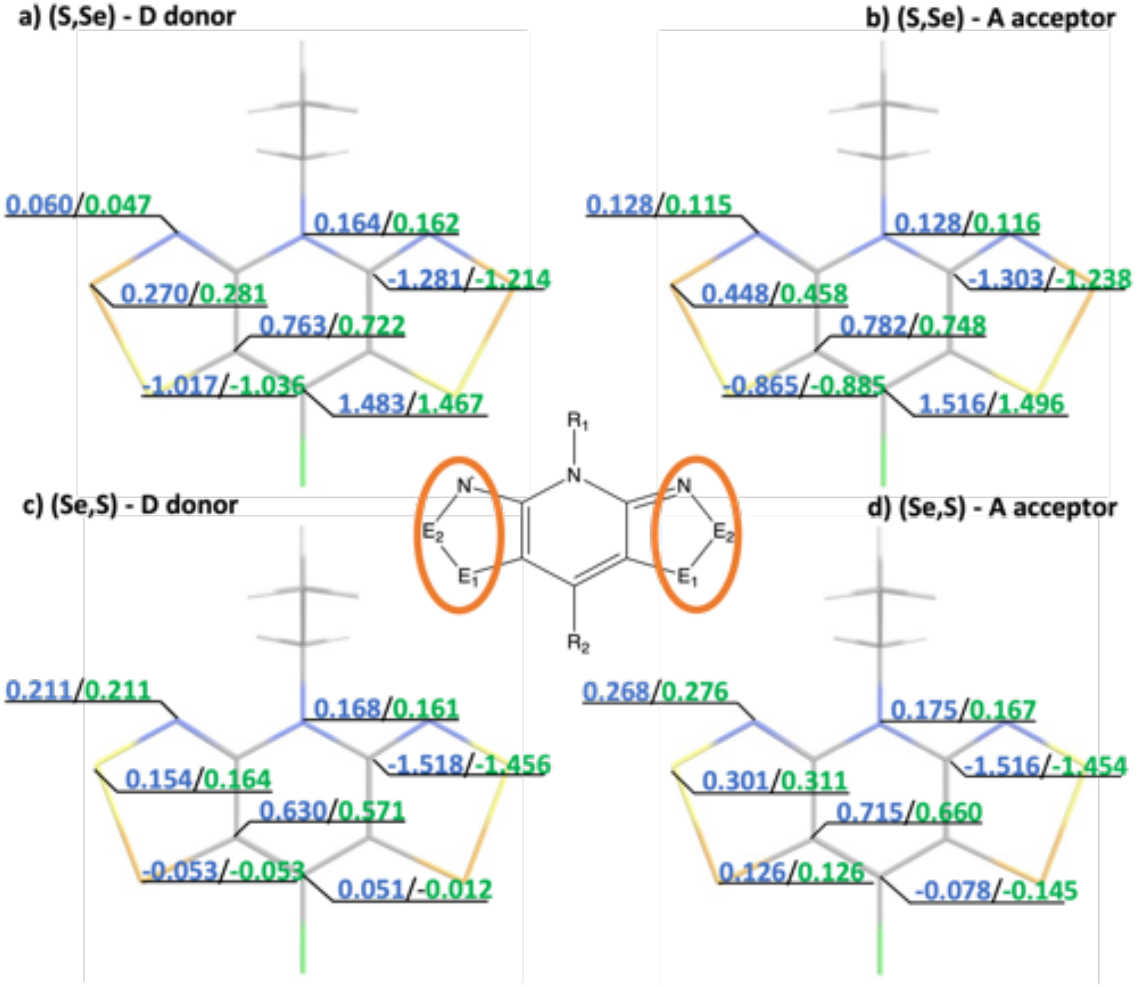

Figure 6.10. Atomic Mulliken charge analysis of the neutral (in blue) and charged (in green) geometries (R^N and R^C, respectively) of donor (D) in (a) and (c) and acceptor (A) in (b) and (d) sites for hole charge transfer. In the figure (S,Se) (top row) and (Se,S) (second row) are shown. Main changes between systems are localized in N-E_2-E_1 atoms, see encircled atoms in orange in the central image.

Document signat digitalment per: CRISTINA RONCERO BARRERO

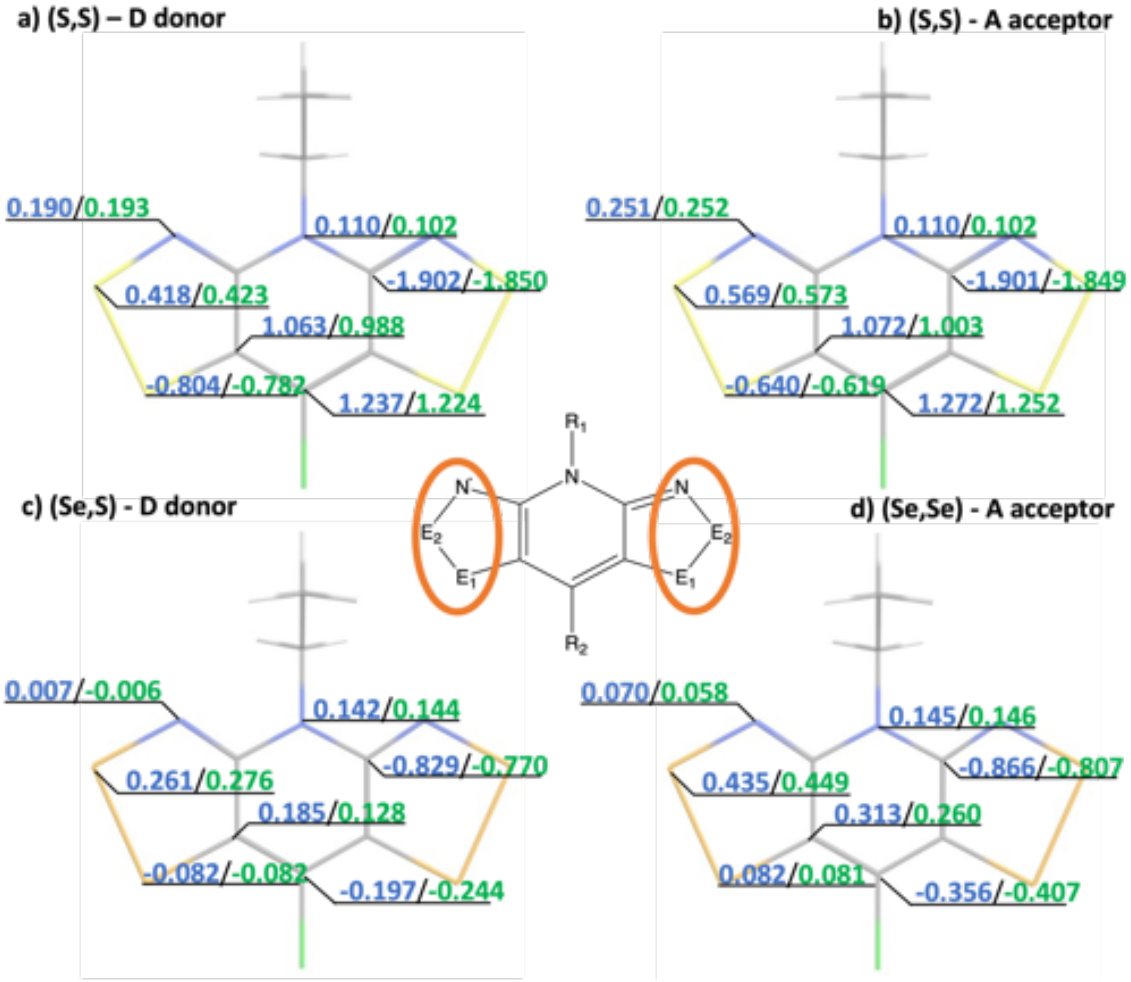

Figure 6.11. Atomic Mulliken charge distribution of the neutral (in blue) and charged (in green) geometries (R^N and R^C, respectively) of donor (D) in (a) and (c) and acceptor (A) in (b) and (d) sites for hole charge transfer. In the figure (S,S) (top row) and (Se,Se) (second row) are shown. Main changes between systems are localized in N-E_2-E_1 atoms, see encircled atoms in orange in the central image.

6.2. Marcus rate constants and Conduction paths

Once we have computed all the relevant λ and H_{DA} parameters of the different A···D radical pairs, the k_{DA} rates are calculated as:

$$k_{DA} = \frac{2\pi}{\hbar}\frac{1}{\sqrt{4\pi\lambda k_B T}}\langle|H_{DA}|^2\rangle_{TS} e^{-\lambda/4k_B T} \qquad \text{Eq. 6.4.}$$

Document signat digitalment per: CRISTINA RONCERO BARRERO

Table 6.5. Marcus rate constants (in THz at 300K) for hole (k_{DA}^{+}) and electron (k_{DA}^{-}) charge transfer obtained according to Eq. 6.4, using CASSCF parameters listed in Tables 6.2 and 6.4.

	(S,S)		(S,Se)		(Se,S)		(Se,Se)	
	k_{DA}^{+}	k_{DA}^{-}	k_{DA}^{+}	k_{DA}^{-}	k_{DA}^{+}	k_{DA}^{-}	k_{DA}^{+}	k_{DA}^{-}
π	2.72	0.53	3.54	1.12	16.51	3.01	14.72	2.60
2b	17.68	3.20	35.74	10.16	99.69	33.00	132.67	56.36
2c	1.24	1.34	13.36	2.12	0.73	0.47	3.64	6.69

The resultant k_{DA} rate constants (see values in Table 6.5 according to Eq. 6.4) preserve the same trends already observed when individually analysing λ and H_{DA}: (1) rate constants increase as the Se-content increases from (S,S) to (Se,Se), (2) a preference for hole conduction is observed by comparing the rate constants for both hole (k_{AD}^{+}) and electron (k_{AD}^{-}) charge conductions at 300K, and (3) the 2b pair of bisDTA radicals prevails as the most probable direction for the charge hopping mechanism in all four materials. Strikingly, mixed thiaselenazolyl materials show different effects due to the Se position. While E_1-substitution in (Se,S) enlarges k_{2b}^{+} (and k_{π}^{+}) rate constants, it can be observed that Se in E_2 opens additional paths for conduction (k_{2c}^{+}) in (S,Se) and favours the electron migration with nearly degenerate k_{2b}^{+}, k_{π}^{+} and k_{2b}^{-}, k_{π}^{-} values. Furthermore, comparison of the largest k_{DA} rate constants of each system shows that the observed tendency for charge transport feasibility is $k_{2b,SS}^{+} < k_{2b,SSe}^{+} < k_{2b,SeS}^{+} < k_{2b,SeSe}^{+}$. Re-evaluation of the 2b and π rate constants at CASPT2 level shows that rate constants do not depend substantially on the dynamic electronic correlation (see Figure 6.12 for rate constants of hole and electron charge transfer).

The direction of the charge transport is important in order to describe the components of the mobility tensor in a crystalline material. It can be inferred from the most significant values of k_{DA} rate constants. Visual representation of the relevant charge transport orientation within the crystal packing (see Figure

Document signat digitalment per: CRISTINA RONCERO BARRERO

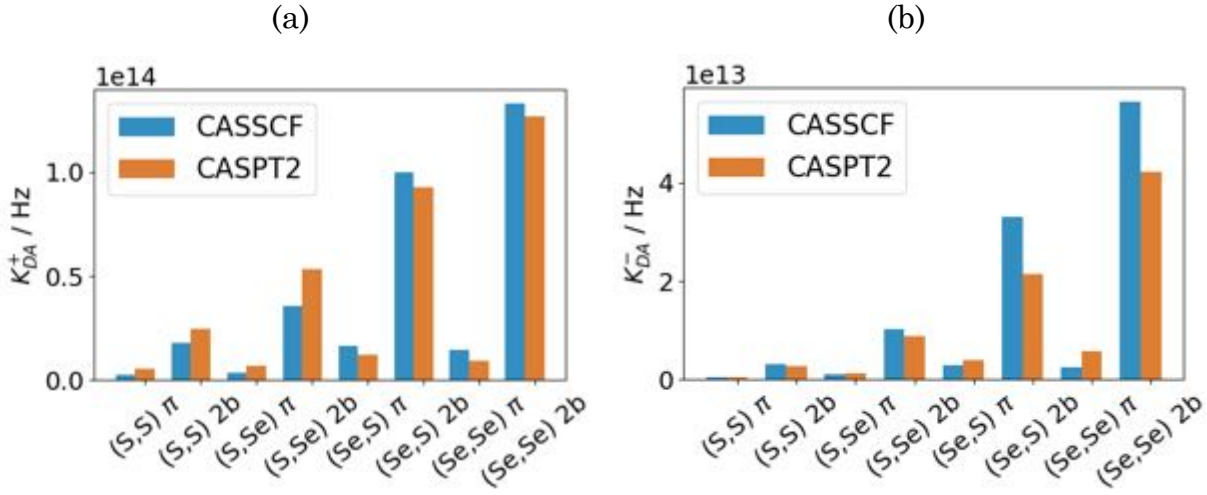

Figure 6.12. Comparison between CASPT2 and CASCF for rate constants when there is either (a) k^{+}_{DA} hole , or (b) k^{-}_{DA} electron charge transfer.

6.13), hereafter the so-called conduction paths, shows that conductivity in the bisDTA crystals might be anisotropic with a preference for the *ab*-plane directions. According to k_{DA}, the conduction paths for (S,S), (Se,S) and (Se,Se) materials exhibit quasi-isolated *ab*-planes, since k_{π} is one order of magnitude smaller in all bisDTA compounds (see Figure 6.13a). On the other hand, for (S,Se), the 2D conduction paths defined by k_{2b} become a 3D conduction network thanks to k_{2c} (see k_{2b} (in orange) and k_{2c} (in blue) in Figure 6.13b).

The study presented in Chapter 5 concerning the magnetism of all four bisDTA derivatives has disclosed the relevant magnetic couplings using an equivalent bottom-up analysis. Regarding the magnetic interactions, it was observed that $E_2 \cdots E_2$ distances were key in order to rationalize the magnitude of the J_{AB} magnetic interaction. In general, the largest magnetic couplings were found in the 2c direction of the material. Results showed that all four bisDTA-derivatives present a 3D magnetic topology with a relatively strong (in comparison with the stacking exchange) *ab*-component in the magnetic coupling propagation. Thus, while deviations from the ideal π-stack crystal packing have been regarded as a disadvantage to the enhancement of the magnetic and conductive properties of this kind of material, it can be here observed that the distorted π-stack crystal packing favours their coexistence in the direction of the

Document signat digitalment per: CRISTINA RONCERO BARRERO

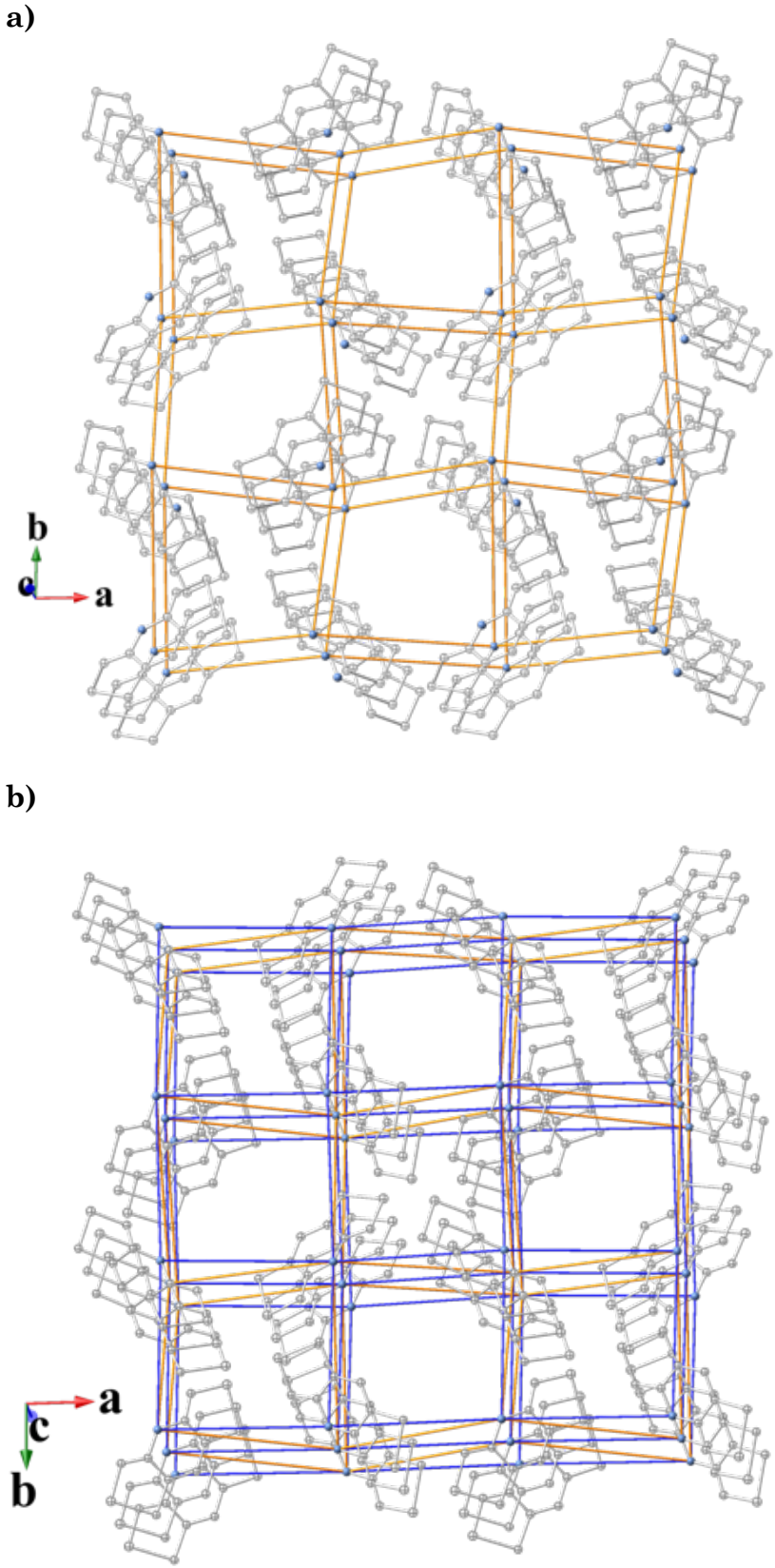

Figure 6.13. Schematic representation of (a) 2D conduction paths for (S,S), (Se,S) and (Se,Se) materials, and (b) 3D conduction network for (S,Se) compound. Colour code: k_{2b} in orange and k_{2c} in blue.

Document signat digitalment per: CRISTINA RONCERO BARRERO

ab-plane of the material. Interestingly, the contribution to conductivity along the π-stack in the crystal (provided by k_{π}^{+} and k_{π}^{-}) is not the dominant conduction path as could be expected for organic π-stacked molecule-based materials. This is remarkable indeed since it illustrates the importance of a detailed analysis of all possible donor···acceptor contacts between radicals, which will be eventually responsible for the conduction paths within the crystal structure.

6.3. From the cluster model to the macroscopic crystal: Electric conductivity

Experimental conductivity measures on the bisDTA-derivates systems of interest were performed using powder samples[1]. Therefore, the measured conductivity of a polycrystalline system does not bring any information regarding the anisotropy of the tensor property and will be closer to an averaged estimation between all possible directions. This means that instead of $\bar{\bar{\sigma}}$, we will report the conductivity as a σ scalar. In order to compare the computational data here reported with the experimental evidence, mobility has been estimated using Eq 6.5 with an effective weighted mean k_{DA} ($p_A = \frac{k_{DA}}{\sum k_{DA}}$) between relevant pairwise rates, under an electric field (E) of 10^4 V/m, which in the absence of directionality, has been set parallel to the effective k_{DA}.

$$\mu = \frac{1}{E}\sum_{A>D} p_A k_{DA} \vec{r}_{DA} \frac{\vec{E}}{E} \quad , \qquad \text{Eq. 6.5.}$$

Resultant mobilities (μ) range from 0.1 to 3.9 m^2/Vs, as expected for a hopping semiconductor (Table 6.6)[3] and retain the observed tendency in the predominant k_{DA}. Both, hole and electron μ (μ^+ and μ^-, respectively) increase with the Se content from (S,S) to (Se,Se). Specifically, the E_1-substituted (Se,S) thiaselenazolyl shows the largest mobilities compared to (S,Se) (2.8 vs. 1.0 m^2/Vs for μ^+ and 1.0 vs. 0.3 m^2/Vs for μ^-, according to Table 6.6). Interestingly, despite that μ^+ shows a clear dominance in all bisDTA, the relative contribution of μ^-increases from ~14% (μ^-/μ^{total}, assuming $\mu^{total} = \mu^+ + \mu^-$) in (S,S) to ~29% in

Document signat digitalment per: CRISTINA RONCERO BARRERO

Table 6.6. Computed hole (μ^+) and electron (μ^-) mobility.

	μ^- (m²/Vs)	μ^+ (m²/Vs)
(S,S)	0.08	0.48
(S,Se)	0.26	0.93
(Se,S)	0.96	2.78
(Se,Se)	1.57	3.82

(Se,Se) material. Previous analysis of k_{DA} showed that $k^-_{DA,SSe}$ and $k^+_{DA,SSe}$ in 2b and π were almost degenerate. However, taking into consideration the present analysis (*i.e.,* distance between sites and the magnitude of k_{DA}), the observed potential improvement of the electron migration has not translated to a larger mobility μ^-_{SSe}= 0.3 m²/Vs, compared to μ^-_{SeS} = 1.0 m²/Vs.

Analysis of the electronic band structure reported in Chapter 4 for the title bisDTA-derivatives showed that all four bisDTA S/Se materials presented similar bands with dispersion between 0.2-0.3 eV, being the dispersion of (Se,S) bands slightly larger than the rest of compounds, and band gaps around 1.15-1.4 eV. Differences between systems happened to be insufficient to explain, from a band model perspective, the observed conductivity. However, those differences have been proven to be relevant in the density of charge carriers (ρ_c) analysis.

$$\rho_c = 2\left(\frac{k_B T}{2\pi\hbar^2}\right)^{3/2}(m_e m_h)^{3/4}\, e^{-E_g/2k_B T} \qquad \text{Eq. 6.6.}$$

Charge carrier densities (ρ_c) have been computed using Eq. 6.6 and the reported E_g band gaps in Chapter 4 for all the different explored magnetic solutions (see Figure 6.14 for a schematic representation of the six open-shell magnetic solutions, and Table 6.7 for values).

Unlike μ, which is favoured by E_1-Se-substitution, computed ρ_c shows generally a greater concentration of charge carriers when Se is located in the E_2 position (see Figure 6.15). This trend has shown to be almost independent of the

Document signat digitalment per: CRISTINA RONCERO BARRERO

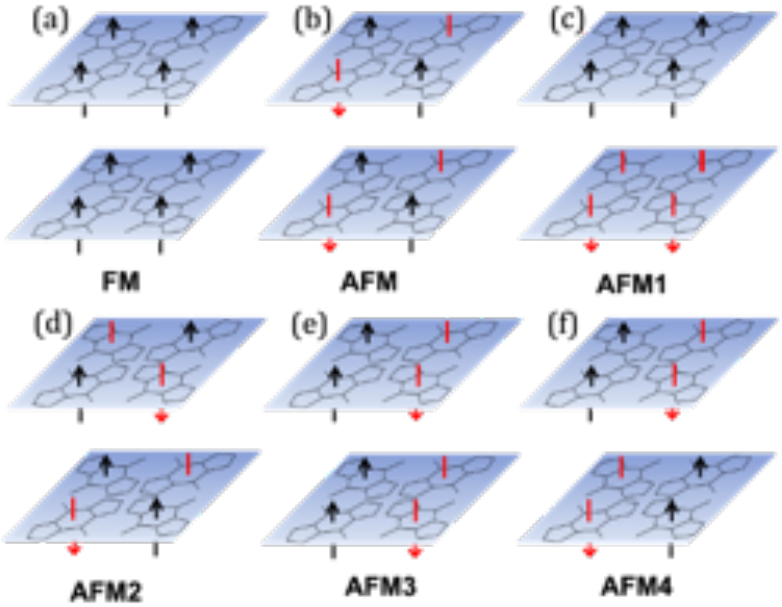

Figure 6.14. Schematic representation of the spin arrangement of the calculated (a) FM and (b)-(f) AFM# electronic solutions. Planes are perpendicular to the columns depicted in Figure 2.3b, i.e. to the direction of π-stacking, and contain the centre of mass of the molecules depicted (ab-plane). Radicals are included to guide the eye. Spin-up and spin-down depicted in black and red, respectively.

magnetic solution with the only exception of AFM3 solutions in which the small band gaps of (S,Se) and (Se,S) systems (1.27 and 1.24 eV, respectively) reverse the trend observed with the other solutions.

Finally, mean conductivities are computed ($\sigma = \rho_c q \mu$) for both, hole σ^+ and electron σ^- conduction. Altogether, hole conductivities at 300K under a 10^4 V/m electric field are in agreement with the experimental data (see σ^+ and σ^{Exp} in Table 6.7). The take-home message is that Se-substitution affects both, charge mobility and density of carriers, depending on the position, and that only when both effects are taken into account the experimental tendency on σ is met. Final results show that improvement in conductivity by Se-substitution in bisDTA materials is, broadly speaking, due to two complementary effects: i) Se substitution (irrespective of the E_1/E_2 position) has proven to favour charge migration when it does not potentially distort the geometry increasing the distance between sites, and ii) when Se is placed in the E_2 position, the band gap

Document signat digitalment per: CRISTINA RONCERO BARRERO

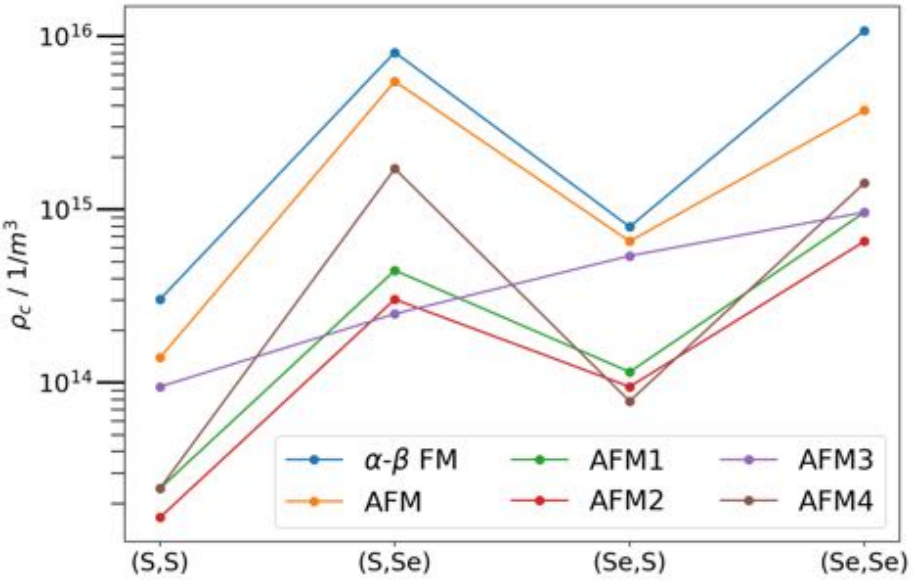

Figure 6.15. Density of charge carriers (ρ_c) tendency for the four bisDTA materials at each magnetic solution. See notation in Figure 6.14.

Table 6.7. Band gap (E_g), density of charge carriers (ρ_c), computed hole (σ^+) and electron (σ^-) conductivity and experimental (σ^{Exp}) at 300K and under electric field E=10^4 V/m. Band gaps have been extracted from the AFM magnetic solution presented in Chapter 4 for all four bisDTA.

	E_g (eV)	ρ_c (1/m³)	σ^- (S·cm^{-1})	σ^+ (S·cm^{-1})	σ^{Exp} (S·cm^{-1})[a]
(S,S)	1.34	$1.39 \cdot 10^{14}$	$1.78 \cdot 10^{-7}$	$1.08 \cdot 10^{-6}$	$3.20 \cdot 10^{-6}$
(S,Se)	1.15	$5.97 \cdot 10^{15}$	$2.49 \cdot 10^{-5}$	$8.91 \cdot 10^{-5}$	$1.00 \cdot 10^{-4}$
(Se,S)	1.26	$7.13 \cdot 10^{14}$	$1.10 \cdot 10^{-5}$	$3.17 \cdot 10^{-5}$	$2.20 \cdot 10^{-5}$
(Se,Se)	1.17	$3.73 \cdot 10^{15}$	$9.37 \cdot 10^{-5}$	$2.28 \cdot 10^{-4}$	$3.00 \cdot 10^{-4}$

a) Data from ref. 1

shrinks and conductivity is enlarged thanks to an increase of the available charge carriers.

6.4. Conclusions

The incorporation of heavy heteroatoms is a common experimental strategy used to improve the electric and magnetic properties of organic radical molecular materials. Due to the neutral nature of the radical building blocks that reduces the crystal packing forces to dispersion or weak electrostatic interactions, Se-

Document signat digitalment per: CRISTINA RONCERO BARRERO

substitution does not just affect the electronic structure of the material but also modifies the crystal arrangement. The resultant crystal structure of distorted π-stack columns might be thought as to hinder the charge migration along the stacking axis. However, this distorted crystal packing is here detected to improve lateral donor···acceptor radical interactions. According to our results, computed electronic couplings (H_{DA}) evidence the predominance of these lateral interactions, which might be motivated by close N-E_1 and E_2-E_2 intermolecular contacts.

Systematic calculation and analysis of relevant terms to interpret the electric mobility and conductivity using a simplified hopping model using pairs of radicals in the crystal structure have been carried out to obtain the relevant conduction paths for each one of the bisDTA-derivatives. Electronic coupling (H_{DA}) and reorganization energy (λ) consistently show a preference for hole conduction in all four selected bisDTA compounds. Conduction paths suggest an anisotropic conduction with larger charge transport rates (k_{DA}) along the ab crystallographic axes, the here named 2b direction. The largest Marcus rates (k_{2b}^{+}) increase with the Se content along the series: $k_{2b,SS}^{+} < k_{2b,SSe}^{+} < k_{2b,SeS}^{+} < k_{2b,SeSe}^{+}$. Comparison between mixed thiaselenazolyl materials indicates that (1) E_1-Se-substitution enlarges k_{DA} but the overall picture of 2D conduction paths remains, and (2) Se in the E_2 position opens additional charge transfer paths (namely 2c) that interconnect the ab-layers along the c-axis (without entailing a direct π-stacking charge transfer path), and thus the conduction path becomes a 3D network. Interestingly enough, the contribution to conductivity along the π-stack in the crystal is not the dominant conduction path as usually expected, which thus shows the importance of a detailed analysis of the particular donor···acceptor radical terms associated to the possible conduction paths in the crystal structure.

The estimation of charge carrier density (ρ_c) shows a significant increase when Se is in the E_2 position. As a result, when charge density and rate constants are accounted for, our computed hole conductivities (σ^{+}) are in

Document signat digitalment per: CRISTINA RONCERO BARRERO

agreement with experimental data since $\sigma_{SS}^{+} < \sigma_{SeS}^{+} < \sigma_{SSe}^{+} < \sigma_{SeSe}^{+}$. Therefore, final conductivities corroborate the preference for hole conduction suggested in the analysis of k_{DA} rate constants for charge transfer.

In conclusion, Se substitution not only favours charge migration but also can induce small structural distortions. The resulting distorted crystal packing can then modify the conduction paths and affect the band dispersion and band gap, and hence the carriers available for conduction. Our computational analysis on the title bisDTA compounds discloses a plethora of effects relevant to interpret their experimental conductivity, which would have not been possible to infer from the small geometrical changes that precede them. Overall, the bottom-up analysis here presented has been shown to be a feasible realizable strategy to study conductivity in organic open-shell molecular materials.

6.5. References

1 C. M. Robertson et al., "Enhanced conductivity and magnetic ordering in isostructural heavy atom radicals," Journal of the American Chemical Society, vol. 130, no. 26, pp. 8414–8425, 2008, doi:10.1021/ja801070d.

2 Marcus, R. A. (1993). Electron Transfer Reactions in Chemistry: Theory and Experiment (Nobel Lecture). Angewandte Chemie International Edition in English, 32(8), 1111–1121. https://doi.org/10.1002/anie.199311113

3 Oberhofer, H., Reuter, K., & Blumberger, J. (2017). Charge Transport in Molecular Materials: An Assessment of Computational Methods. Chemical Reviews, 117(15), 10319–10357 . https://doi.org/10.1021/acs.chemrev.7b00086

4 Coropceanu, V., Cornil, J., da Silva Filho, D. A., Olivier, Y., Silbey, R., & Brédas, J. L. (2007). Charge transport in organic semiconductors. In Chemical Reviews (Vol. 107, Issue 4, pp. 926–952). https://doi.org/10.1021/cr050140x

5 A. Bondi, "van der Waals Volumes and Radii," The Journal of Physical Chemistry, vol. 68, no. 3, pp. 441–451, Mar. 1964, doi: 10.1021/j100785a001.

6 Malmqvist, P. Å., Roos, B. O., & Schimmelpfennig, B. (2002). The restricted active space (RAS) state interaction approach with spin–orbit coupling.

Document signat digitalment per: CRISTINA RONCERO BARRERO

Chemical Physics Letters, 357(3–4), 230–240. https://doi.org/10.1016/S0009-2614(02)00498-0

7 Koopmans, T. (1934). Über die Zuordnung von Wellenfunktionen und Eigenwerten zu den Einzelnen Elektronen Eines Atoms. Physica, 1(1–6), 104–113. https://doi.org/10.1016/S0031-8914(34)90011-2

8 Kushida, T., Shirai, S., Ando, N., Okamoto, T., Ishii, H., Matsui, H., Yamagishi, M., Uemura, T., Tsurumi, J., Watanabe, S., Takeya, J., & Yamaguchi, S. (2017). Boron-Stabilized Planar Neutral π-Radicals with Well-Balanced Ambipolar Charge-Transport Properties. Journal of the American Chemical Society, 139(41), 14336–14339. https://doi.org/10.1021/jacs.7b05471

9 Leitch, A. A., Lekin, K., Winter, S. M., Downie, L. E., Tsuruda, H., Tse, J. S., Mito, M., Desgreniers, S., Dube, P. A., Zhang, S., Liu, Q., Jin, C., Ohishi, Y., & Oakley, R. T. (2011). From magnets to metals: The response of tetragonal bisdiselenazolyl radicals to pressure. Journal of the American Chemical Society, 133(15), 6050–6060. https://doi.org/10.1021/ja200391j

Document signat digitalment per: CRISTINA RONCERO BARRERO

Chapter 7. Conclusions

Based on the objectives proposed in the introduction of this PhD dissertation and the partial conclusions presented along Chapters 4, 5 and 6, a series of general conclusions have been extracted.

- Periodic Hybrid DFT calculations have proven to be a reliable tool for the study of the electronic structure of the four bisDTA S/Se molecular materials formed by neutral open-shell radicals. Overall, the results obtained describe the four systems as paramagnetic semiconductors with a *ca.* 1.3eV indirect band gap. The characterized ground state found after the study of different spin-unrestricted magnetic solutions is open-shell and consistent with the experimentally observed magnetic behaviour of the systems. However, the band structure of the system is not sufficient to interpret the trends observed in the conductivity of the materials. A closed-shell metallic solution has been found near in energy (~250 meV per chemical formula unit) in all four materials, suggesting that the conductivity might have contributions from band and hopping mechanisms. Analysis of the projected density of states shows that the band gap in the four bisDTA-derivatives arises mainly from the contributions of the atoms in N-E_2-E_1 positions, which hints at their importance in the posterior description of the charge transport process. Two further conclusions can be drawn from analysing the charge and spin distributions: i) the crystal packing of distorted π-stacked columns is the result of attractive/repulsive interactions between the E_2 and N atoms, and ii) the spin distribution shows that bisDTA radicals of the four systems can be considered as a S=½ effective spin particle, which allows

Document signat digitalment per: CRISTINA RONCERO BARRERO

the study of their magnetic interactions by means of the two-body HDVV spin Hamiltonian.

- Following a First Principles Bottom-Up working strategy (FPBU) the intricate magnetic topologies of the four bisDTA S/Se materials have been characterized. All four materials present, at 100K, magnetic topologies consisting of ferromagnetic FM planes, which either (i) are connected by means of antiferromagnetic AFM interactions through the π-stacking directions, resulting in 3D topologies for (S,S), (Se,S) and (Se,Se) systems, or (ii) remain isolated resulting in a 2D FM magnetic topology, as in the (S,Se) material. The resultant macroscopic magnetic properties calculated by means of crystallographic data characterised at 100 K, namely magnetic susceptibility (χT) and critical temperature (T_C), proves to be only capable to reproduce correctly the experimental data of (S,S) and (Se,S) compounds. However, the results of the present model do not reproduce quantitatively the experimental magnetisation observed at low temperature for (S,Se) and (Se,Se). Our results also reveal that, in E_2-Se-substituted systems, crystallographic data below the T_C critical temperature are exceedingly important in order to compute the microscopic contributions responsible for the magnetic properties.

- It has been proven that, for systems for which crystallographic data is not available, PBE-D2 crystal optimization is a useful tool to evaluate the thermal effects in the geometry and microscopic magnetic interactions. Magnetic topologies using PBE-optimized geometries for (S,Se) and (Se,Se) recover the expected FM ground state, which has been further corroborated by means of the P_{ij} analysis (i.e. in terms of spin correlation). The high sensitivity of the J_{AB} value upon structural changes for these materials has been also assessed using magneto-structural correlation maps. Specifically, the mapping of the π-stacking magnetic interaction (J_π) versus the longitudinal(y)-slippage and the interplanar distance (δ) has shown that, in fact, the geometry of the π-stacking pair of (Se,Se)

Document signat digitalment per: CRISTINA RONCERO BARRERO

radicals lies close to a FM and AFM boundary region, in which J_{π} can transition from AFM to FM (and *vice-versa*). It is thus concluded that small perturbations in the crystallographic structure can affect dramatically the overall magnetic picture of the material.

- Evaluation of the reorganization energies (λ) and electronic couplings (H_{DA}) of all four bisDTA S/Se materials shows a preference for hole conduction (i.e. rate constants for hole charge transfer are larger than for electron charge transport, $k^+ > k^-$). Conduction paths defined in terms of k_{DA} Marcus rate constants show that the materials exhibit an anisotropic conduction with larger k_{DA} in the ab-plane (k_{2b}^+). Strikingly, and contrary to the expected behaviour for these materials formed by the stacking of planar organic molecules, the contribution along the π-stack is not the dominant conduction path.

- The experimental tendency on conductivity observed in bisDTA materials due to the S/Se substitutions (namely, $\sigma_{SS} < \sigma_{SeS} < \sigma_{SSe} < \sigma_{SeSe}$) is only recovered when both density of charge carriers (ρ_c) and mobilities (μ) are considered. Results prove that Se-substitution favours the charge migration irrespective of the E_1/E_2 position if it does not produce geometry distortions that play against it, and that, when placed in the E_2 position, Se-substitution enhances conductivity by increasing the number of available charge carriers.

- The resultant calculated electric conductivities prove that Marcus rate equation is valid for the description of open-shell molecular magnetic semiconductors. Furthermore, it has been demonstrated that the approximations employed, such as the Energy-Splitting-in-Dimer method for the evaluation of the H_{DA} electronic couplings (Figure 3.6 and Eq. 6.2), and the calculation of λ reorganisation energy using the 4-points scheme model (Figure 3.7 and Eq. 6.3), correctly portrait conductivity and reproduce the expected trends in single-component radical semiconductors.

Document signat digitalment per: CRISTINA RONCERO BARRERO

- Distortions of the crystallographic arrangement of all four bisDTA S/Se materials (*e.g.* latitudinal and longitudinal slippage, tilting angle with respect to the π-stacking direction and the interplanar distance (δ) have been regarded as to hinder the charge migration along the π-stacking direction. Our computed electric conductivities do support this educated guess. However, while these distortions affect negatively the charge migration along the π-stacking direction, they have the side effect of improving lateral interactions. Therefore, magnetic topologies and conduction paths become 3D by means of these enhanced lateral contacts.

- The proposed methodology combining periodic and cluster model approaches provides a useful scheme to investigate the electronic structure and properties of this kind of organic multifuncional materials formed by neutral open-shell molecular entities. The open-shell nature of the molecular building blocks along with the neutral character of the constituent molecular entities makes these systems a challenge for quantum chemistry methods and models. The competition between charge localisation (which would enhance magnetism) and charge transport (which would enhance conductivity) along with the neutral character of the constituent molecular entities (which reduce the cohesive forces in the crystal to dispersion or weak N···S / N···Se electrostatic interactions) is a difficult scenario for present day electronic structure methods. However, analysis of the frontier orbitals associated to the unpaired electrons provide useful information to establish the topology of the relevant exchange coupling mechanism and conducting paths governing their interesting interrelated properties.

Document signat digitalment per: CRISTINA RONCERO BARRERO

PART III. APPENDIX

Document signat digitalment per: CRISTINA RONCERO BARRERO

Document signat digitalment per: CRISTINA RONCERO BARRERO

A1. Bisdithiazolyl derivatives

List of some of the compounds that belongs to the family of Bisdithiazolyl-based materials. Compounds have been listed in different groups classified by the functional group of the central ring.

A1.1 Pyridine-bridged bisDTA

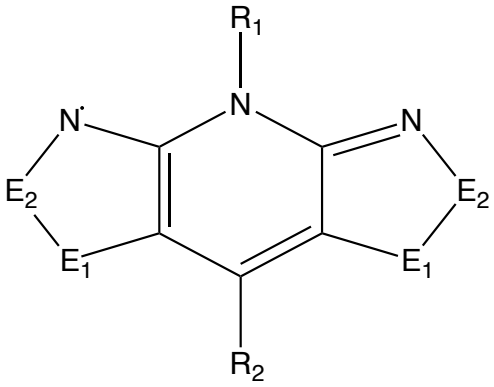

(E_1,E_2)	R
1. (S,S)	a) R_1=Me, R_2=Cl
2. (S,Se)	b) R_1= Me, R_2=H
3. (Se,S)	c) R_1= Et, R_2=Cl
4. (Se,Se)	d) R_1= Pr, R_2=Cl
	e) R_1= Cl, R_2=Me
	f) R_1=H, R_2= Me
	g) R_1=Me, R_2= Me
	h) R_1=Ph, R_2= Me
	i) R_1=Pr, R_2= F
	j) R_1=Bu, R_2= F
	k) R_1=Pn, R_2= F
	l) R_1=Hx, R_2= F
	m) R_1=Et, R_2=Ph
	n) R_1=Me, R_2=Ph
	o) R_1= Et, R_2=Br
	p) R_1= Et, R_2=H
	q) R_1= Et, R_2=F
	r) R_1=H, R_2=Cl
	s) R_1=Me, R_2=F
	t) R_1=CH_2CF_3, R_2=Cl
	u) R_1=Et, R_2=Me
	v) R_1=Et, R_2=Br

Synthetized materials:

1a: [1]–[4]	1l:[9], [12]	1p:[18]	3c: [9]
1b: [1], [5], [6]	1n: [13]	3p: [18]	1s: [21]
1c: [2], [3], [7]–[10]	1m: [13]	4p: [18]	1q: [23]
1d:[2]	4n: [13]	2c: [7]–[9], [17], [19]	2d: [19]
1e:[11]	4m: [13]	1q: [9], [20], [21]	2t: [19]
1f:[11]	3b:[5], [6]	3c: [8]	2u: [19]
1g: [11]	4b:[5], [6]	1r: [3]	2o: [19]
1h: [11]	4c:[8], [9], [14], [15]	2p: [22]	2v: [19]
1i: [12]	4o:[14]	2s: [17]	
1j:[12]	2b: [6], [16], [17]	2a: [4]	

Document signat digitalment per: CRISTINA RONCERO BARRERO

1k: [12]

3a: [4]
4a: [4]

A1.2 Pyrazine-bridged bis DTA

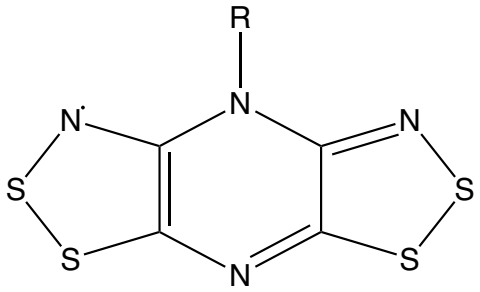

Synthetized materials:

1. R= Et [24]
2. R= Me[25]

A1.3 Semiquinone

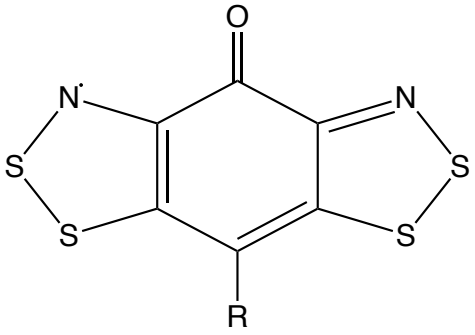

1. R= F
2. R= OMe
3. R= OAc
4. R= SMe
5. R= Cl
6. R=H
7. R= NO_2
8. R= Ph
9. R= Br
10. R= I

Synthetized materials:

1-4: [26], [27]
5: [28]
6: [29], [30]
7: [31]
8: [32]
9-10: [32]

Document signat digitalment per: CRISTINA RONCERO BARRERO

A1.4 Benzoquinone

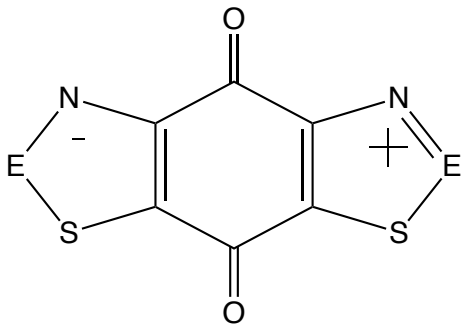

E= S [33]
E= Se[34]

[1] L. Beer *et al.*, "Structure-property trends in π-stacked dithiazolo-dithiazolyl conductors," *Chemical Communications*, no. 21, pp. 2562–2563, 2002, doi: 10.1039/b207735n.

[2] L. Beer *et al.*, "Resonance-Stabilized 1,2,3-Dithiazolo-1,2,3-dithiazolyls as Neutral π-Radical Conductors," *J Am Chem Soc*, vol. 124, no. 32, pp. 9498–9509, Aug. 2002, doi: 10.1021/ja026118s.

[3] L. Beer *et al.*, "Prototypal Dithiazolodithiazolyl Radicals: Synthesis, Structures, and Transport Properties," *J Am Chem Soc*, vol. 125, no. 47, pp. 14394–14403, Nov. 2003, doi: 10.1021/ja0371350.

[4] A. A. Leiten *et al.*, "Structure and property correlations in heavy atom radical conductors," *J Am Chem Soc*, vol. 131, no. 20, pp. 7112–7125, 2009, doi: 10.1021/ja900853t.

[5] J. L. Brusso, K. Cvrkalj, A. A. Leitch, R. T. Oakley, R. W. Reed, and C. M. Robertson, "Resonance stabilized bisdiselenazolyls as neutral radical conductors," *J Am Chem Soc*, vol. 128, no. 47, pp. 15080–15081, 2006, doi: 10.1021/ja0666856.

[6] L. Beer *et al.*, "Pressure Enhanced Conductivity in Bis-1,2,3-Thiaselenazolyl Dimers," *J Am Chem Soc*, vol. 127, no. 51, pp. 18159–18170, Dec. 2005, doi: 10.1021/ja055122b.

[7] C. M. Robertson *et al.*, "Ferromagnetism in a heavy atom heterocyclic radical conductor," *J Am Chem Soc*, 2007, doi: 10.1021/ja076841o.

[8] S. M. Winter, S. Hill, and R. T. Oakley, "Magnetic Ordering and Anisotropy in Heavy Atom Radicals," *J Am Chem Soc*, vol. 137, no. 11, pp. 3720–3730, 2015, doi: 10.1021/jacs.5b00672.

[9] C. M. Robertson *et al.*, "Enhanced conductivity and magnetic ordering in isostructural heavy atom radicals," *J Am Chem Soc*, vol. 130, no. 26, pp. 8414–8425, 2008, doi: 10.1021/ja801070d.

[10] L. Beer *et al.*, "Dithiazolodithiazolyl Radicals: Substituent Effects on Solid State Structures and Properties," *Chemistry of Materials*, vol. 16, no. 8, pp. 1564–1572, 2004, doi: 10.1021/cm035191u.

[11] K. Lekin, J. W. L. Wong, S. M. Winter, A. Mailman, P. A. Dube, and R. T. Oakley, "Bisdithiazolyl Radical Spin Ladders," *Inorganic Chemistry*, vol. 52, no. 4, pp. 2188–2198, Feb. 2013, doi: 10.1021/ic302658c.

Document signat digitalment per: CRISTINA RONCERO BARRERO

[12] J. L. Brusso *et al.*, “Isostructural bisdithiazolyl and bisthiaselenazolyl radicals: Trends in bandwidth and conductivity,” *Inorganic Chemistry*, vol. 45, no. 26, pp. 10958–10966, Dec. 2006, doi: 10.1021/ic061687c.

[13] A. A. Leitch *et al.*, “From magnets to metals: The response of tetragonal bisdiselenazolyl radicals to pressure,” *J Am Chem Soc*, vol. 133, no. 15, pp. 6050–6060, 2011, doi: 10.1021/ja200391j.

[14] C. M. Robertson, S. M. Winter, J. A. K. Howard, M. R. Probert, and R. T. Oakley, “Low temperature insights into the crystal and magnetic structure of a neutral radical ferromagnet,” *Chemical Communications*, vol. 57, no. 79, pp. 10238–10241, 2021, doi: 10.1039/D1CC03842G.

[15] J. S. Tse *et al.*, “Metallization of a hypervalent radical dimer: Molecular and band perspectives,” *J Am Chem Soc*, vol. 132, no. 13, pp. 4876–4886, 2010, doi: 10.1021/ja100216c.

[16] A. A. Leitch, X. Yu, C. M. Robertson, R. A. Secco, J. S. Tse, and R. T. Oakley, “Isostructural bis-1,2,3-thiaselenazolyl dimers,” *Inorganic Chemistry*, vol. 48, no. 20, pp. 9874–9882, 2009, doi: 10.1021/ic901563n.

[17] A. A. Leitch *et al.*, “Spin-canting in heavy atom heterocyclic radicals,” *Chemical Communications*, no. 32, p. 3368, 2007, doi: 10.1039/b708756j.

[18] C. M. Robertson *et al.*, “Ferromagnetic ordering in bisthiaselenazolyl radicals: Variations on a tetragonal theme,” *J Am Chem Soc*, vol. 130, no. 44, pp. 14791–14801, 2008, doi: 10.1021/ja8054436.

[19] K. Lekin *et al.*, “Hysteretic spin crossover between a bisdithiazolyl radical and its hypervalent σ-dimer,” *J Am Chem Soc*, vol. 132, no. 45, pp. 16212–16224, 2010, doi: 10.1021/ja106768z.

[20] K. Lekin *et al.*, “Heat, pressure and light-induced interconversion of bisdithiazolyl radicals and dimers,” *J Am Chem Soc*, vol. 136, no. 22, pp. 8050–8062, 2014, doi: 10.1021/ja502753t.

[21] L. Beer *et al.*, “Bis-1,2,3-thiaselenazolyl radicals and their σ-bonded dimers,” *Chemical Communications*, no. 12, pp. 1543–1545, Mar. 2005, doi: 10.1039/b416352d.

[22] H. Phan, K. Lekin, S. M. Winter, R. T. Oakley, and M. Shatruk, “Photoinduced solid state conversion of a radical σ-dimer to a π-radical pair,” *J Am Chem Soc*, vol. 135, no. 42, pp. 15674–15677, Oct. 2013, doi: 10.1021/ja4055806.

[23] A. A. Leitch, C. E. McKenzie, R. T. Oakley, R. W. Reed, J. F. Richardson, and L. D. Sawyer, “Bimodal association of a bis-1,2,3-dithiazolyl radical,” *Chemical Communications*, no. 10, pp. 1088–1090, 2006, doi: 10.1039/b517098b.

[24] A. A. Leitch *et al.*, “An alternating π-stacked bisdithiazolyl radical conductor,” *J Am Chem Soc*, vol. 129, no. 25, pp. 7903–7914, 2007, doi: 10.1021/ja071218p.

[25] A. Mailman, C. M. Robertson, S. M. Winter, P. A. Dube, and R. T. Oakley, “The Importance of Electronic Dimensionality in Multiorbital Radical Conductors,” *Inorganic Chemistry*, vol. 58, no. 9, pp. 6495–6506, 2019, doi: 10.1021/acs.inorgchem.9b00691.

Document signat digitalment per: CRISTINA RONCERO BARRERO

[26] A. Mailman *et al.*, “Crossing the insulator-to-metal barrier with a thiazyl radical conductor,” *J Am Chem Soc*, vol. 134, no. 24, pp. 9886–9889, 2012, doi: 10.1021/ja303169y.

[27] X. Yu *et al.*, “Semiquinone-bridged bisdithiazolyl radicals as neutral radical conductors,” *J Am Chem Soc*, vol. 134, no. 4, pp. 2264–2275, 2012, doi: 10.1021/ja209841z.

[28] J. W. L. Wong *et al.*, “Supramolecular architecture, crystal structure and transport properties of the prototypal oxobenzene- bridged bisdithiazolyl radical conductor,” *Chem. Commun. Chem. Commun*, vol. 50, no. 50, pp. 785–787, 2014, doi: 10.1039/c3cc46686h.

[29] J. W. L. Wong *et al.*, “Pressure induced phase transitions and metallization of a neutral radical conductor,” *J Am Chem Soc*, vol. 136, no. 3, pp. 1070–1081, 2014, doi: 10.1021/ja411057x.

[30] A. Mailman *et al.*, “Fine Tuning the Performance of Multiorbital Radical Conductors by Substituent Effects,” *J Am Chem Soc*, vol. 139, no. 4, pp. 1625–1635, Feb. 2017, doi: 10.1021/jacs.6b11779.

[31] X. Yu, A. Mailman, P. A. Dube, A. Assoud, and R. T. Oakley, “First semiquinone-bridged bisdithiazolyl radical conductor: A canted antiferromagnet displaying a spin-flop transition,” *Chemical Communications*, vol. 47, no. 16, pp. 4655–4657, 2011, doi: 10.1039/c1cc10598a.

[32] A. Mailman *et al.*, “Multiple orbital effects and magnetic ordering in a neutral radical,” *J Am Chem Soc*, vol. 137, no. 3, pp. 1044–1047, Jan. 2015, doi: 10.1021/ja512235h.

[33] A. Mailman *et al.*, “The Power of Packing: Metallization of an Organic Semiconductor,” *J Am Chem Soc*, vol. 139, no. 6, pp. 2180–2183, Feb. 2017, doi: 10.1021/jacs.6b12814.

[34] K. Lekin *et al.*, “Benzoquinone-Bridged Heterocyclic Zwitterions as Building Blocks for Molecular Semiconductors and Metals,” *Inorganic Chemistry*, vol. 57, no. 8, pp. 4757–4770, 2018, doi: 10.1021/acs.inorgchem.8b00485.

Document signat digitalment per: CRISTINA RONCERO BARRERO

A2. CASPT2 benchmark

		IpeaShift	Shift	Ref W. 1	Ref W. 2	MS overlp.	H_{AB} /meV
(S,S)	H_{π}^{+}	0.25	0	0.36806	0.23677	$4.2442 \cdot 10^{-4}$	42.24
		0	0	0.36950	0.37034	$-1.899 \cdot 10^{-5}$	34.31
		0	0.1	0.39673	0.39677	-0.00002814	35.14
		0	0.2	0.41884	0.41888	-0.00002555	34.97
	H_{π}^{-}	0.25	0	0.30732	0.33316	-0.02468564	673.37
		0	0	0.00000	0.09269	3.48527591	565170.37
		0	0.1	0.39516	0.39508	0.00134605	39.13
		0	0.2	0.42108	0.42115	0.00127871	37.73
	H_{2b}^{+}	0.25	0	0.35662	0.36417	-0.00219469	96.34
		0	0.1	0.17410	0.38971	0.00002333	4405.09
		0	0.2	0.41259	0.41240	-0.00004902	75.88
(S,Se)	H_{π}^{+}	0.25	0	0.35925	0.36207	0.00034627	52.40
		0	0	0.33353	0.32727	-0.00216796	87.79
		0	0.1	0.38720	0.38668	-0.00007208	42.48
		0	0.2	0.41006	0.40981	-0.00009461	46.17
	H_{π}^{-}	0.25	0	0.30946	0.26517	0.00021784	124.60
		0	0.1	0.37998	0.37543	-0.00163776	129.37
		0	0.2	0.41053	0.41045	-0.00102617	152.57
	H_{2b}^{+}	0.25	0	0.31905	0.34302	0.00016032	121.89
		0	0.1	0.38368	0.35916	0.00053353	109.86
		0	0.2	0.41225	0.41163	-0.00006869	128.44
	H_{2b}^{-}	0	0.1	0.38883	0.38660	-0.00026212	129.37
		0	0.2	0.41360	0.41357	-0.00019322	152.57

Document signat digitalment per: CRISTINA RONCERO BARRERO

A3. Band structure plots

Band structure calculation of FM, AFM1, AFM2, AFM and CS states have been performed on (Se,Se) using a recently characterised X-Ray crystal structure at 2 K (see Figure A3.1). Notice that FM and AFM band diagrams reported here have been obtained in a 1x1x2 supercell of the crystallographic cell.

(a) FM – 2 cells

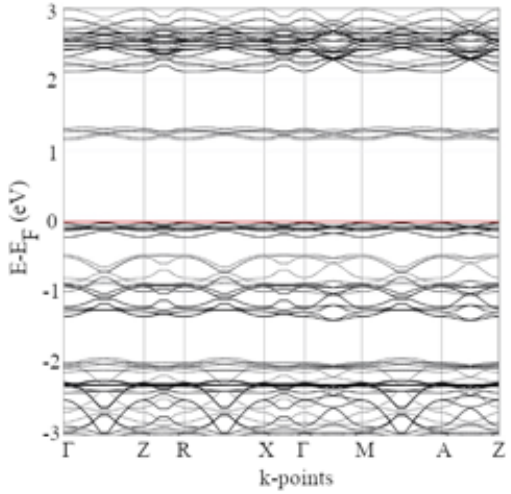

(b) AFM1

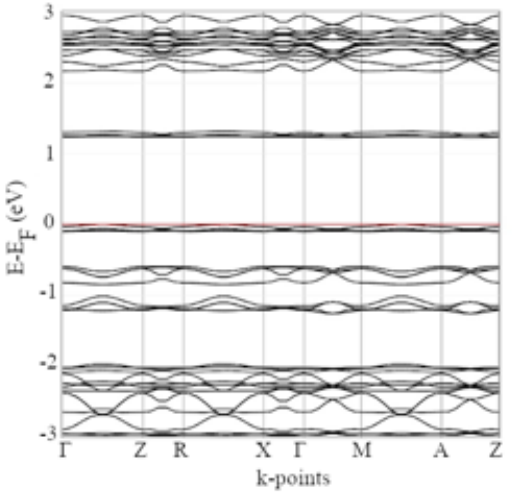

(c) AFM2

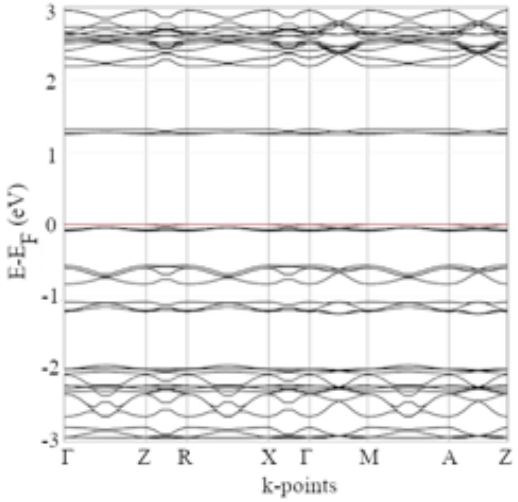

(d) AFM – 2 cells

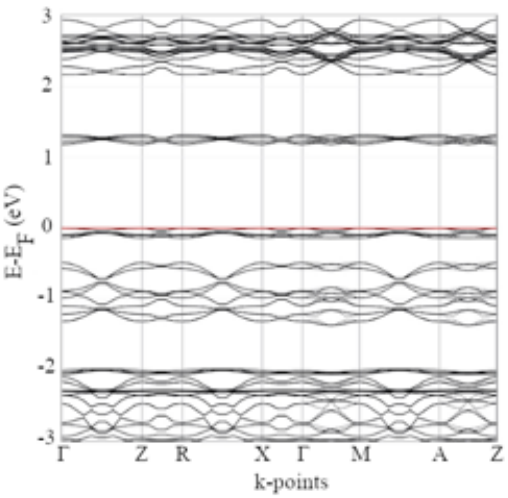

Document signat digitalment per: CRISTINA RONCERO BARRERO

(e) CS

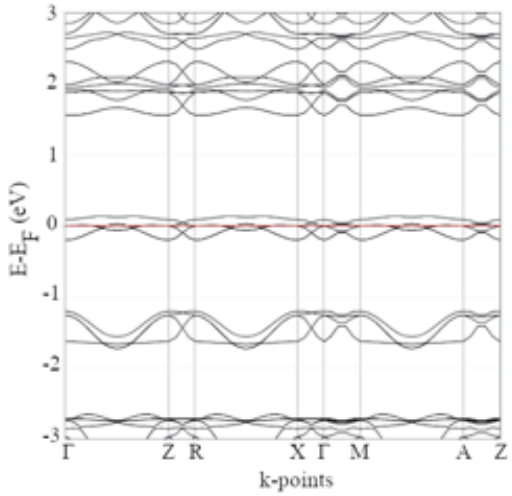

Figure A3.1. Band structure plots of (Se,Se) compound using X-Ray crystal structure determined at 2K.

(a) (S,S): AFM2

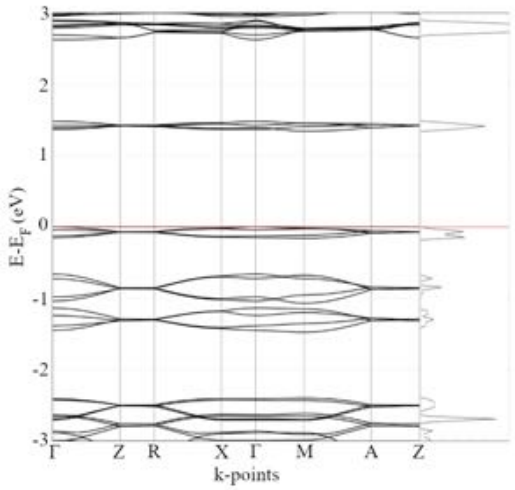

(b) (S,Se): AFM2

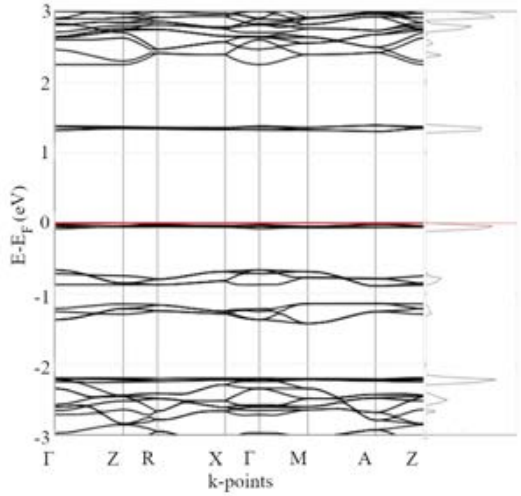

(c) (Se,S): AFM2

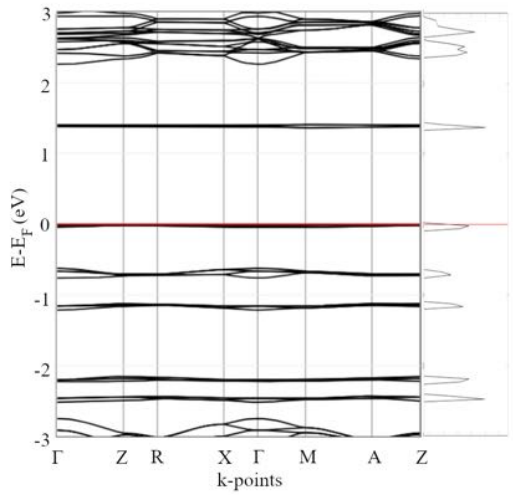

(d) (Se,Se): AFM2

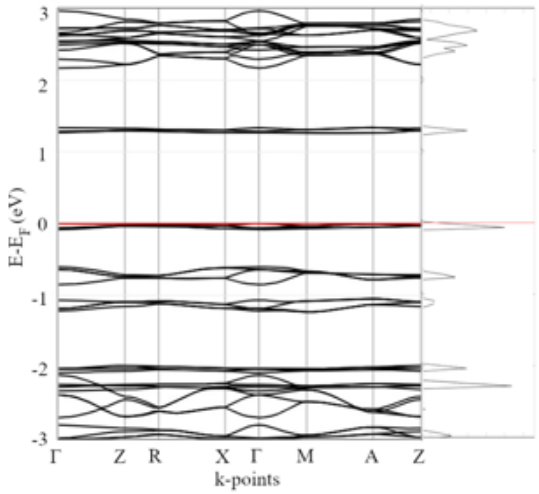

Figure A3.2. Band structure plots and normalized density of states plots of the AFM2 solution for the studied compounds. The top of the valence bands has been set at 0 eV.

Document signat digitalment per: CRISTINA RONCERO BARRERO

Document signat digitalment per: CRISTINA RONCERO BARRERO